SEASONAL AND SPATIAL STRUCTURE OF THE GRAVITY WAVES AND VERTICAL WINDS OVER THE CENTRAL USA DERIVED FROM THE NOAA PROFILER NETWORK DATA.

A Dissertation Presented to
The Academic Faculty

by

Oleksandr Karabanov

In Partial Fulfillment
of the Requirements for the Degree
Doctor of Philosophy in Atmospheric sciences
in the School of Earth and Atmospheric Sciences

Georgia Institute of Technology
August 2006

SEASONAL AND SPATIAL STRUCTURE OF THE GRAVITY WAVES AND VERTICAL WINDS OVER THE CENTRAL USA DERIVED FROM THE NOAA PROFILER NETWORK DATA.

Approved by:

Dr. R. G. Roper, Advisor
School of Earth and Atmospheric Sciences
Georgia Institute of Technology

Dr. Irina Sokolik
School of Earth and Atmospheric Sciences
Georgia Institute of Technology

Dr. Derek Cunnold
School of Earth and Atmospheric Sciences
Georgia Institute of Technology

Dr. Paul Steffes
Electrical & Computer Engineering
Georgia Institute of Technology

Dr. Robert Black
School of Earth and Atmospheric Sciences
Georgia Institute of Technology

Date Approved: 06/06/2006

ACKNOWLEDGEMENTS

I would like to express my gratitude to Dr. R.G. Roper for his support and valuable help during my graduate studies. I would like to thank Georgia Institute of Technology and the School of Earth and Atmospheric Sciences for financial and organizational support. Also I wish to express my appreciation to the members of my dissertation committee: Dr. D. Cunnold, Dr. R. Black, Dr. I. Sokolik and Dr. P. Steffes for their time and expertise.

I wish to thank Dr. N. Meskhidze and Dr. Dong L. Wu (JPL/Caltech, Pasadena, CA) for their helpful discussions. Also, I am grateful to Dr. J. St. John, Dr. Yuhang Wang and Dr. Tao Zeng for their help with obtaining some data.

I must express my gratitude to my parents and all my friends for their support and understanding, which made my graduate studies and this work possible.

TABLE OF CONTENTS

LIST OF TABLES

LIST OF FIGURES

Page

LIST OF SYMBOLS AND ABBREVIATIONS

NOAA	National Atmospheric and Oceanic Administration
NPN	NOAA Profiler Network
VHF	Very High Frequency (30 - 300 MHz)
UHF	Ultra High Frequency (300 - 3000 MHz)
GCM	General Circulation Model
NCAR	National Center for Atmospheric Research
NCEP	National Center for Environmental Prediction
DAWEX	Darwin Area Wave Experiment
NetCDF	Network Common Data Form
USGS	U.S. Geological Survey
u	zonal component of the wind velocity
v	meridional component of the wind velocity
w	vertical component of the wind velocity
ρ	Air density
$\hat{w}$	Amplitude of the vertical component of gravity wave
FTP	File Transfer Protocol
RAOB	Radiosonde Observation
UTC	Coordinated Universal Time
PV	Potential Vorticity

SUMMARY

The high-resolution, long-term measurements by the National Oceanic and Atmospheric Administration wind profiling radar network, covering the central part of the USA, are here used (1) to investigate the effects of precipitation, topography and gravity wave on the measurements of winds by UHF wind profilers, and (2) to study the climatology and sources of gravity waves.

Profiler vertical winds were compared to the NCAR/NCEP reanalysis (on long timescale) and MM5 model (on short timescale). The comparison revealed that the averaged wind profiler vertical velocities are strongly affected by precipitation both directly and via enhanced gravity wave activity produced by convection. Precipitation effects were found to be most important in the lowest 3 km of the troposphere.

Based on the statistics of the vertical wind velocities we have determined a vertical velocity threshold of -0.25 m/s to be the most suitable for identifying and correcting of the precipitation-affected data. Corrected (by the use of the above threshold) records of the profiler-measured vertical winds show much better agreement with both reanalysis and model data.

For the first time the profiler network has been used to obtain a detailed climatology of the gravity waves over the central USA. The characteristics of the gravity waves in three period bands (6 min - 1 hour, 1 - 3 hours and 3 - 12 hours) and for three orthogonal spatial components were obtained using spectral analysis of the profiler-measured winds, and verified using the wind variance. The most energy was found in the low frequency horizontal components of the gravity waves. A consistent annual,

geographical and seasonal pattern of total gravity wave energy was observed in the troposphere, with maxima reaching ~25 J/kg in winter at ~ 8 - 10 km altitude.

In order to evaluate the effects of topography on gravity wave generation, we have developed a simple technique for quantifying the topography variance near the measurement sites. Using these estimates we have determined that topography is an important source of the medium- and high-frequency waves in the middle troposphere.

Correlation and regression analyses were used to study the other sources of the gravity waves and their variation with altitude. Precipitation (as a proxy for convection) was found to explain a significant part of the vertical component of the gravity wave energy and total wave energy in the lower troposphere, while vertical shear of the zonal wind was the most important source in the upper troposphere and, more generally, for the total gravity wave energy at all altitudes.

This study provides important information for (a) interpreting the wind measurements taken with wind profiling radars, (b) better understanding of the structure and sources of the gravity waves, and (c) improving gravity wave parameterizations in global circulation models.

CHAPTER 1

INTRODUCTION

1.1 Vertical air motions in the atmosphere and their study with wind profilers

Vertical motions of the atmosphere are critically important in atmospheric science because they are both a product of and a cause for many atmospheric phenomena. Thus, for example, upward motions modify atmospheric stability and promote the formation of clouds and precipitation. At the same time, vertical motion can result from horizontal advection of air masses with different temperatures. There are several areas of atmospheric science where vertical air motions are of significant importance.

Knowledge of the vertical velocities is a crucial point in modeling the microphysics of cloud formation, their dynamics and resulting precipitation type.

Integration of high-resolution vertical motions makes it possible to calculate vertical transport of the trace chemical constituents (Ruster at al., 1998), such as ozone, NO_x , water vapor, etc. Incorporated into chemical box models, knowledge of vertical motions allows for realistic adjustment of ambient physical properties along the path of the pair parcel.

Simultaneous high-resolution measurements of both horizontal (*u, v*) and vertical (*w*) winds together with known density ρ allows calculation of another important dynamical quantity – the vertical flux of horizontal momentum, $\tau_R = \rho(\overline{u'w'}^2 + \overline{v'w'}^2)^{1/2}$, (Chang et al., 1997).

Despite the importance of knowing the vertical air motions, and unlike the horizontal motions, that have been extensively measured, direct measurements of vertical wind have been very scarce and limited in resolution and coverage. Much of our present knowledge of the role of vertical velocity in weather and climate comes from indirect methods (kinematic, adiabatic or omega equation methods can be used to derive vertical motions) and is the result of the analysis of large-scale synoptic wind fields that are measured directly (Holton, 2004; McAfee at al., 1995). Typically, vertical motions on a large scale are several orders of magnitude smaller than the velocities of horizontal motions, and, therefore derivations of the former from the latter are sensitive to the errors in the horizontal wind fields. These fields are usually smoothed and interpolated, and do not carry information about processes at small scales.

Until recently, *in-situ* measurements using meteorological towers and accelerometers onboard airplanes were the only available techniques for direct measurements of vertical air motions. Later, the radar tracking of ascending jimspheres was used to calculate vertical velocities, providing some estimates of the ascend rate in the absence of atmospheric motions. With development of technology and appearance of remote sensing tools, new possibilities opened for direct vertical wind measurements. One of these remote sensing tools – wind profilers – made it possible to measure both horizontal and vertical velocities with exceptional spatial and temporal resolution, and at low cost.

The wind profiling technique was developed on the basis of experimental VHF (30-300 MHz, most frequently using frequencies ~ 50 MHz) Doppler radars (Gage and Balsley, 1978; Kato et al., 1984) that were operated mostly on a short-campaign basis by

research institutions. First measurements of vertical winds by wind profilers (Peterson and Balsley, 1979; Nastrom and Gage, 1984; Ecklund et al., (1982); Gage (1983); Green et al., (1988), etc.) raised questions as to the accuracy of such a measurements (e.g. May at al., 1988; Nastrom at al., 1990, Rottger and Larsen, 1990). The problem of determining how reliable are the vertical wind measurements by wind profilers is complicated by several factors:

1) the absence of "ground truth" data that can be used for establishing profiler measurement errors, and
2) the extreme variability of both the time scales and magnitudes of vertical air motions due to the large number of physical processes involved.

On the "background" of synoptic- and meso-scale vertical motions with magnitudes of ~1 cm/s and characteristic times of days, there co-exist multiple smaller scale motions, from sub-synoptic scale to local processes such as convection, gravity waves, large-scale turbulence, with magnitudes up to meters per second (McAfee et al., 1995; Nastrom et al., 1994). The question of how well the profilers measurements of vertical wind represent real atmospheric motions received significant attention as the number of operational wind profilers increased and longer datasets became available. The vertical wind measurements, beside the reasons listed above, are of special importance for the wind profiling technique because in the typical radar beam configuration (two off-zenith beams with zenith angle θ and one vertical beam), in order to obtain the zonal *u* and meridional *v* wind, measured radial wind components u_r and v_r need a correction proportional to the vertical wind w: $u = u_r \csc\theta - w\cot\theta$ and $v = v_r \csc\theta - w\cot\theta$ (Clifford et al., 1994).

Later in 1990's, when wind profiling technology became well established, the routine measurements from the NPN (NOAA Profiler Network) at UHF were used for weather forecasting and data assimilation for models, typically as a source of high-resolution horizontal wind measurements (Nash, 1994; Monna, 1994) and in some prognostic applications (e.g. Mace and Ackerman, 1996). At the same time existing VHF profilers were used mostly for research-related measurements. These studies resulted in a significant number of publications. Thus, profiler-derived winds were compared to those obtained using the kinematic method based on radiosoundings (Nastrom et al., 1994a; Nastrom and Warnock, 1994) and based on profiler-measured horizontal wind (Rao et al., 2003) and scanning Doppler Weather radar (Cifelli at al., 1996) . Also, comparisons were made with model output (Larsen et al, 1988) and with NCAR/NCEP reanalysis by Schafer et al., (2003). Long-term measurements were analyzed by Huaman and Balsley (1996) and Gage et al., (1991); and extremely high vertical resolution (75m) data with a vertically pointing beam were presented by Ruster et al., (1998) for various meteorological conditions.

The findings of the studies on the interpretation of vertical wind measurements by profilers can be summarized as follows. In general, on a time scales of days, measurements of vertical winds by wind profilers show satisfactory agreement with dynamical conditions and winds derived with the other methods, especially on clear days. For tropical sites, long-term averages of w are positive in the lower troposphere and negative in the upper troposphere and do not exceed 1-2 cm/s. Most of the profilers located in midlatitudes have a negative (downward) vertical velocity on the order of several centimeters up to tens of centimeters per second in the troposphere, on the longer

timescales. In the upper troposphere the sign of these relatively large velocities changes from negative to positive, with magnitude of several cm/s. These values were substantially larger than expected for typical large-scale vertical motions. Several mechanisms were proposed to explain this negative/positive bias, including:

1. Possible contamination of the small magnitude vertical winds by significantly larger horizontal winds if a small error in beam-pointing is present (Huaman and Balsley, 1996);
2. Aspect sensitivity - reflection from tilted layers, resulting in *effective* beam tilting from vertical, and consequent contamination of vertical winds by the horizontal component (e.g. Doviak and Zrnić (1984b); Tsuda et al., 1986);
3. Mechanism of gravity waves modification of reflectivity, leading to enhanced scattering from the downward moving air parcels and therefore biases in the wind (Nastrom and VanZandt, 1996);
4. Topography-induced mountain wave component of the wind, when the phase of the wave above the radar is not random (Worthington 1999; Worthington et al., 2001)
5. Possible effect of Kelvin-Helmholtz instabilities in regions of strong vertical shear of the winds near the jet-stream (Muschinski, 1996)
6. Gradients in the flow within the sampling volume, namely divergence, leading to bias in vertical wind measurements (Larsen and Palmer, 1997);
7. Possible presence of hydrometeors in the sampling volume can lead to changes in reflectivity (e.g. Vaughan and Worthington, 2000) and to the fact that the measured vertical velocity will be reflectivity weighted, i.e. biased toward the

terminal velocity of the raindrops (Ralph 1995a; Ralph 1995b; Chu et al., 1997; Orr and Martner 1996).

Despite the progress in understanding the physics of phenomena affecting the vertical wind measurements, the relative importance of these mechanisms is still unknown, and possible magnitudes of introduced biases are determined only coarsely.

It should be noted that most of the mentioned studies and measurements of vertical velocity were based on VHF profilers, so the extent of the vertical wind biases for a UHF profilers is even less well known, as the physics of the scattering is wavelength-dependent. For example, the aspect sensitivity is considered to have less effect on a UHF profiler than on a VHF one (Muschinski and Wode, 1998).

To summarize, the most extensively operated UHF wind profilers (the NOAA network), and therefore potentially the most valuable in terms of long-time high-resolution measurements, are the least studied in terms of the interpretation of vertical wind measurements. There is only one study known to the author, which addresses vertical wind-measuring performance of UHF wind profilers (initial results reported by McAfee et al., 1994; McAfee et al., 1995). The drawback of previous VHF studies is that long-term records of vertical wind were not considered in their connection to corresponding records of such important background meteorological conditions as precipitation, horizontal wind and wind shear, etc. Also, newer, advanced models are now available for case studies and validations. The wide geographic spread of the NPN profiler sites is another beneficial factor that has not been exploited. The network can be very useful in determining the importance of orographic and local climatic effects.

1.2 Wind profilers and atmospheric gravity waves

One of the phenomena inherently connected to vertical air motions is gravity waves. Atmospheric gravity waves (this term is usually confusing for non-atmospheric scientists, and the better physical description would probably be "buoyancy waves"; nonetheless, we will follow the former notation) play an important role in the dynamics of the middle and upper atmosphere. Being generated mostly in the troposphere, gravity waves, together with large-scale eddies transport energy and momentum to the upper atmosphere, where, due to the wave breaking, energy is deposited and the mean flow is therefore modified (Holton, 1990; Salby 1996).

Despite the fact that ~75% of the atmospheric mass is confined to the lowest 10 km (troposphere), recent discoveries show that the stratosphere can force changes in the troposphere, and therefore stratospheric dynamics is vital for long-term weather forecasting and climate modeling with general circulation models (GCM) (e.g. Egger and Hoinka, 2005; Black et al., 2005; Mukougawa and Hirooka, 2004).

Another aspect of gravity wave importance is that the vertical transport of the chemical species, such as ozone and ozone-related chemicals, depends on the residual mean meridional circulation driven by the drag force exerted by Rossby and gravity waves (McLandress 1998; Holton, 1990; Butchart and Scaife, 2001). Also, gravity wave-induced updrafts can force cloud formation and therefore affect radiative balance both at small and planetary scales. Mesoscale gravity waves are recognized as a phenomenon responsible for organizing cloud fields and precipitation bands (Trexler and Kosh, 2000).

In spite of the constantly increasing capabilities of computers and the growing resolution of GCMs the gravity waves represent sub-grid scale phenomena. Even at 1° resolution, the modeled stratospheric flow is still considerably different from observations due to unaccounted gravity wave effects (Hamilton, 1996). Therefore, the effects of gravity waves on the mean flow should be represented in some simple, but realistic way, i.e. parameterized in models (McLandress, 1998). Despite some success of the existing parameterization schemes, they still have significant drawbacks. The sources of tropospheric gravity waves are not completely understood, and thus knowledge of the spatial and temporal distribution of sources is incomplete. Currently, only topographic waves are parameterized both in time and space with moderate success (Alexander et al., 2002). A directly observed climatology of the tropospheric gravity waves would provide new fundamental knowledge of how the waves are generated and dissipated and how they interact with the mean flow and other atmospheric phenomena.

Several observational techniques have been used to study gravity waves. The earlier studies of upper- and middle-atmospheric gravity waves were based on rocket measurements (e.g. Hirota, 1984; Philbrick and Chen, 1992). The lidar technique was also used for observations of stratospheric and mesospheric waves (Gardner et al., 1989; Beatty et al., 1992; Hertzog et al., 2001). Recently, satellite observations and GPS meteorology have become widely used to study gravity waves in the middle atmosphere, for example studies by Tsuda et al., (2000) and Jiang et al., (2005) established the morphology of gravity waves in the middle atmosphere. Rocket and lidar measurements provide good altitude resolution but very limited spatial coverage, while satellite measurements potentially can provide global coverage.

Routine radiosonde probing has the advantage of very good spatial coverage, the largest time-span of all techniques and high reliability and precision. It has been traditionally used as a data source for gravity wave research. Kitamura and Hirota (1989) observed gravity waves over Japan and have determined their altitudinal structure. Similarly, Allen and Vincent (1995) have obtained the climatology of gravity waves in the troposphere-stratosphere above Australia and Antarctica, based on high-resolution radiosounding data. Recently, Wang and Geller (2003), followed the methodology of Allen and Vincent (1995) to obtain the morphology of gravity-wave energy from US radiosonde data. They determined the latitudinal structure of the wave energy in the troposphere and lower stratosphere over North America, and analyzed seasonal variations. Other findings included the discovery of apparently low correlations between tropospheric and stratospheric wave energy and the recognition of the Rocky Mountains as a significant wave source for the troposphere. At the same time their work has several drawbacks:

- radiosoundings used were performed at the same fixed times (00 UTC and 12 UTC) for all sites, therefore the sampling of the gravity wave activity might be biased if there is a significant diurnal variation (for example, convection is one of the sources for gravity waves, and it has a defined diurnal cycle);
- the variations in vertical profiles of horizontal wind and temperature, used as a proxy for gravity wave oscillations might as well be stationary layers. Sparse temporal sampling of radiosondes does not allow for resolving this issue;
- as a result, no gravity wave frequency-related information is obtained and waves are not resolved in the frequency domain;

- vertical velocity contribution is not accounted for;
- the sources were not clearly identified. The troposphere was considered as a whole, not allowing for the resolution of different areas with attributed different sources of generation.

Many of the mentioned drawbacks are inherent to radiosounding as an in-situ measurement tool and, therefore, wind profilers can be very beneficial if used in gravity wave research. Wind profiler studies of gravity waves on a case study basis have been conducted since the development of the profiler technique. Significant interest in profiler use for gravity wave research still exists now, which is obvious from a large number of recent publications in the area. Among other techniques, the Boundary Layer profiler was used by Hamilton et al., (2004) in a DAWEX field campaign. An important advance was made by Hansen et al., 2001 who derived a 5-year climatology of gravity waves with the VHF radar at White Sands, NM, in the troposphere and lower stratosphere. Later studies also include the use of spatially distributed profilers. The lifecycle of mesoscale gravity waves was studied by Trexler and Kosh, (2000); Serafimovich et al., (2005) derived important parameters of gravity waves during a Rossby wave breaking event using a complex cross-spectral analysis of data from 2 profilers.

Given the interest in the topic, proven technique and availability of NPN data, the next logical step would be to use a network of wind profilers to obtain a climatology of gravity waves over central USA. This would complement existing data obtained with the above mentioned radiosounding and satellite studies, and can lead to a better understanding of the morphology of the gravity waves and ultimately result in their better parameterization in numerical models and therefore, to improved atmospheric models.

1.3 Topography and its effect on gravity waves and vertical winds

An important factor that affects both vertical winds and gravity waves is topography. Variations in the terrain surrounding a location of interest could significantly affect local winds, precipitation patterns and generate atmospheric waves and turbulence.

On a small scale (meters to hundreds of meters) the properties of the land surface can be described in terms of the aerodynamic roughness length z_0, which can be either calculated from direct wind profile measurements or derived from local topography variations. The estimation of aerodynamic roughness length has been addressed in many papers (e.g., Tieleman, 2003; DeVries et. al., 2003). In general, roughness length characterizes the wind profile in the lower part of a neutrally stratified boundary layer over homogeneous terrain (DeVries et al., 2003). On larger spatial scales (order of kilometers and more) the terrain and land surface properties vary significantly and can not be considered homogeneous. This heterogeneity leads to the introduction of integral quantities, like *effective* aerodynamic roughness length, and involves a variety of semi-empirical techniques for its determination.

At the same time, in many geophysical and atmospheric research applications, especially involving measurements of the atmospheric variables at significant height above the ground and those that have a large upwind fetch, a larger scale description of the surrounding terrain is needed.

One of the areas where quantitative classification of terrain in terms of topography variation on the scale of a tenth to hundreds of kilometers would be

especially useful, is analyzing vertical velocity and gravity waves seen by wind profiling radars. As pointed out above, measurements of both horizontal and vertical components of the wind by the wind profiling radars could be affected by the presence of gravity waves. At the same time, in publications discussing effects of terrain and topography on the radar measurements of winds in the troposphere, authors are usually limited to a verbal description of the terrain, such as: "…radar is surrounded by hills and low mountains in all directions…" by Hansen and Nastrom, (2001) about the location of the MU radar in Japan; or "…very flat terrain, far from any mountains…" - about the Flatland VHF radar near Champaign-Urbana, Illinois - Nastrom et al, (1990). Comparison of the results from multiple wind profiling radar sites would significantly benefit if quantitative estimates of terrain variation around these sites were readily available.

A technique for classification of the terrain in terms of topography effects on the surface winds was suggested by Z. Sen (1999). Based on the comparison of the graphs of semi-variance cumulative functions of the wind and elevation measured at multiple sites, Z. Sen classifies five different classes of terrain. While being helpful in identifying different types of terrain, this "semivariogram cumulative technique" does not give quantitative characteristics helpful for direct comparison of the sites. Also, in this technique, the relative positions of the sites with respect to the prevailing wind direction are not taken into account (only absolute values of distances are incorporated into cumulative semivariogram).

Therefore, there exists the need for a method that would allow for a simple quantitative estimate of the variability in topography surrounding a site of interest.

1.4 Goals and objectives of the study and organization of the material

This study is an attempt to utilize the unique capabilities of wind profiling radars in order to look at both the vertical winds and gravity waves in a new way – by using high-resolution, multi-seasonal, spatially-distributed observations from the NPN, and relating them to the topographic features around the measurement sites and to the basic atmospheric characteristics – horizontal wind, wind shear and precipitation. The goals and objectives of this study are:

- to examine the structure of the monthly mean vertical winds at multiple locations as seen by the NPN over several seasons, and to compare the profiler-derived vertical winds to the NCAR/NCEP reanalysis data (on a long-time scale);
- compare the profiler-derived vertical winds to the contemporary regional MM5 model (on a short time-scale);
- to improve the understanding and interpretation of vertical wind measurements by UHF wind profilers through comparison of records of vertical winds with corresponding records of background meteorological variables;
- to better assess the gravity wave energy characteristics over central USA both in altitude and frequency domain, and the sources of their generation;
- to develop a technique for quantitative depiction of the topography surrounding measurement sites;

- using this depiction, to estimate the effects of topography on gravity wave energy and on vertical winds in order to facilitate the analysis of the sources of the wave generation and biases in vertical wind measurements by wind profilers.

The work is organized as follows. First, in chapter 2, we describe the specific features of wind profiling radar technique and details of the data processing algorithms that were utilized in this study. We also describe the precipitation rate data used for this study. Then, in chapter 3 we present the data and analyze the long-term averages of horizontal and vertical wind motions as seen by the NPN, some statistical properties and altitude dependences, and the relation to horizontal wind, wind shear and precipitation.

In chapter 4 the long-term records of profiler vertical winds are compared to NCEP/NCAR reanalysis vertical winds. Further, moving from long to short timescales, a case-study comparison between the NPN measurements of vertical winds and MM5 model data is described. Based on the results of these comparisons and distributions of the profiler vertical velocities, we develop a precipitation correction scheme, apply it to profiler data and discuss the improvements both on long and short timescales.

Then, in chapter 5 we describe two techniques used for gravity wave analysis, based on 1) wind variance and 2) spectral analysis of the wind time series, and present the obtained gravity wave climatology. We also analyze the possible sources of the waves and their relative importance for generating waves of different frequencies at different altitudes.

Chapter 6 is focused on the suggested method for quantitative estimation of topography variations around measurement sites. Using these estimates, we evaluate the contribution of topography as a gravity wave generation source.

In chapter 7 we present a linear multiple regression model designed to investigate the effects of the precipitation, zonal wind and gravity waves on vertical velocities measured by wind profilers, and discuss the results of the regression analysis. In the second half of the chapter, similar approach is used to model the gravity wave energy based on precipitation, zonal wind and wind shear.

In the concluding chapter, we summarize and discuss the findings of the study and give suggestions about future research that could complement our results.

CHAPTER 2

WIND PROFILING TECHNIQUE AND DATA PROCESSING

2.1 History of the wind profiling technique

Based on the available publications, we can attribute the first observations of radio waves scattered by "invisible" atmospheric targets to the 1930-ies. In 1936, Colwell and Friend (1936) were observing medium- and short-wave reflections from heights of about 10 km. Further studies were conducted after World War II, and later were accommodated into the fundamentals of the wind profiling technique. After the war high-sensitivity centimeter-band radars, created by the military, were used for scientific purposes. They were the ones to rediscover the scattering of the radiowaves by clear air. The phenomena were called "angels" and were extensively studied in the fifties and sixties (e.g. Hardy, 1967). These studies demonstrated that turbulent and layered inhomogeneities of the dielectric constant of the air under clear-sky conditions can produce significant and persistent scattering in the troposphere and stratosphere. The energy and polarization properties of these scattered signals were determined, but the idea of using these signals for the purpose of wind measurements did not appear until the multi-channel Doppler-frequency resolving radars became available.

Many new types of radars for atmospheric research were developed in the 1960's. The pioneering work of Manning at al., (1953) measured the winds at mesospheric heights (80-105 km) using reflection from drifting meteor trails. Similar studies were conducted by B.L. Kashcheyev (Ukraine) since 1958. Powerful radars were implemented

to probe the upper atmosphere using incoherent ionospheric scattering (~50 km and above) (Gordon, 1958). Such radars were widely used in the sixties and seventies to study the dynamics of the ionospheric plasma. Being relatively high-powered (peak power of ~1 MW) these radars were able to study the D- and E- layers of the ionosphere using frequencies about 2 - 6 MHz. The wind measurements in the ionosphere were made possible by implementing spatially separated receiving and transmitting antennas to measure the drift of the plasma inhomogeneities. The evolutionary development of incoherent scatter radars in the seventies led to the creation of powerful scientific radars at Arecibo (Puerto-Rico), Jicamarca (Peru) and Millstone Hill (USA).

In 1970, at the Jicamarca radar unusual reflections from clear air were observed in the mesospheric region. These signals had a Doppler shift that corresponded to a horizontal velocity of tens of meters per second. Soon it was shown (Woodman and Gullen, 1974) that these reflections appear due to scattering of the radiowaves by the clear air refractive index inhomogeneities in the mesosphere and stratosphere. These findings became the theoretical base of the new generation of atmospheric research radars, capable of measuring the winds in troposphere, stratosphere and mesosphere, now known as wind profilers.

VHF band (at a frequency of about 50 MHz) wind profilers, often referred to as mesosphere-stratosphere-troposphere (MST) wind profilers, were developed at the end of the seventies - beginning of the eighties; with the pioneering work done at Poker Flat, Alaska (see Balsley and Gage, 1980), and White Sand Missile Range. In 1980, NOAA's Wave Propagation Laboratory in Boulder (now the Environmental Technology Laboratory), started a new program to create specialized UHF band wind profiling radars

(~400 MHz) for routine measurements in the troposphere and low stratosphere. Around 1984 the first radars of WPDN - Wind Profiler Demonstration Network (Chadwick, 1986) were created and underwent extensive testing and later - operational use.

2.2 Brief description of wind profiling radars and principles of operation

A wind profiler is a pulse Doppler radar operating in the VHF or UHF bands (50 MHz, 400 MHz, and 900 MHz frequencies are most often used). It is capable of measuring 3 orthogonal components of the wind vector under most weather conditions. A detailed description of wind profiling radars can be found in e.g. VanZandt, (2000) or Doviak and Zrnic, (1984a). To obtain information about overhead winds, three spatial antenna beams are usually used: one vertical and two shifted a few degrees off zenith (angle $\beta \approx 10\text{-}13°$, see figure 2.1) to the north and west.

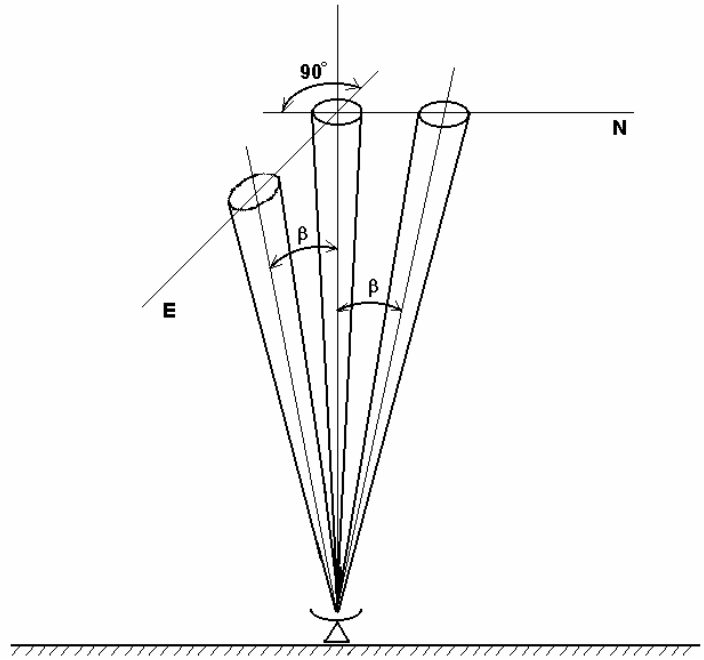

Fig. 2.1. Typical configuration of wind profiler antenna beams.

A wind profiling radar is sensitive to the turbulent irregularities of the dielectric constant (refractive index fluctuations) of the air. When turbulence has a spatial scale close to half the wavelength of the radar signal, Bragg scattering takes place, improving the reflectance. These irregularities are embedded in the flow and moving with it, and therefore the scattered signal is Doppler shifted by a value proportional to the projection of mean wind velocity V_r on the radar beam axis:

$$F_d = \frac{2 \times V_r}{\lambda}, \tag{2.1}$$

where λ - is the radar wavelength, $V_r = V \times \sin(\beta)$, V - horizontal wind speed and β – radar beam zenith angle. The Doppler shift of the signal contains information about the line-of-sight value of wind velocity and the width of the Doppler spectra provides data about wind variance in the sampled volume. The assumption of turbulence eddies being "frozen" in the mean flow is a version of widely known "Taylor hypothesis" and is a key assumption that allows wind measurements by wind profilers.

Typically, the wind profilers of the NOAA Profiler Network (NPN) are capable of measuring winds from ≈500 m up to 14-16 km (depending on weather) with ~ 250 m resolution in altitude and a temporal resolution of 6 minutes. For operational wind profilers the availability of data (percent of the time when data are available) is 75-95% (Martner et al., 1993). The precision of wind profiler measurements is comparable to those of radiosonde data (Clifford et al., 1994); this has been verified by numerous joint measurements with radiosondes, radars and lidars and comparisons with model data (Larsen et al, 1988). A more detailed description of the NPN profilers is given in Appendix A.

2.3 Features of the profiler radar signal and inherent limitations of the technique

Due to the very specific nature of the scattering media used by wind profilers, the received signal has the following characteristics:

- sensitivity to a wide spectrum of atmospheric motions of different nature;

- relatively low signal-to-noise ratio of the clear air scattered signal;

- presence of clutter.

The reflected power of the sounding signal, associated with clear-air turbulence, is proportional to the reflectivity η_{air} (Doviak and Zrnić, 1994a):

$$\eta_{air} = 0.38 \times {C_n}^2 \times \lambda^{-1/3}, \tag{2.2}$$

where ${C_n}^2$ - refractive index structure parameter; λ - radar wavelength.

For a frequency band, used in wind profiling, the ${C_n}^2$ can be estimated as (Nastrom and VanZandt, 1994):

$${C_n}^2 = \left(2.8{L_0}^{4/3}\right)\left(\frac{77\times10^{-6}P}{T\times\Theta}\right)^2\left(\left(1+\frac{15500\times q}{T}\right)\frac{\partial\Theta}{\partial z}-\frac{15500\times\Theta}{2T}\cdot\frac{\partial q}{\partial z}\right)^2, \tag{2.3}$$

where Θ - potential temperature, q - specific humidity; L_0 - turbulence outer scale; T – temperature. It is obvious from this equation, that reflected power is enhanced in layers with increased stability $\frac{\partial\Theta}{\partial z}$ or negative humidity gradient $\frac{\partial q}{\partial z}$.

Clutter arises either due to:

1) reception of sounding signals reflected (scattered) from unwanted targets through the antenna main and side lobes; or

2) due to reception of sounding signals scattered from clear air through the antenna side lobes.

Among unwanted targets (shown in figure 2.2) we can count the Earth's surface and other stationary objects, slowly moving objects - trees, power lines, precipitation, etc., and fast moving objects – birds and airplanes. Detection of the fast moving targets and "ground" clutter is usually performed during the first stage of signal processing (by radar hardware or software), while distortions of the data due to slow-moving targets are usually eliminated during secondary (by user) processing, based on the continuity principle and analysis of the atmospheric motions. The secondary data processing system, created for this study, will be described in more details in chapter 2.4.

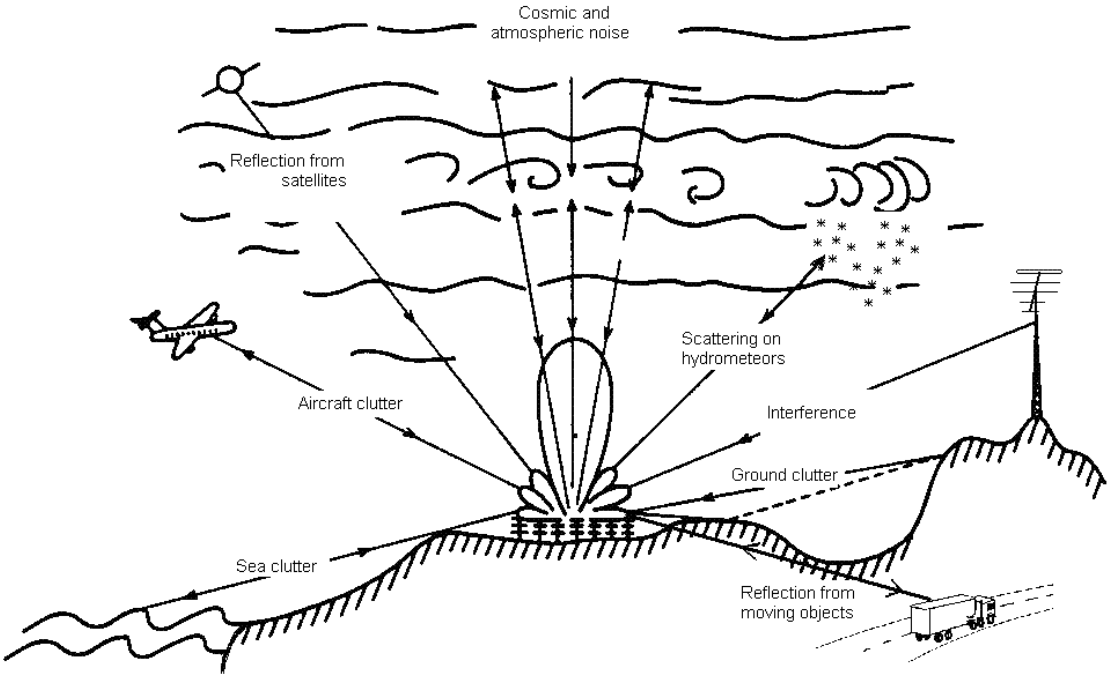

Figure 2.2. Clutter contamination of the clear air signal. Modified from Rastogi, (1983).

A significant drawback that limits the capabilities of a wind profiler is its sensitivity to hydrometeors. The Rayleigh scattering of radiowaves from small ice or rain particles may provide significantly higher reflectivity than the clear-air (Doviak and Zrnić, 1994a):

$$\eta_{rain} = \frac{\pi^5}{\lambda^4}\left|K_w\right|^2 Z\,, \tag{2.4}$$

where $Z = \frac{1}{\Delta V}\sum_i D_i^6$ is the reflectivity factor, D is the cloud particle diameter, and V is the sampling volume. Here K_w is used to denote $(m^2-1)/(m^2+2)$ where m is the complex index of refraction of water (or ice) at the wavelength λ.

In the case of rain the measured vertical velocity will be reflectivity weighted, i.e. biased toward the fall velocity of the raindrops. Horizontal winds are less susceptible to such contamination due to the much larger amplitudes of the wind. The procedures for detection of rain-contaminated data, used for this study, are discussed in section 4.3.

2.4 Profiler data used for this study and data processing algorithms

In this study we have used the high-resolution NPN data for a 3-year period starting August 2002 till July 2005. The height resolution of the data is 250 m, with lowest available data at 500 m (above ground level) and the highest available data at 16250 m. NPN data are freely available in both graphical and text (RAOB) formats with 60-minute resolution at the Forecast Systems Laboratory (FSL) website: (http://www.profiler.noaa.gov/npn/index.jsp). It is interesting, that the FSL site does not carry the full archive of the data. Also, the vertical wind component data are not available

in text-based or graphical outputs from the website. The last 14 days of 6-minute resolution measurements in NetCDF format can be downloaded via FTP.

The raw data with 6-minute temporal resolution that were used for the study were routinely downloaded from the Storm Chaser website, courtesy of Gilbert Sebenste and Dawn Gonsowski, (Northern Illinois University). The download page is available at: http://weather.admin.niu.edu/machine/ .

The data were routinely downloaded and archived for 26 NPN wind profiling radars, which were operational at the beginning of the study (August 2002). The locations and additional information on the 26 sites is given in table 2.1.

Table 2.1. Description of the NPN wind profiler sites.

Station ID #	Station abbreviation	Location	WMO ID	Latitude, deg.	Longitude, deg.	Site elevation, m
1	AZCN5	Aztec, NM	74630	36.84	-107.91	1901
2	BLMM7	Bloomfield, MO	74662	36.88	-89.97	129
3	BLRW3	Blue River, WI	74357	43.22	-90.53	225
4	CNWM7	Conway, MO	74550	37.52	-92.7	390
5	DQUA4	DeQueen, AR	74752	34.11	-94.29	195
6	FBYN1	Fairbury, NE	74440	40.08	-97.31	432
7	GDAC2	Granada, CO	74530	37.77	-102.18	1155
8	HBRK1	Hillsboro, KS	74546	38.31	-97.3	446
9	HKLO2	Haskell, OK	74648	35.68	-95.86	218
10	HVLK1	Haviland, KS	74541	37.65	-99.11	647
11	JTNT2	Jayton, TX	74735	33.02	-100.98	707
12	LMNO2	Lamont, OK	74647	36.69	-97.48	306
13	LTHM7	Lathrop, MO	74551	39.58	-94.19	297
14	MBWW4	Medicine Bow,	74431	41.90	-106.19	1996
15	NDSK1	Neodesha, KS	74542	37.30	-95.601	265
16	NLGN1	Neligh, NE	74445	42.21	-97.79	524
17	OKOM6	Okolona, MS	74769	34.09	-88.86	125
18	PATT2	Palestine, TX	74750	31.78	-95.71	119
19	PLT	Platteville, CO	N/a	40.13	- 104.6	N/a
20	PRCO2	Purcell, OK	74649	34.98	-97.52	330
21	RWDN1	McCook, NE	74433	40.09	-100.65	800
22	SLAI4	Slater, IA	74449	41.90	-93.7	315
23	VCIO2	Vici, OK	74640	36.07	-99.22	647
24	WDLM5	Wood Lake, MN	74341	44.67	-95.45	318
25	WNCI2	Winchester, IL	74556	39.66	-90.48	169
26	WNFL1	Winnfield, LA	74753	31.90	-92.78	93

The location of the sites is also given in figure 2.3.

The raw wind profiler data, used for this study, consist of triplets of zonal *u*, meridional *v* and vertical *w* components of wind velocity obtained for each range gate (altitude level) from 500 to 16250 m in 250 m increments. The data have 6 minute time resolution and represent approximately 2-minute averages of each component. Data were archived as monthly files for each wind profiler, separately for zonal, meridional and vertical components. The size of each station monthly component file is ~ 3.3 Mb, and total archive is about 9 Gb.

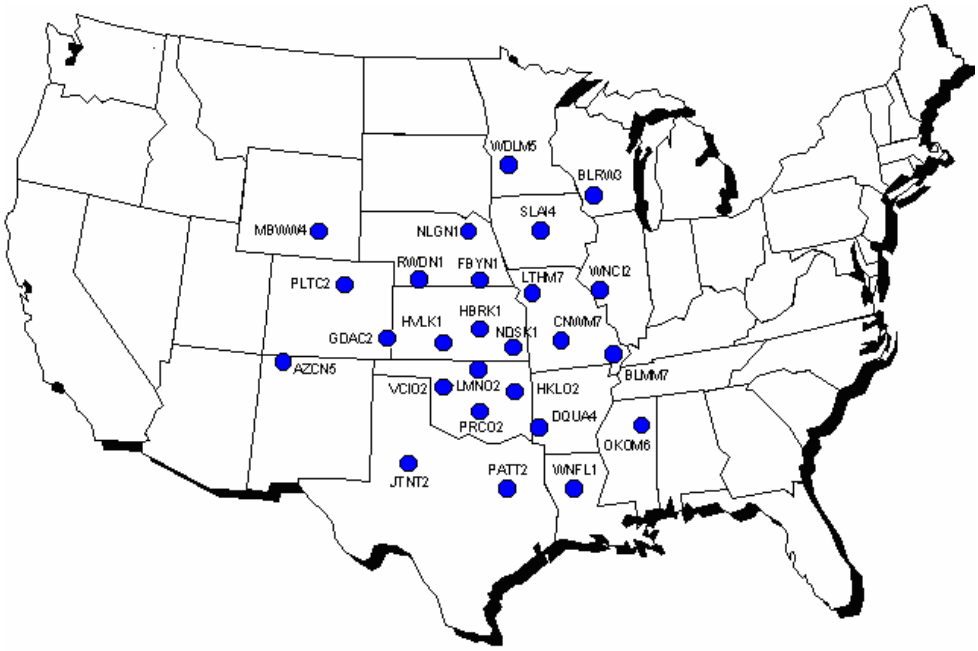

Figure 2.3. Locations of the NPN Wind Profiling radars used for the study. (Modified from http://www.profiler.noaa.gov/npn/npnSiteMap.jsp)

In general, the data coverage is good, with data available more than 80% of the total time. An example of the time and altitude coverage, typical for the dataset, is shown in figures 2.4 and 2.5. The decreased coverage (up to 20% time available) was observed on April 2003 and May 2004. There are also some gaps in the data, the largest being

about 2 months (May-June 2003) due to network data delivery problems and profiler maintenance.

As mentioned above, the wind profiler signals, besides carrying the information about the "true" wind, are contaminated by a large number of distortions, due to a variety of atmospheric phenomena affecting the scattering physics. Instantaneous sampling of multiple atmospheric processes is characterized by:

- Variety of temporal scales (max variability at ~10 min.);
- Variety of spatial scales, reduced to temporal variations in measured time realizations;
- Significantly different magnitudes.

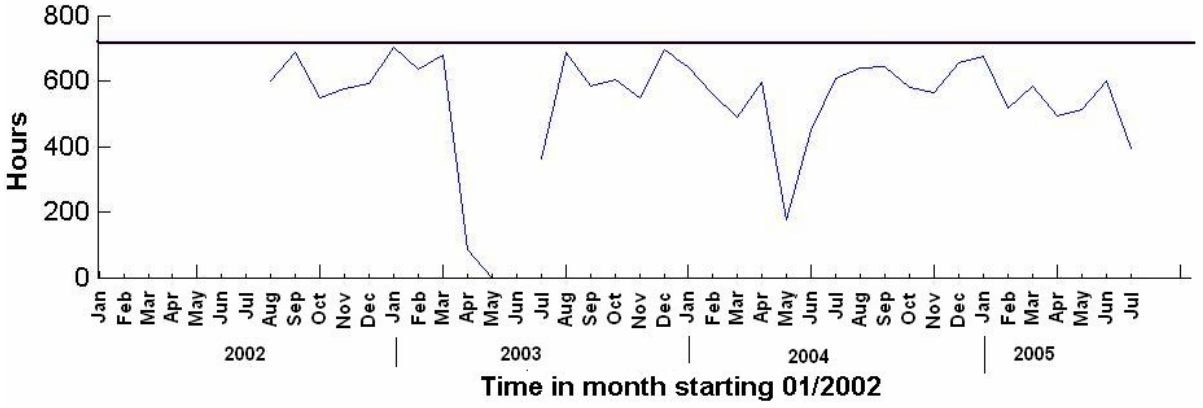

Figure 2.4. Typical data coverage for dataset used in calculations. The data for the MBW profiler at 8 km are shown, with maximum possible monthly coverage (720 hours) plotted as a horizontal line at the top of the graph.

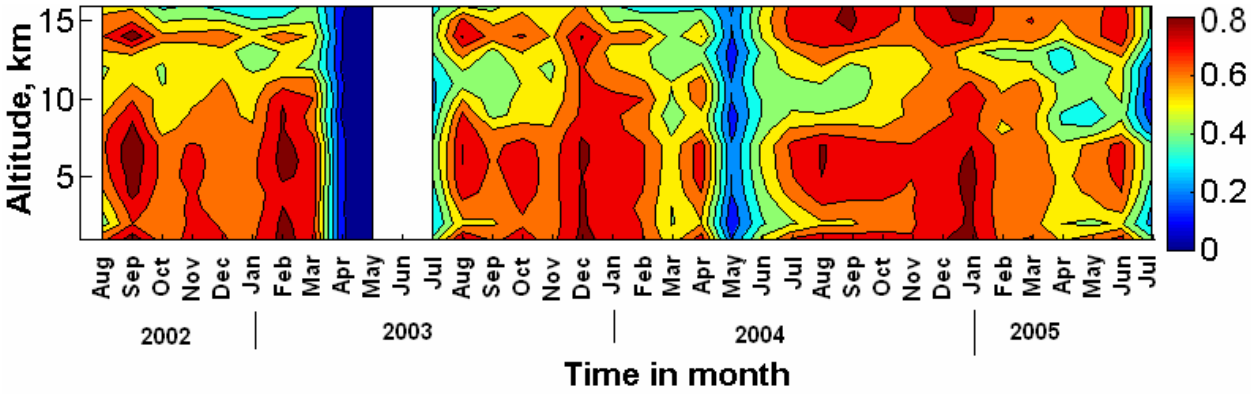

Figure 2.5. Typical altitude/time coverage for the dataset. The data for the MBW profiler are shown; shading represents the fraction of the time when profiler data were available.

In order to ensure the removal of clutter and to achieve needed data quality, we have developed data processing algorithms that were consecutively applied to raw 6-minute NPN data. In the first step, the "instantaneous" profiles of the raw zonal *u*, meridional *v* and vertical *w* components of wind velocity were processed in the altitude domain. After that, the time realizations of the *u*, *v* and *w* at the fixed altitude were processed in the time domain. Diagrams of the data processing algorithms implemented in this study, are presented in figures 2.6 and 2.7.

The threshold values for filtering and data editing were determined based on physical limitations to the measured value (wind velocities). In the altitude domain approximation of the missing data in each profile was performed for no more than two consecutive missing data points (500m gap in altitude). Smoothing was performed by a 5-point running window. In general, this algorithm of height-domain filtering follows the one described by Rastogi (1986) and Rastogi (1989).

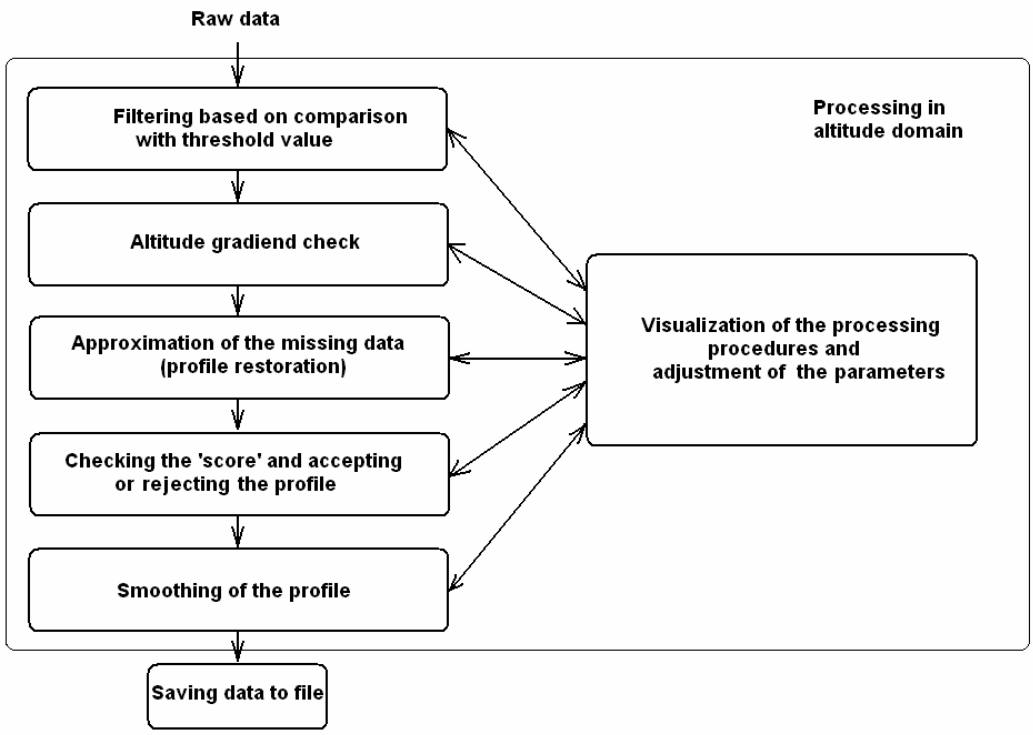

Figure 2.6. Diagram of the data processing in the altitude domain.

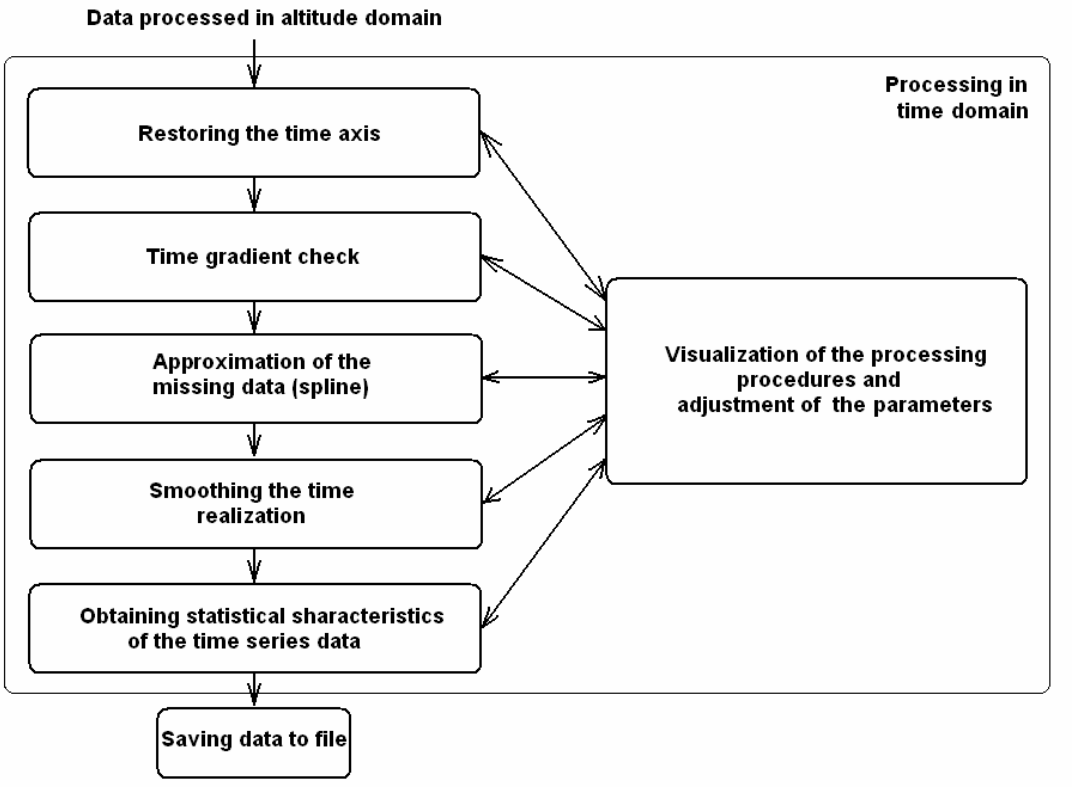

Figure 2.7. Diagram of the data processing in the time domain.

Algorithms of the data processing in the time domain represent the further development of author's previous work (Oleinykov and Karabanov, 1997) and contain the following steps:

- restoring the time axis (finding gaps in the time domain);
- checking the time gradients of wind velocities at each altitude level, in comparison with a predefined threshold;
- approximation of the missing data (no more than 3 points, or 18-minute gap) by a spline approximation;
- smoothing the time realizations of velocities at the fixed height with a 5-point running mean;
- averaging the data to get hourly and monthly means;
- obtaining the departures from the mean;
- visualization of the data, that allows for control of the editing procedures and presents the results in a format convenient for analysis.

Data processing algorithms were implemented using the *MATLAB 6.5®* software package.

After initial data processing it was found that data from the PLT profiler in general were significantly less reliable and consistent than from the other profilers. The data from the PLT wind profiler also were only available as hourly averaged data. Therefore comparison with 6-minute resolution data from other stations would not be logical. In order to minimize resulting biases in correlation plots, distributions, etc. we have excluded the PLT data (station 19 in table 2.1) from most of the following analysis.

2.5. Precipitation data

In chapter 3 the profiler-measured winds will be compared to the rainfall rates for corresponding locations. As the rain proxy the NCAR/NCEP reanalysis monthly averaged surface rainfall rate was chosen, for several reasons. First, it was intended to maintain consistency with other data, as NCAR/NCEP reanalysis vertical and horizontal wind data were also used for comparison with profiler measurements. Second, even though on a short timescale and for local features, raingauge and satellite observations have significant differences with reanalysis rainfall (Janowiak at al., 1998), on a longer timescales for central North America the measurements and reanalysis compares well (same reference).

At the same time smoothed reanalysis data might not be a good representation of actual rain at the profiler site for shorter time and spatial scales, therefore we have used the second source of precipitation data – from the land-based observational network, distributed by National Climatic Data Center (http://www.ncdc.noaa.gov/oa/land.html). Despite the very favorable location of some raingauge stations in close proximity to wind profiling sites (e.g. 1 km for MBW, or 9 km for DQU, as shown in table 2.2), the average distance is ~26 km. At this spatial scale the precipitation features characteristic of the profiler location might be partially lost, but we expect that nearer raingauges would still give a better estimate of precipitation over a profiler site than the reanalysis data.

A correlation between monthly averages of reanalysis-predicted rainfall rate and raingauge measurements for the locations of 26 wind profilers is presented in figure 2.8.

Table 2.2 National Climatic Data Center raingauges used for this study. The three raingauges closest to each profiler site are shown, with distance to profiler indicated; the ones used for comparisons are in bold; the ones with no data available for research period are highlighted.

Profiler	ID #	Raingauges					
		1st closest		2nd closest		3rd closest	
		Raingauge ID	Distance, km	Raingauge ID	Distance, km	Raingauge ID	Distance, km
AZC	1	**293142**	41	055531	75	057656	112
BLM	2	**230022**	26	235207	29	238700	35
BLR	3	478164	32	474821	39	**474404**	40
CNW	4	**234825**	18	235307	32	235834	63
DQU	5	**031952**	9	032810	11	032020	23
FBY	6	**253737**	32	253735	33	250620	65
GDA	7	**053477**	36	140802	66	057866	78
HBR	8	**145039**	25	143366	47	142135	66
HKL	9	344506	55	344098	56	**346638**	56
HVL	10	147965	38	**140326**	98	140620	99
JTN	11	**414570**	53	411903	71	415358	73
LMN	12	**347556**	34	141233	41	347196	43
LTH	13	**234387**	29	237114	41	237862	46
MBW	14	**486120**	1	488192	53	487995	80
NDS	15	**143954**	13	142430	20	145536	21
NLG	16	**256720**	30	257347	39	256655	39
OKO	17	**229003**	22	224265	25	220021	48
PAT	18	**416757**	12	416335	68	414591	68
PLT	19	**053553**	25	053546	27	052731	38
PRC	20	**346859**	34	341750	45	344052	50
RWD	21	**255312**	14	145787	55	140441	56
SLA	22	**130200**	15	130241	25	137985	34
VCI	23	**348708**	28	342334	63	349404	64
WDL	24	**213311**	17	218323	53	218729	55
WNC	25	**114442**	32	116837	36	113666	45
WNF	26	**169803**	11	166582	39	165935	53

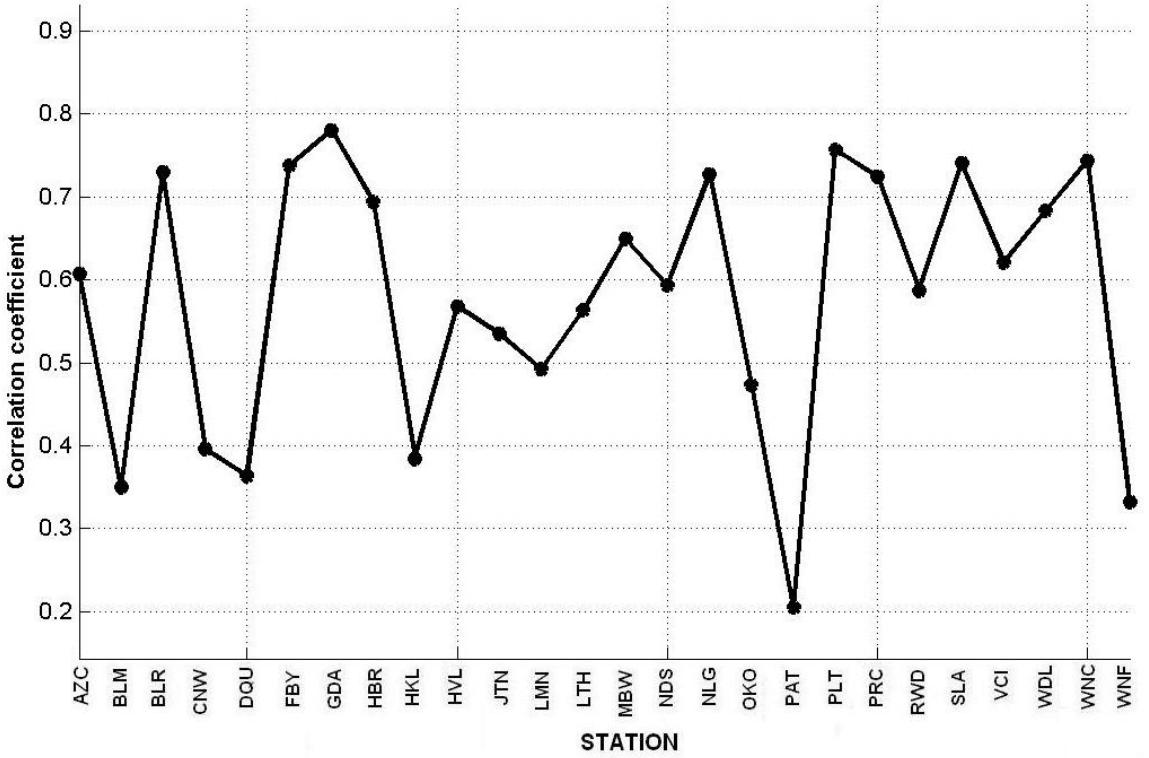

Figure 2.8. Correlation between reanalysis rainfall rate and raingauge rain data for 26 profiler locations.

The correlation coefficient for most of the stations is within 0.4-0.7. It is interesting, that the highest correlation is found not for locations with shortest distance between profiler and raingauge sites (MBW, DQU), but for stations with distances 15 - 30 km: BLR, FBY, GDA, HBR, NLG, PLT, SLA and WNC. These are locations with average rainfall rates, 1.5 - 3 mm/day, in the middle of the precipitation rate range of all the stations, and located in the central/north part of the area covered by the profiler network, north from 37^{o} N. The lowest correlation appears at the locations with the highest rainfall, at the extreme south-eastern locations. Observed disagreement between the two precipitation data sources indicates that different mechanisms are responsible for the precipitation in the two regions, one – probably stratiform and spatially uniform and therefore well-captured by reanalysis, and another – dominated by local convective precipitation

patterns. Therefore, neither of the data sources can be used explicitly. Rather, both sources will be used for comparison. Reasonable caution should be exercised when discussing these comparison results.

An estimate of average rainfall over the study period based on reanalysis and raingauge data for profiler site locations is presented in Table 2.3. It was obtained as an average of monthly precipitation rates for 36 months at each site. The group of sites with highest rainfall includes BLM, DQU, OKO and WNF. Lowest precipitation rates are observed at AZC, MBW, JTN, VCI and HVL.

Table 2.3. Average NCAR/NCEP reanalysis and raingauge rainfall rates for profiler sites. The sites with largest rainfall are highlighted.

Profiler Site	Profiler ID #	Average NCEP/NCAR reanalysis precipitation rate, mm/day	Average Raingauge precipitation rate, mm/day
AZC	1	1.2	0.7
BLM	2	4.5	2.9
BLR	3	2.6	2.1
CNW	4	3.7	2.2
DQU	5	4.1	2.7
FBY	6	1.9	1.6
GDA	7	1.8	1.3
HBR	8	1.9	2.3
HKL	9	2.9	2.1
HVL	10	1.6	2.3
JTN	11	1.4	1.9
LMN	12	1.9	2.1
LTH	13	2.7	2.0
MBW	14	1.3	0.7
NDS	15	2.6	2.6
NLG	16	1.9	1.8
OKO	17	5.3	4.5
PAT	18	3.7	3.2
PLT	19	1.5	0.8
PRC	20	2.1	2.3
RWD	21	2.1	1.4
SLA	22	2.9	2.4
VCI	23	1.6	1.7
WDL	24	2.3	1.4
WNC	25	3.4	2.2
WNF	26	4.9	3.8

CHAPTER 3

THE LONG-TERM CHARACTERISTICS OF WIND DATA OBTAINED BY THE NOAA PROFILER NETWORK RADARS

3.1 Mean zonal and meridional wind

In this section we present the time-space structure of the *u* and *v* components of horizontal winds obtained a result of data processing procedures described in chapter 2 applied to the NPN measurement database. The derivatives of these data, vertical shear of horizontal wind and variance of the horizontal wind are also presented. Horizontal wind data and especially the vertical shear of horizontal wind, obtained in this section, will later (in chapters 5 and 7) be used to analyze the gravity wave structure and possible generation mechanisms. These data also will make it possible to highlight the specific features of the vertical winds measured by the NPN profilers; to investigate the possible contamination of the vertical wind measurements by the horizontal winds due to antenna pointing inaccuracies and aspect sensitivity.

Typical monthly mean zonal wind component for the WNF and MBW wind profilers is presented in figures 3.1 and 3.2 correspondingly. These two stations were chosen as they are typical examples of two wind regimes that are apparent in the time-height structure of the zonal winds. The first regime which was found most obvious at DQU, OKO, PAT and WNF sites, is characterized by a strong seasonal cycle with single yearly maximum up to 40 m/s at 12 - 13 km in winter (December-February) and

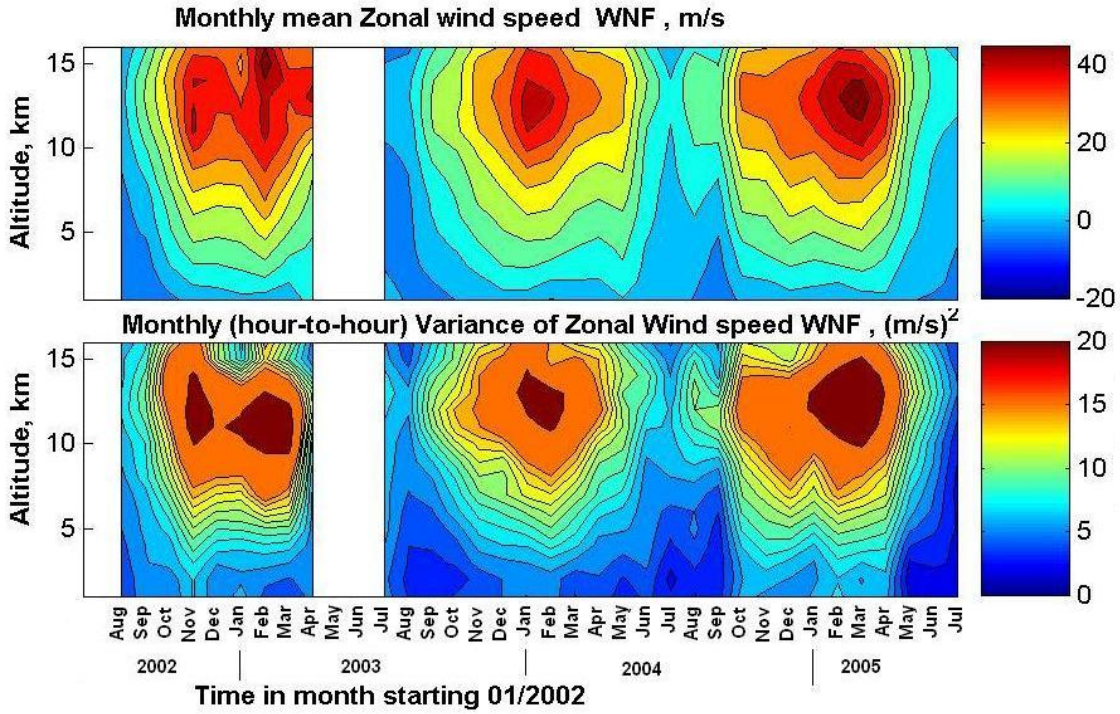

Figure 3.1 Monthly mean zonal wind (upper plot) and variance of zonal wind (lower plot) for the WNF wind profiler. Contour interval is 5 m/s for wind speed and 1.5 $(m/s)^2$ for variance.

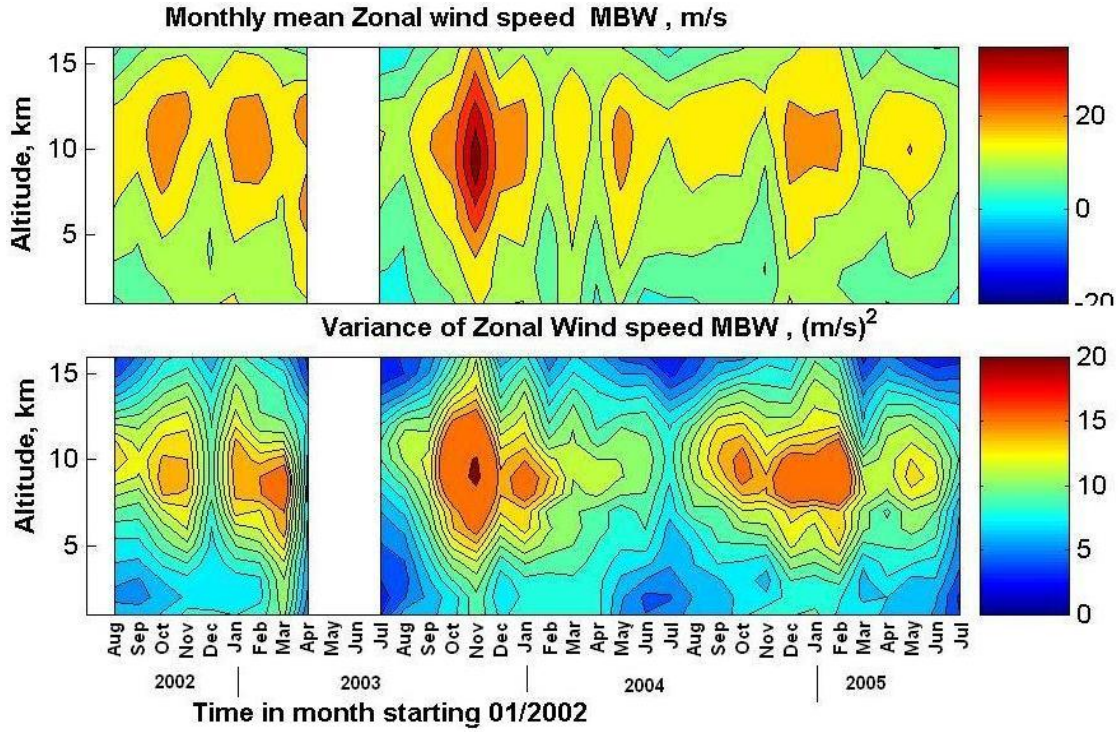

Figure 3.2. Same as fig. 3.1, but for the MBW wind profiler.

weak (<10 m/s) zonal winds in summer. These sites are the southernmost of all profiler sites (compare to fig. 2.3), all located at ~32 - 34 ^{o}N, in the latitude band that is influenced by strong seasonal relocation of the jet-stream. The variance of the zonal wind, calculated as a variance of hourly mean values within a month, follows the zonal mean wind rather closely (lower graph in fig 3.1).

The second regime is characteristic for most of the northern sites and the ones located in mountains (MBW, AZC, WDL, and others). It is characterized by the absence of strong seasonal cycle of zonal wind, with multiple local wind maxima at lower heights (~10km), than for the first regime. The observed decrease of the maximum wind altitudes from the first to the second regimes is consistent with the lower altitudes of the tropopause and the jet-stream for the northerly-located sites. The variance of the zonal wind however does not follow the zonal mean wind pattern that closely. Maxima of the variance are found in winter season, similarly to the first regime, and are observed at altitudes slightly below the maximum wind.

Zonal wind measurements on a timescale of a month correlate extremely well (R=0.9 - 0.97) with Reanalysis data, as shown in figure 3.3, with the exception of three locations with lower correlations: MBW (R=0.8), NLG (R=0.87) and WDL (R=0.83). There appears to be some dependence between the latitude of the profiler site and how similar to reanalysis is the zonal wind. Thus, the most north- and north-west located stations MBW, NLG, BLR, MBW (compare with fig. 2.2), appears to have the most differences with reanalysis.

The meridional wind structure during the observational period is presented in figure 3.4, using the plots for the WNF site as an example.

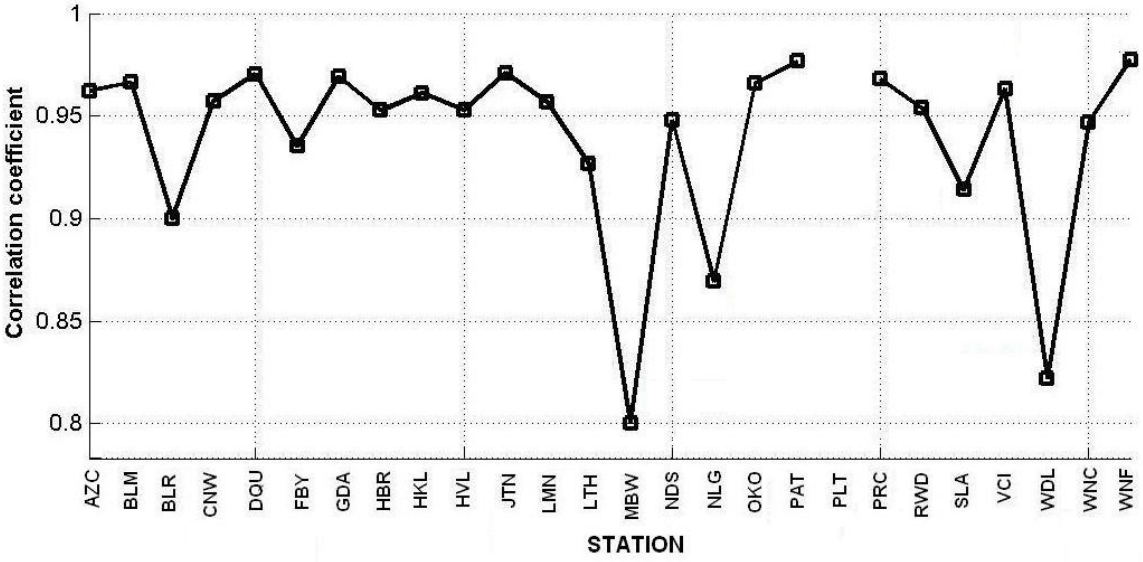

Figure 3.3. Correlation coefficient between 36-month profiler-measured zonal wind and reanalysis zonal wind at 5 km for 25 profiler stations.

Plots for most of the NPN sites look similar, with more pronounced alternation of the direction (sign) of the wind, for northern part of the network. The areas of positive (negative) winds are stretched from lower troposphere up to 15 km, forming band-like structures with 3 to 5 month period. The monthly mean magnitudes of the meridional wind typically do not exceed ~10 m/s. The variance of the meridional wind behaves more like the one for the zonal wind, with a prominent maximum in winter season and smaller secondary maxima in spring, both at 9 to 10 km altitude.

The vertical shear of horizontal wind (both directional shear and speed shear) was calculated as a wind speed or direction difference over a 250-m layer scaled to units of ms^{-1}/km and °/km, using the profiler-derived hourly mean *u* and *v* velocities. In order to compare the primary wind field and corresponding vertical shear of the wind, the time – altitude fields of the shear for the WNF and MBW wind profilers will be examined, as shown in figures 3.5 and 3.6 correspondingly.

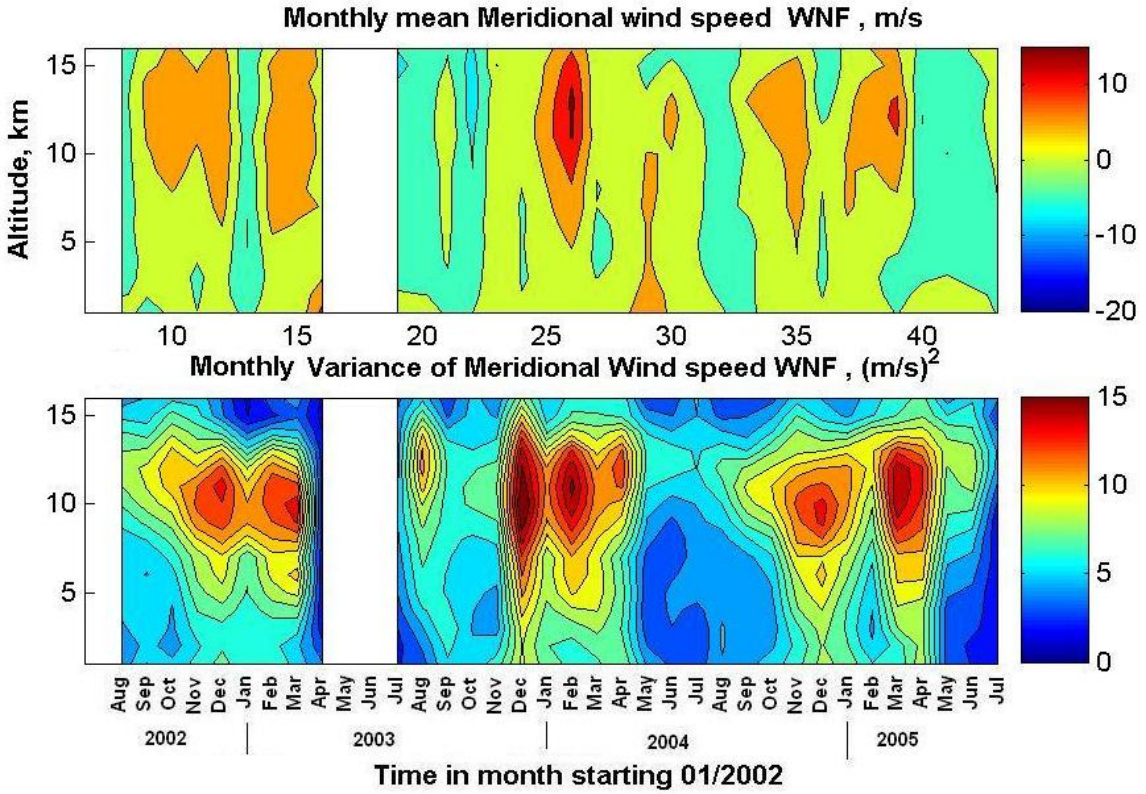

Figure 3.4 Monthly mean meridional wind (upper plot) and variance of meridional wind (lower plot) for the WNF wind profiler. Contour interval is 5 m/s for wind speed and 1.5 $(m/s)^2$ for variance.

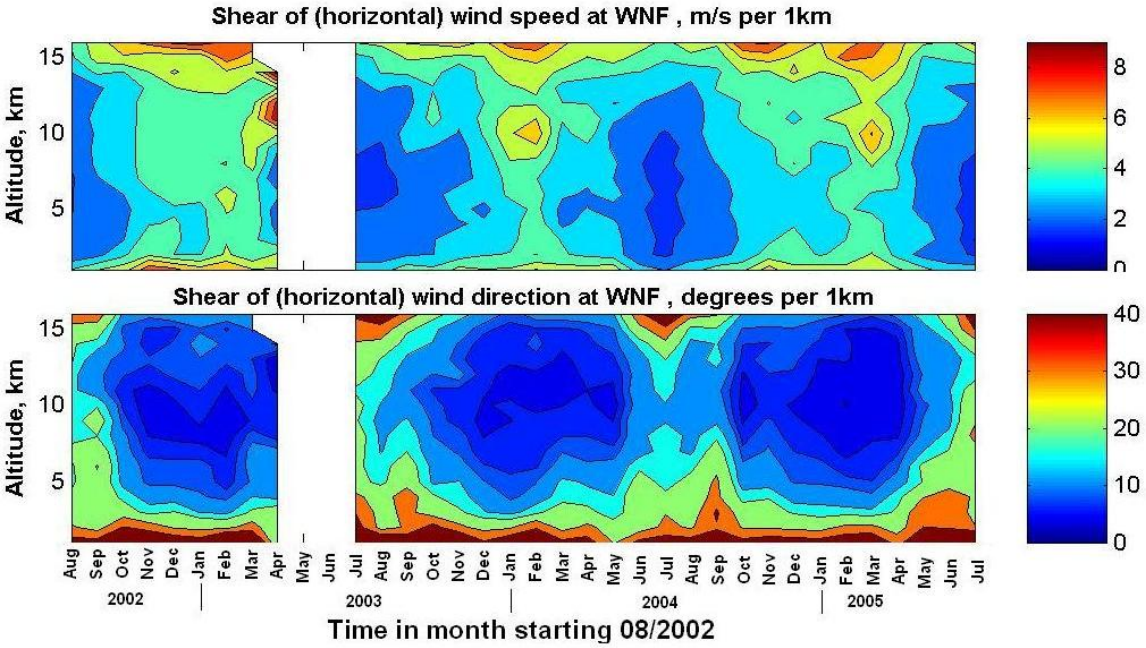

Figure 3.5 Monthly mean vertical shear of horizontal wind speed (upper plot) and direction (lower plot) for the WNF wind profiler.

Comparison of fig. 3.5 and fig. 3.1 shows that for the WNF site the maxima of the speed shear coincide with maxima of the zonal wind in time, but located *below* the area of the strongest winds (12 - 13 km) , at ~ 9 km. Unlike the wind maxima, that are observed in the upper troposphere/lower stratosphere, the areas of increased wind speed shear are stretched over the all the troposphere, from the lower troposphere up to 15 km, forming the band-like structures that are narrower in the mid-troposphere and wider in the lower and upper troposphere. Seasonal structure is clearly visible in plots for both the speed shear and direction shear, but the phase between them seems to be shifted by ~ 6 month. The directional shear is minimum in the areas of horizontal wind maxima, and shows the enhancement in summer season when the winds are weak, being the largest in the lower and upper troposphere. The timing and altitudes of this summer directional shear enhancement does not correspond to the local strengthening of the meridional winds (not shown). The time-altitude behavior of the wind shear, shown in fig. 3.5 is typical for the southernmost profiler sites (DQU, PAT, OKO, WNF).

For the MBW profiler site comparison of fig. 3.6, 3.5 and fig. 3.2 indicates less pronounced seasonal structure of the wind shear, consistent with less pronounced structure of the zonal wind. Winter increase of speed shear and summer increase of directional shear still could be distinguished, but are not so obvious.

In general, for all profiler sites (with possible exclusion of MBW) the correlation between zonal wind and vertical shear of horizontal wind is good in the troposphere, as shown in figure 3.7. In this figure, the correlation coefficient between the zonal wind and the vertical shear of horizontal wind calculated for 36 month at 5 km altitude is plotted for 25 wind profiler stations.

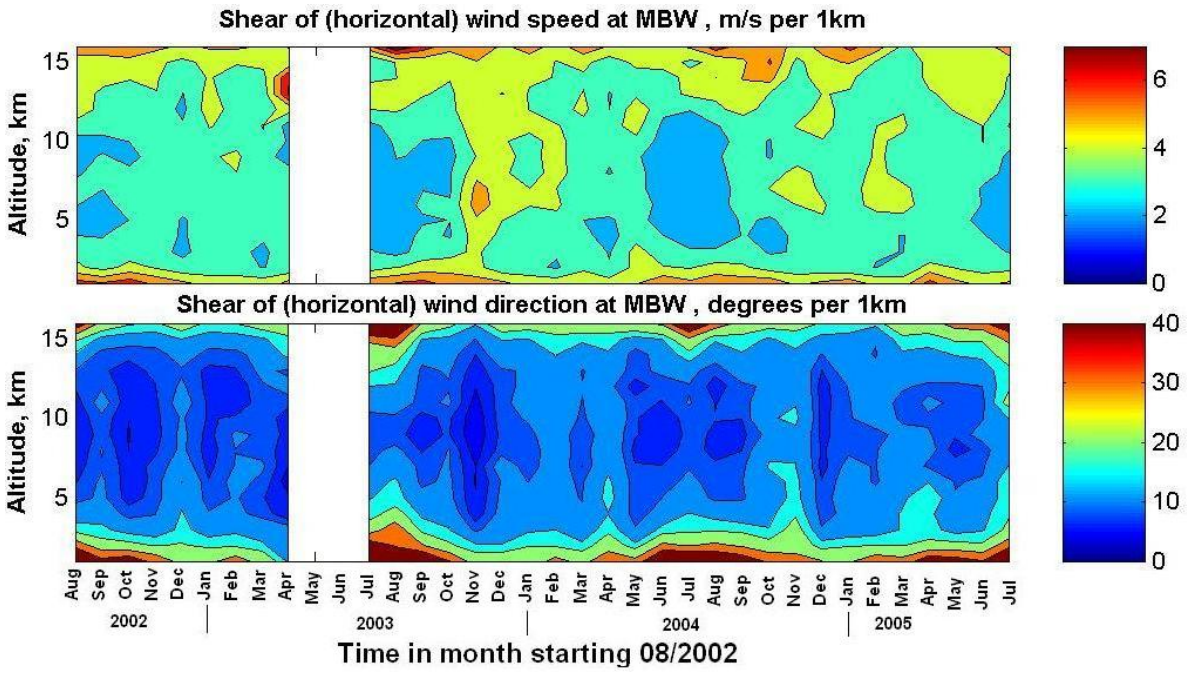

Figure 3.6. Same as fig. 3.5, but for the MBW wind profiler.

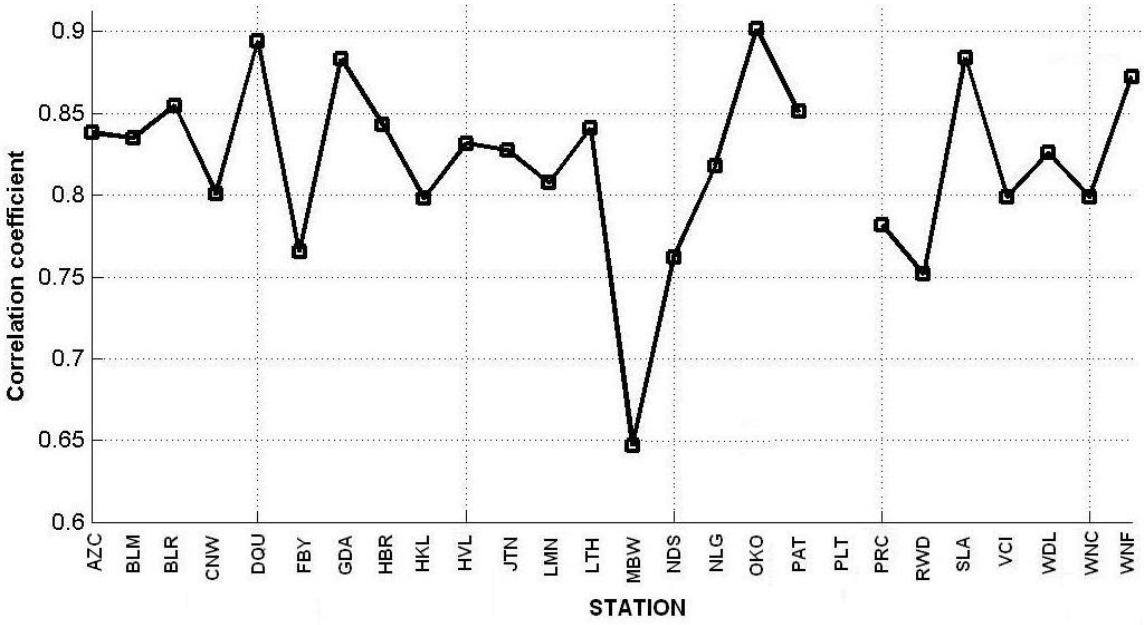

Figure 3.7. Correlation coefficient between zonal wind and vertical shear of horizontal wind at 5 km for 25 profiler stations.

Note that the lowest correlation is observed at MBW and is equal to ~0.65, while for southern sites (DQU, PAT, OKO and WNF) it varies between 0.85-0.9. It can be concluded, therefore, that vertical wind speed shear is strongly dependent on zonal wind speed for most of the locations, with the exception of MBW, where the proximity to the Rocky Mountains and strong mountain gravity wave activity might be affecting the wind shear.

3.2 Vertical winds measured by the NPN

As was mentioned previously, "instantaneous" measurements of vertical wind possess very high variability both in time and altitude domain, due to the large number of processes that are incorporated into vertical air motions. As an example of such measurements, the vertical profiles of vertical wind are presented in figure 3.8 (altitude domain), and in figure 3.9 (time domain). The observed instantaneous values of vertical wind are within ±0.4 m/s, with significant variability in both the altitude and time domains. The cases with large negative values of the vertical motions (e.g. 5-7 km on the right graph fig. 3.8 and measurements number 220 - 260 in fig. 3.9) most likely represent contamination of the wind data by rain. This issue will be discussed later in chapter 4.

Much more useful for observing the atmospheric processes are smoothed and averaged vertical wind data on the scales of days. As an example, demonstrating the potential of vertical wind observations in the analysis of atmospheric processes, the observations of a cold front and tropopause fold passage over the WDL profiler are presented in figure 3.10.

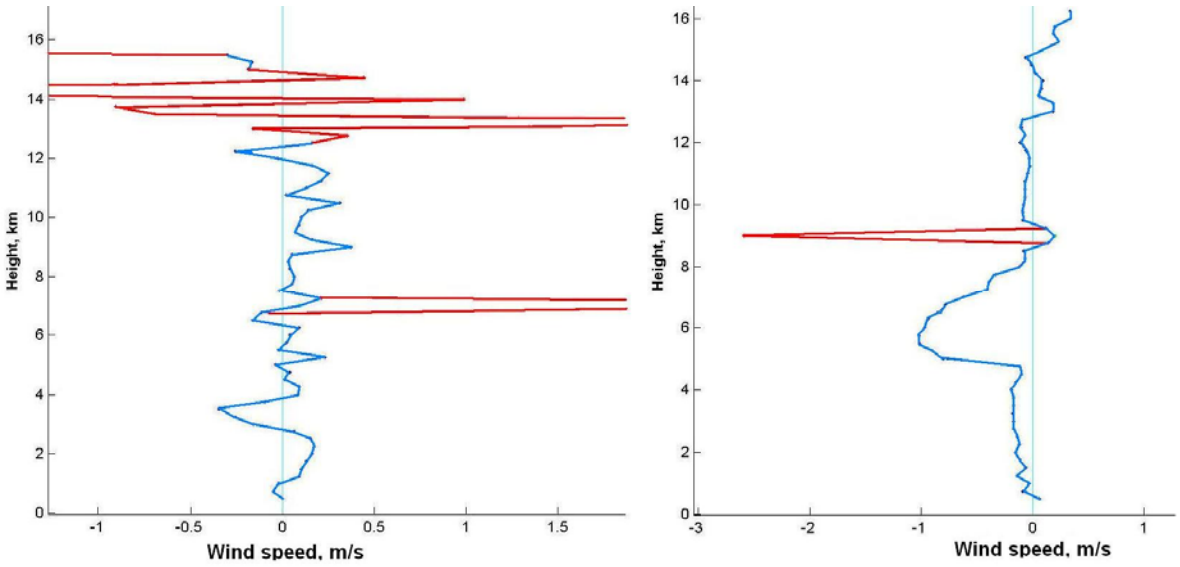

Figure 3.8. Instantaneous raw (red) and edited (blue) vertical profiles of vertical wind measured by the OKO profiler in winter (left graph) and summer (right graph).

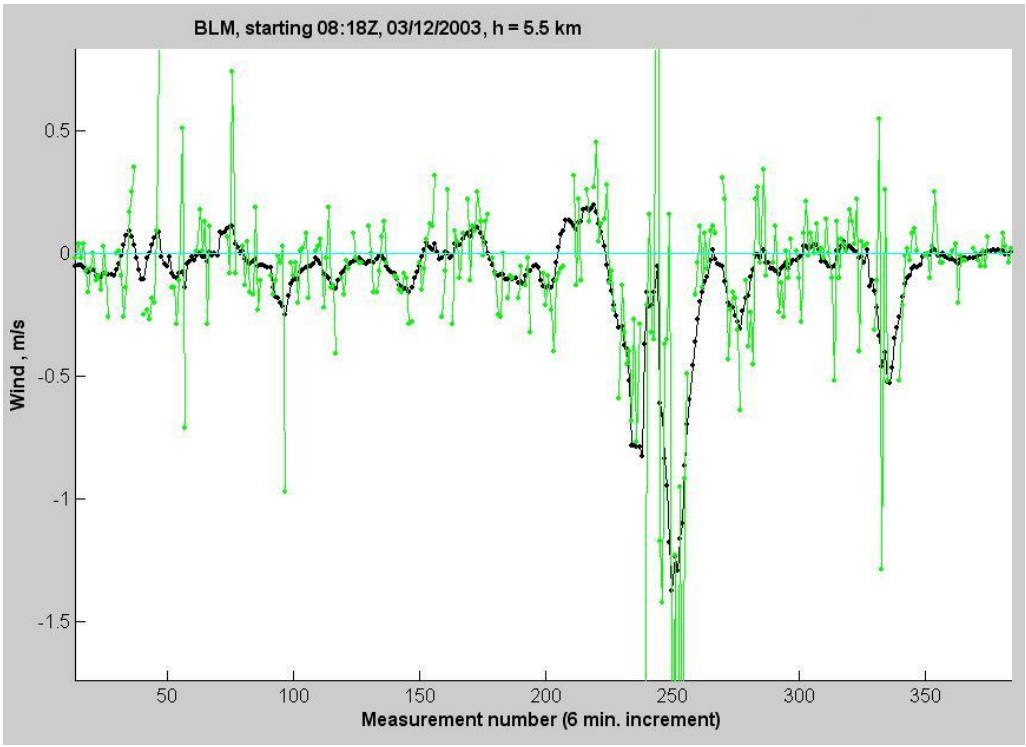

Figure 3.9. Raw (green) and edited (black) time realizations of vertical wind measured by the BLM profiler at 5.5 km in spring 2003, with 6-minute time resolution.

A short-wave, fast-moving trough formed in the upper-air flow over the Dakotas and the northern part of Nebraska on 28 July 2002 (not shown). The trough moved over 600 km toward the east during a 12-hour period, and reached the western part of Wisconsin by midday on 29 July 2002.

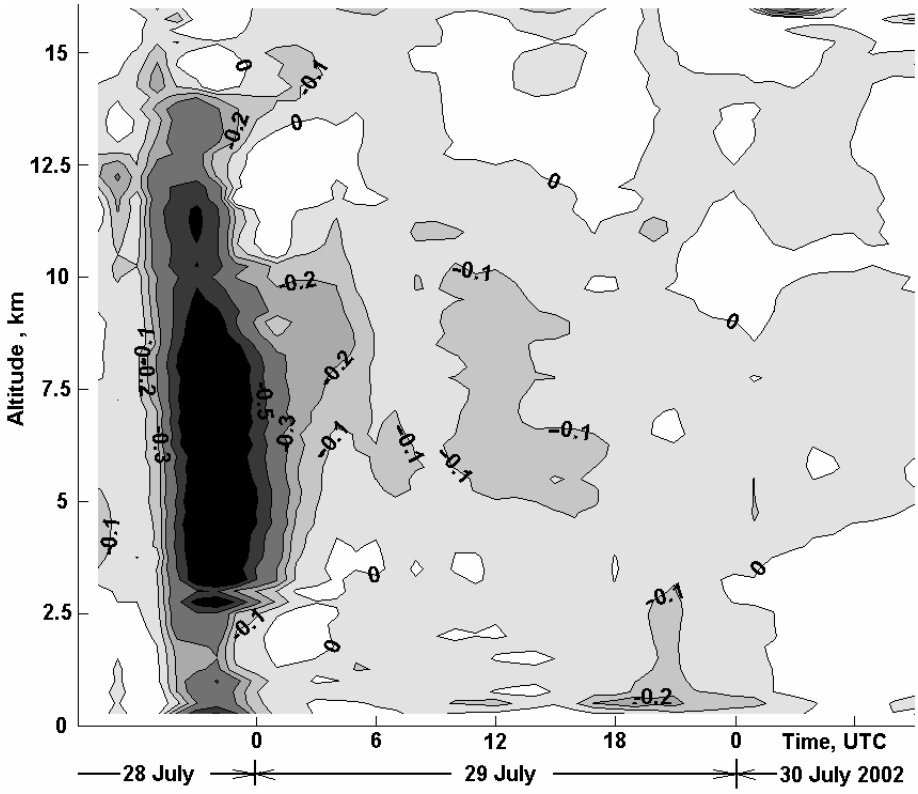

Figure 3.10. WDL wind profiler data during a frontal passage: a time-height field of vertical wind velocity; contours are plotted at 0.1 m s^{-1} intervals, with downward velocities shaded. Strong downward velocities in the left part of the plot from 18-23 UTC on July 28th are due to rain.

The middle part of the trough at the 300 mb level passed over the wind profiler at Wood Lake, Minnesota (WDL) at approximately 08 UTC on July 29th. Potential vorticity (PV) values in the vicinity of the western flank of the trough reached 4 PVU, and satellite water vapor charts for 14.15 UTC 29 July 2002 indicated (not shown) an area of dry air in the southwestern part of the trough, supporting the assumption that tropopause folding

was happening. The time when the tropopause fold was advected over the location of the profiler was defined using consecutive PV and water vapor charts. During the time of the fold passage (06-16 UTC 29 July 2002, Figure 3.10), the air motion was predominantly downward, with vertical velocity being within -0.1…-0.2 m/s over altitudes up to 12 km. Note that above the fold area, at altitudes 11-12 km and up, the air is mostly ascending, which is in agreement with classical fold structure (e.g. Neiman et al., 1992).

In the rest of this chapter we will focus on the long-term mean characteristics of the vertical wind as measured by the NPN radars.

Typical sample frequency of occurrence of the vertical wind velocities for the 36-month measurement period for the boundary layer, mid- and upper troposphere are presented in figure 3.11 for the AZC and WNF profilers and in APPENDIX B for the rest of the sites. A Gaussian curve was individually fitted to each sample distribution to facilitate comparison. Each curve is based on ~ 200 000 individual vertical wind profiles.

For the boundary layer, distributions of measured velocities is clearly non-Gaussian, with an overall shift of the distribution toward negative values and significant 'wings' to the distribution at ~ -0.5 m/s. Distribution is skewed toward negative velocities, that is especially noticeable for locations with higher average rainfall rates (shown in table 2.3) – BLM, DQU, OKO, WNF. For these locations the distribution curve is wider in the boundary layer than in mid-troposphere, and the opposite is true for the rest of the locations.

For the midtroposphere the distribution of velocities is more Gaussian-like, with some excessive frequencies at -0.1…-0.3 m/s and at ~-0.5 m/s (e.g. left middle plot in fig.

3.11) at most locations. A nearly Gaussian distribution in midtroposphere is observed at the BLM, BLR, CNW, FBY, HKL, PAT, WNF sites.

In the upper troposphere the distribution of velocities is closer to Gaussian for most of the stations, with some excessive frequencies at positive velocities ~ 0.1 - 0.25 m/s and at negative ~ -0.5 m/s (e.g. lower right plot in fig. 3.11). The conclusions from the analysis of distributions can be summarized as follows:

1) distributions are clearly non-Gaussian for lower and mid- troposphere;

2) boundary layer distributions are strongly affected by precipitation;

3) there are three diapasons of vertical velocities where most significant difference form Gaussian curve are observed: at -0.1…-0.3 m/s , -0.5…-0.6 m/s and 0.1…0.25 m/s.

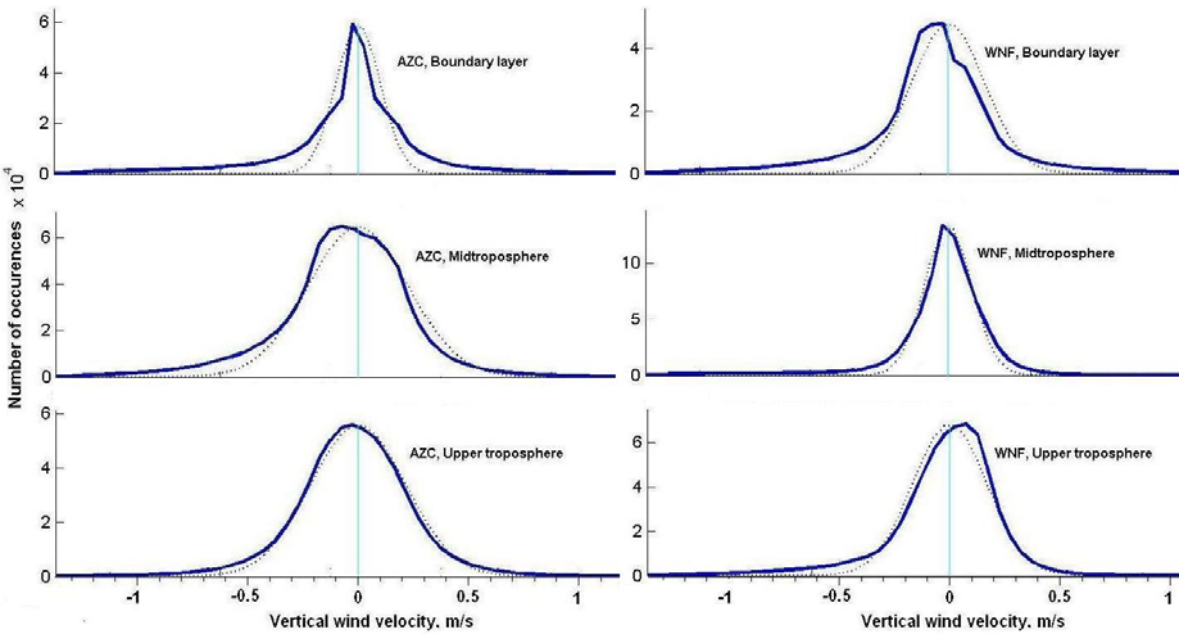

Figure 3.11. Frequency of occurrence of the vertical wind velocities obtained for the 36-month measurement period for the AZC (left plots) and WNF (right plots) profiler sites. Upper plots are for boundary layer, middle – for midtroposphere, and lower for upper troposphere. A Gaussian curve is fitted to each plot (thin dashed line).

A different description of the vertical wind, showing its behavior in both the altitude and time domains, can be obtained if monthly averages of the vertical wind are plotted as time-altitude fields similar to figs. 3.1 and 3.4. We have used the procedures described in chapter 2 to obtain the monthly mean vertical wind data for 25 NPN profiler sites for the 36-month study period. A sample time-altitude plot of vertical velocities measured by WNF is shown in figure 3.12; the plots for the other sites are presented in APPENDIX C.

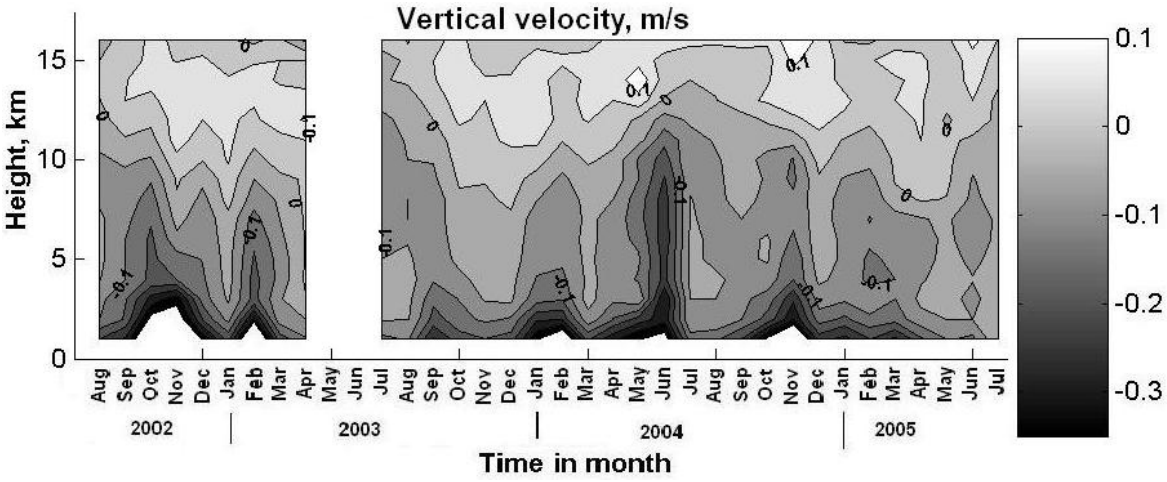

Figure 3.12. Time-altitude plots of monthly mean vertical velocities measured by the WNF during 36-month observation period.

The structure of the vertical winds at the WNF site has several features similar to the other locations:

- Periodic enhancements of the vertical velocity in the lower troposphere, at 1-3 km, that sometimes extend to 5-10 km. These enhancements have large negative velocities, up to -0.4 m/s, while in the most of the troposphere outside of these events the velocities do not exceed -0.05…-0.1 m/s
- The periods of large negative velocities are repeatedly occurring in late fall (October-December), winter (February) and in summer (June), the periods

between maxima are typically 3-4 months, but the timing and duration vary from year to year.

- Above ~10-12 km, predominantly downward velocities change sign and become positive.
- Locations with high rainfall rates have larger downward velocities in lower/midtroposphere. The opposite is true for low-rainfall locations.
- In general, the vertical wind structure is variable and complex, but bears definite similarities for closely-located sites.

Averaging the above time-altitude plots along the time axis for the whole measurement period produces long-term mean vertical profiles of vertical wind. The 3-year average profiles of vertical wind were obtained for all profiler sites, and plotted together with averages obtained for each season separately. The plots for the WNF profiler are shown in figure 3.13, while the plots for the other stations are given in APPENDIX D.

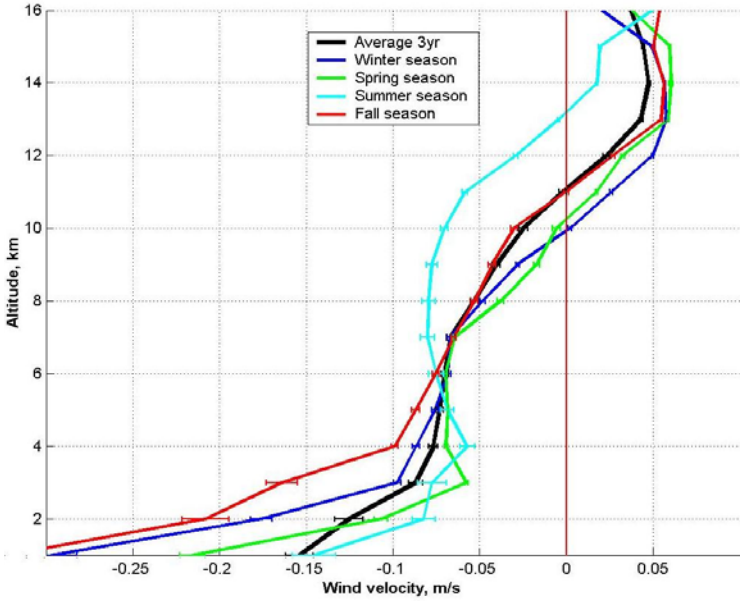

Figure 3.13. The 3-year average profile of vertical wind and seasonally averaged profiles for the WNF site. The error bars at $\pm\sigma$ are shown on each curve.

The prominent features of the profiles can be identifies as follows:

- In the troposphere, for all locations the long-term mean velocities are negative (downward) with the values for the midtroposphere about -7.5 cm/s, significantly decreasing in the lower troposphere and boundary layer, down to -10…-15 cm/s; in the upper troposphere the negative vertical velocities decrease in magnitude, and change sign at ~ 10 - 12 km, becoming positive. The stronger negative velocities in the lower troposphere are observed at the locations with higher annual rainfall.
- At some locations (DQU, HBR, NLG, PRC, VCI, WNC) the velocity sign change in the upper troposphere/stratosphere is not present, or minimal.
- The altitude at which the velocity changes sign is close to that of the maximum horizontal winds; it does not show any noticeable dependence on latitude.
- The maximum positive velocities reach 2.5 cm/s at ~ 14 km height, and up to 5 - 7 cm/s for HKL, JTN, OKO, and WNF.
- On average, the difference in vertical wind speed between seasons is about 2.5 cm/s, being minimal for locations with minimum precipitation (AZC, MBW, JTN, in table 2.3); the highest difference between seasons is observed at the NLG.
- The average summer profile typically has the most deviation from the mean and other season profiles; in the upper troposphere (above 5 km) the summer mean profile is more negative than for the other seasons, with 2.5 - 5 cm/s negative shift from the mean profile.

The conclusions from the analysis of the mean profiles in general confirm the results of the analysis of the wind velocity distributions, that vertical velocity measurements below

5 km are significantly affected by precipitation. Stronger negative velocities in the upper troposphere during summer are probably the result of the vertically developed convective events, and hydrometeors being present at higher altitudes than during the other seasons.

It is interesting to compare the results presented here with similar measurements from the literature. The average vertical velocity profile for January-April 1990, obtained with the Flatland VHF wind profiler (Nastrom and VanZandt 1994), is shown in figure 3.14. This profile is typical for VHF radars in midlatitudes, e.g. Aberstwyth MST radar (Worthington et al., 2001) .

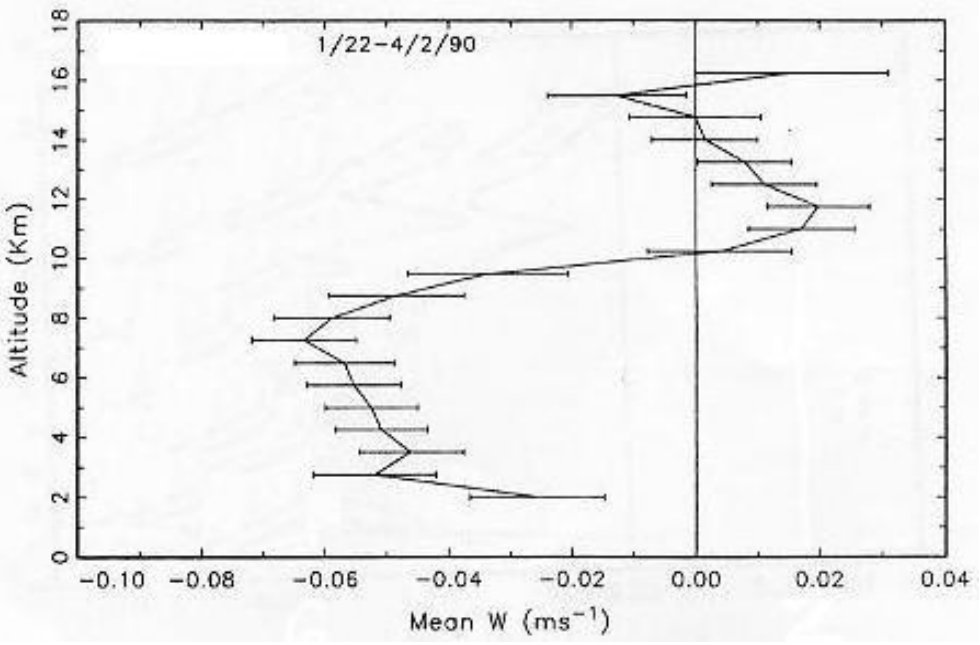

Figure 3.14. Average vertical profile of vertical velocity above Flatland, obtained by Nastrom and VanZandt (1994).

The largest difference between profiles is observed below 3 - 4 km, where UHF profilers have larger negative velocities, up to -0.14…-0.25 m/s in the boundary layer. The magnitude of the negative vertical velocities for UHF wind profilers in midtroposphere (this study) is about 2.5 cm/s larger than the value of ≈ -5.2 cm/s

obtained by Nastrom and VanZandt. The altitude at which the velocity changes sign is in the vicinity of 10 km for Flatland (the latitude of Flatland site is 40.5°N, about the same as for PLT, RWD and FBY), which is 1 - 2 km lower than that typical for our results. It is possible that this difference is a reflection of seasonal and annual changes, as the Nastrom and VanZandt study covers only one season. The magnitude of the ascending motion in the stratosphere (for those locations where change of sign is observed) is larger for our study, being 2.5 - 5 cm/s versus 2 cm/s for Flatland.

In order to assess the hypothesis that precipitation is responsible for the increased bias of vertical wind that is observed in the lower troposphere, the correlation of mean vertical velocities measured at 1 km height, versus rainfall rates were plotted for 25 wind profilers, as shown in figure 3.15.

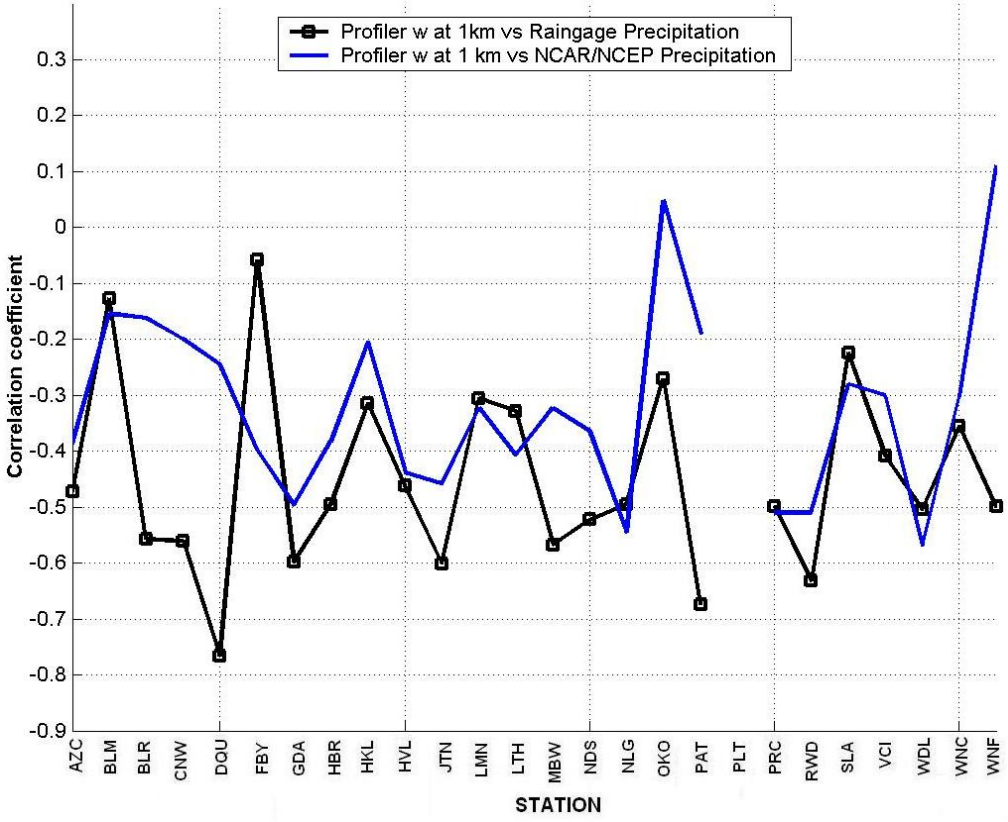

Figure 3.15. Correlation coefficient for vertical wind and rainfall rate at 1 km for 25 wind profiler sites.

The correlation was calculated using both reanalysis and raingauges rain data. The correlation coefficient is negative, is larger for raingauge data than for reanalysis and reaches -0.77 for DQU, the station which both has the high average rainfall rate and is located close to the raingauge (9 km, see tables 2.2 and 2.3). The second highest correlation of -0.68 is found at PAT, which is also close to it's corresponding raingauge (12 km). The correlation varies between -0.3…-0.6 for most of the stations, and is minimal for locations with distance from the nearest raingauge of ~30 km, e.g. FBY and BLM. It seems reasonable to conclude, that if the rainfall data sources were located in the immediate vicinity of the profiler sites, the correlations would be even more significant (and negative) for all sites. This conclusion supports the suggestion that a significant part of the negative vertical velocities observed in the lower troposphere are due to the contamination of the clear air signal by scattering from raindrops, that have substantial negative vertical velocities. The increase in rainfall rates that would produce the decrease (larger negative values) of profiler-observed vertical velocities explains the negative sign of the correlation.

If the above suggestion is true, then the variance of the vertical wind is expected to be high in the lower troposphere (as largest negative *w* is observed in the lower troposphere), and to strongly depend on rainfall. The average over the 36-month period in the variance of the vertical wind for each profiler site is shown in figure 3.16, and the correlation coefficients between rainfall rate and profiler *w* variance for the boundary layer and midtroposphere – in figure 3.17. The correlation for the upper troposphere is similar to the one for the midtroposphere (not shown). As expected, the *w* variance in the boundary layer is about double that in the troposphere, and depends strongly on rainfall.

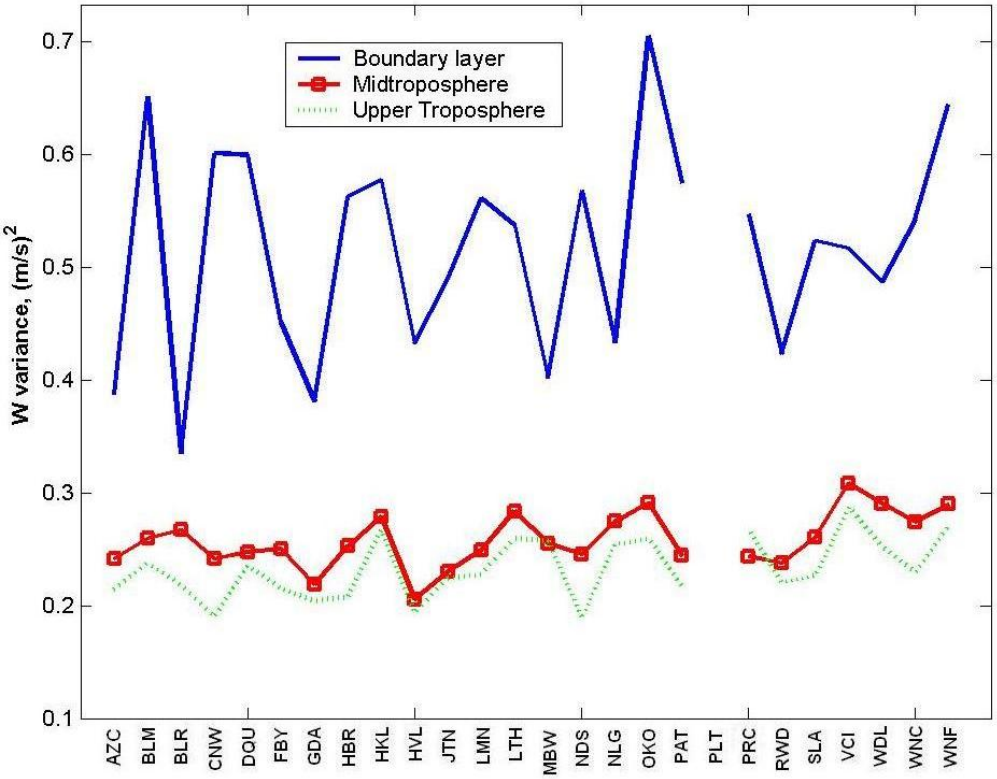

Figure 3.16. 36-month average variance of the vertical wind for boundary layer, mid-troposphere, and upper troposphere for 25 profiler stations.

The highest variance is observed at OKO, BLM and WNF (0.6 - 0.7 m^2/s^2), at the locations with highest rainfall rate of all sites.

Surprisingly, the correlation coefficient is slightly higher for the midtroposphere (0.3-0.7) than for the boundary layer (0.2-0.6) for most of the stations with medium and high rainfall. It reaches maximum values of 0.6-0.7 for DQU, GDA, HBR, and HVL.

These are the stations in close proximity, located in the southern central plains (as shown in fig. 2.3). Correlation is low or negative for stations at the very north and south of the spatial domain, or with lower than average rainfall. Low correlation coefficient for WNF, OKO, PAT in the boundary layer seems to be connected to reanalysis rainfall performance at small spatial scales, for a specific location (southern central), as correlation based on raingauge is significantly higher.

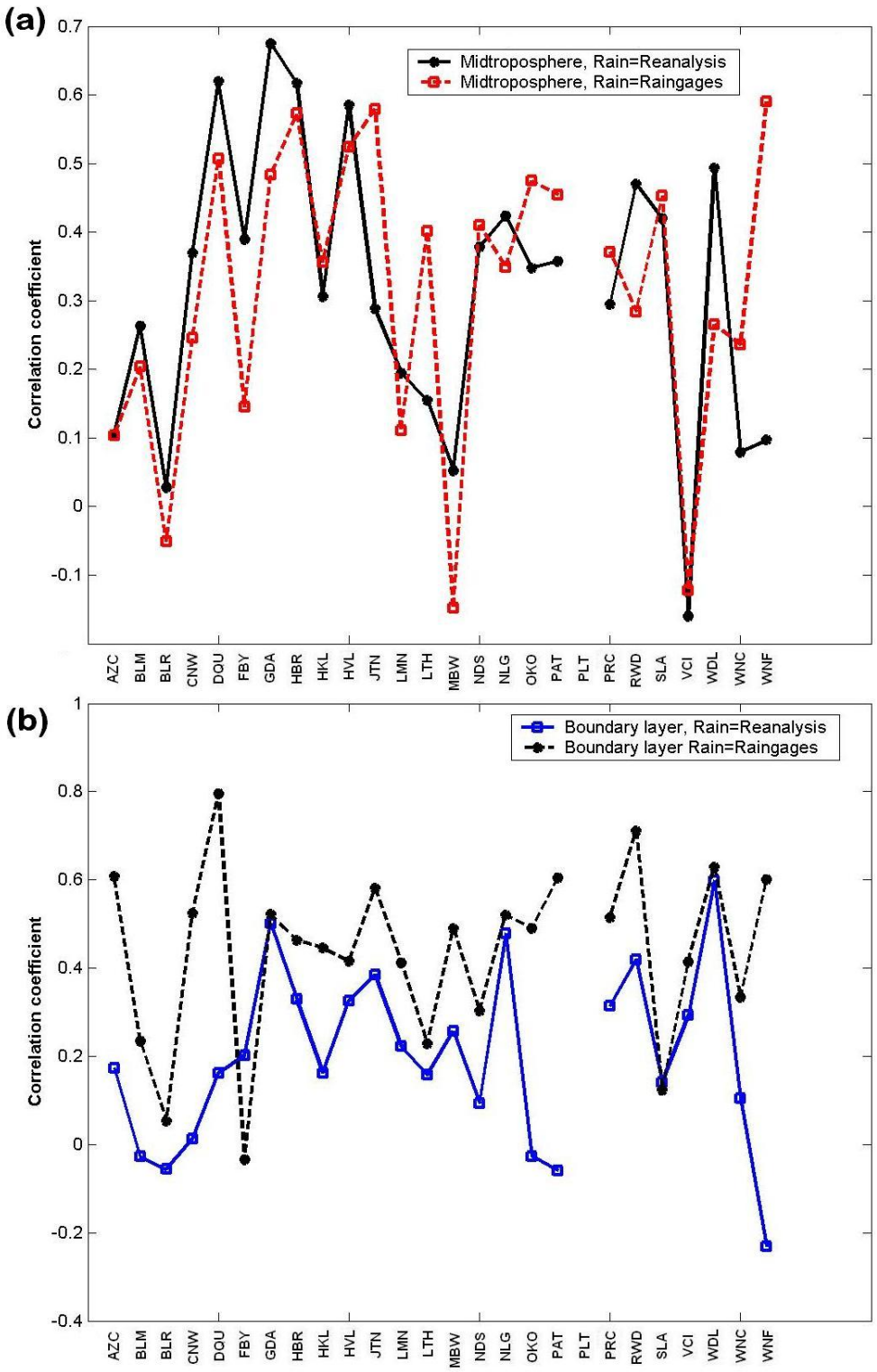

Figure 3.17. Correlation coefficient for vertical wind variance and rainfall rate for (a) the midtroposphere and (b) the lower troposphere for 25 wind profiler sites.

Another interesting feature is that correlations in the midtroposphere are higher for reanalysis rainfall data than for raingauges. The opposite is true for boundary layer. Based on the analysis of the plots above, we can speculate that raingauge data give better representation of the precipitation in the boundary layer, while reanalysis precipitation seem to be more consistent with precipitation signatures aloft. Hydrometeors originating in the upper troposphere might evaporate without reaching the ground and being detected by raingauges, but still would affect the vertical wind observed by UHF profilers.

In this chapter, we have pointed out the most prominent seasonal and altitudinal features of the long-term winds, measured by the NPN profilers. The performance of the horizontal wind measurements was expected and found to be good, on a monthly time scales, in comparison to reanalysis. The derivatives of the wind fields obtained (wind shear, distributions of wind directions and velocities) will be used in the following sections. The structure and behavior of the vertical winds was found to be much more complicated and therefore more challenging to explain. The main differences with previously reported vertical wind profiles are confined to the lowermost 1-4 km of the troposphere. The influence of precipitation on the vertical wind measurements will be further investigated in the next chapter. Using the reanalysis and model data we will try to develop a better understanding of the factors affecting vertical wind measurements by UHF wind profilers.

CHAPTER 4

COMPARISON OF PROFILER VERTICAL WIND WITH REANALYSIS ON LONG AND WITH MM5 MODEL DATA ON SHORT TIME SCALES

4.1 Comparison with NCAR/NCEP reanalysis vertical wind

In order to compare reanalysis and profiler-derived winds we have chosen to compare data at 500mb, level with close to zero divergence and therefore maximum synoptic-scale vertical winds in a barotropic atmosphere (Holton, 2004). This level corresponds to approximately 5500 m (Standard Atmosphere, 1976). The monthly averages of omega (vertical wind in pressure coordinates)) NCAR/NCEP reanalysis data at 500mb were obtained from the Climate Diagnostic Center Interactive plotting and analysis pages at *http://www.cdc.noaa.gov/cgi-bin/Composites/printpage.pl*. The vertical velocity ω from pressure-coordinates was converted into w (velocity in height coordinates) using the approximate relationship, which is valid for hydrostatic atmosphere on synoptic scales:

$$\omega \approx -\rho g w, \tag{4.1}$$

where ρ - density, g - gravity acceleration. The density data are not critical in this conversion, so they were obtained from Standard Atmosphere tables (U.S. Standard atmosphere, 1976). In figure 4.1 the profiler-measured vertical wind is compared to reanalysis vertical wind for the 36-month period, at the location of the JTN wind profiler. In order to facilitate the comparison, a reanalysis precipitation rate is shown, too. A similar plot, but for the WNF profiler, is shown in figure 4.2.

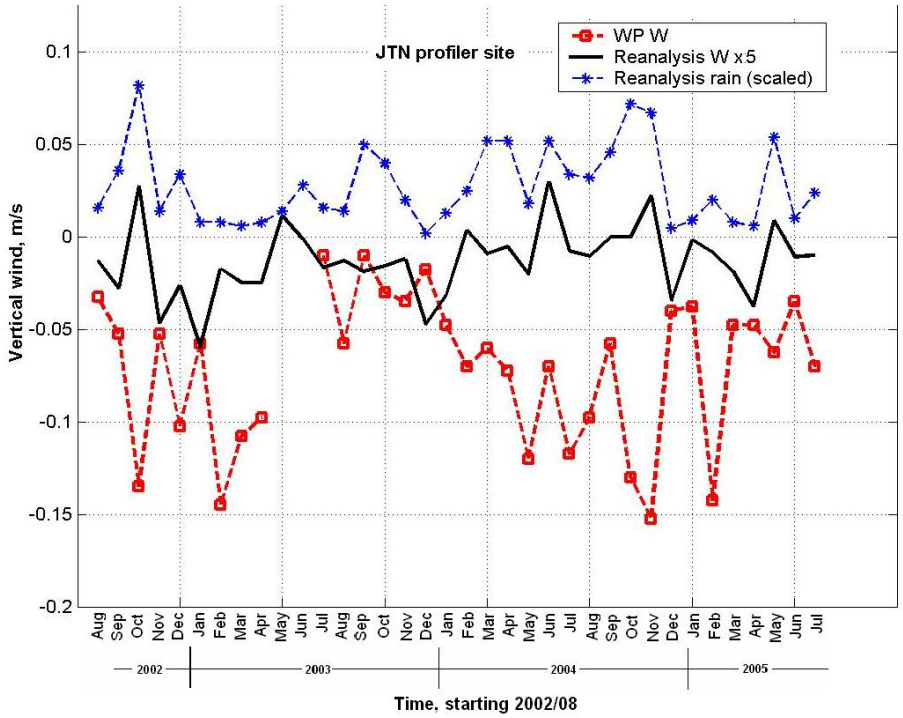

Figure 4.1. Comparison of reanalysis vertical wind and precipitation rate vs. profiler vertical wind for the JTN site at the 500 mb level. Note that reanalysis w is exaggerated 5 times, and reanalysis rainfall rate is scaled by 0.02.

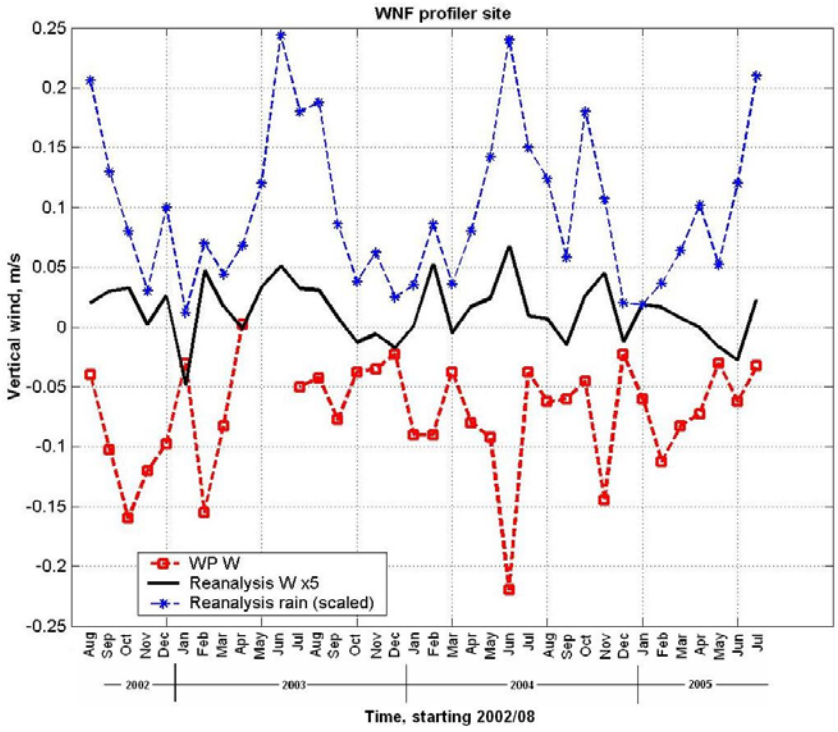

Figure 4.2. Same as above, but for the WNF site.

These sites were chosen to represent the locations with relatively high (WNF) and low (JTN) average precipitation rates. From the analysis of figures 4.1 and 4.2 the following observations can be made:

- The reanalysis-derived vertical velocities (order of ~1 cm/s) are significantly smaller than the profiler-observed values, the latter being mostly negative (-5…-10 cm/s on average);
- For the WNF site (characteristic of high-rainfall sites) the periods with positive reanalysis velocities correspond to increased rainfall and to large negative values of profiler-observed vertical motions, probably due to precipitation contamination.
- For the JTN site (characteristic of low-rainfall rate sites) the correlation of positive reanalysis velocities versus increased rainfall is not that prominent; similarly, the correspondence of increased rainfall periods and large negative profiler-observed vertical motions is less obvious than in the high-precipitation case. Despite ~3 times lower average rainfall rates, the negative shift of vertical velocities measured by the JTN wind profiler is similar to one for the WNF.

In general, the correlation between profiler vertical wind and reanalysis vertical wind is strongly negative with values -0.6…-0.7 for all the locations with high rainfall rates, and low negative for low-rainfall sites, as shown in figure 4.3. While the low correlation of -0.16 for the AZC is understood, as this is a location with very small rainfall, the reason for similarly small values for stations HBR, LTH and RWD is unclear, as those locations have close to average rainfall rates.

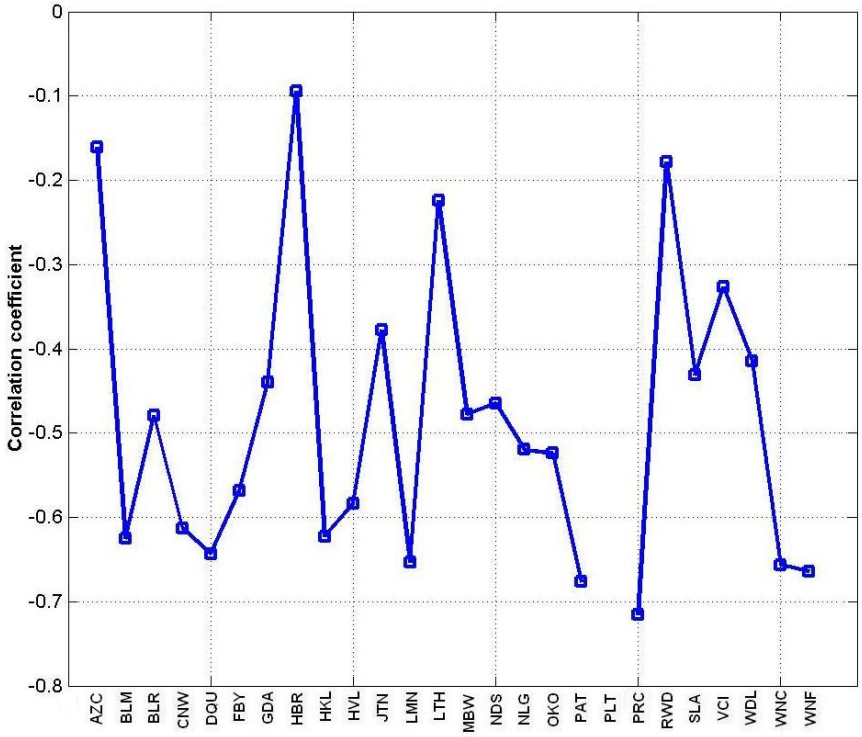

Figure 4.3. Correlation coefficient between reanalysis *w* and profiler-measured *w* at 500 mb for 25 profiler sites.

In order to better understand the effect of rainfall, we have grouped the profiler sites according to their corresponding average rainfall rates, and calculated the average correlation from figure 4.3 within the groups. The results are presented in table 4.1. The correlation is significantly larger for high-rainfall sites, than for low rainfall ones. Note, that the groups of high-rainfall sites coincide for both reanalysis and raingauge, while low-rainfall groups are overlapping.

It is obvious from the above analysis that the long-term averages of wind profiler vertical velocities in the midtroposphere are strongly affected by precipitation either directly or through enhanced gravity wave activity related to increased convection. The synoptic-scale vertical velocities, being significantly smaller in magnitude than rain-induced negative bias, are completely masked.

Table 4.1 Average correlation coefficients between vertical velocity measured by wind profilers and reanalysis vertical velocity at 500 mb. The list of sites and averages obtained for raingauge-defined low rainfall locations are given in brackets.

Locations	Average correlation coefficient
All locations, 26 sites	-0.49±0.18
High-rainfall locations BLM, DQU, OKO, PAT, WNF	-0.63±0.06
Low-rainfall locations AZC, HVL, JTN, MBW, VCI (AZC, GDA, MBW, RWD, WDL)	-0.39±0.16 (-0.33±0.15)

In order to extract the synoptic-scale vertical velocities, related to clear air rather than to precipitation, from UHF profiler data, some technique is needed for the removal or correction of rain-affected measurements.

4.2 Comparison with MM5 model data

For the comparison of profiler vertical wind with contemporary model data we have used the output of MM5 model runs for 09^{th}-23^{rd} of March 2003 (Data were provided by Yuhang Wang and Tao Zeng). The MM5 is a limited area, non-hydrostatic mesoscale model with terrain-following sigma-coordinates. The model run was performed with 23 sigma levels, grid resolution of 60 km at center and 1 hour time step output for winds. NCEP/NCAR reanalysis data were used as initial and boundary conditions. The model grid domain and the locations of the wind profiler sites are shown in figure 4.4.

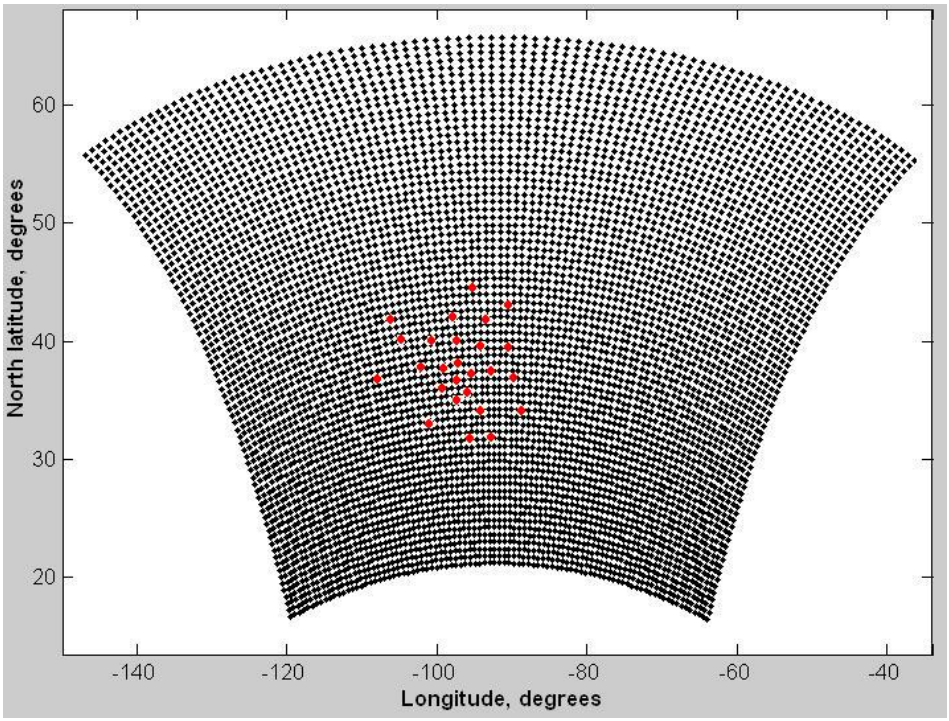

Figure 4.4. The grid (black dots) of the MM5 model domain used for this study and the wind profiler locations (red dots).

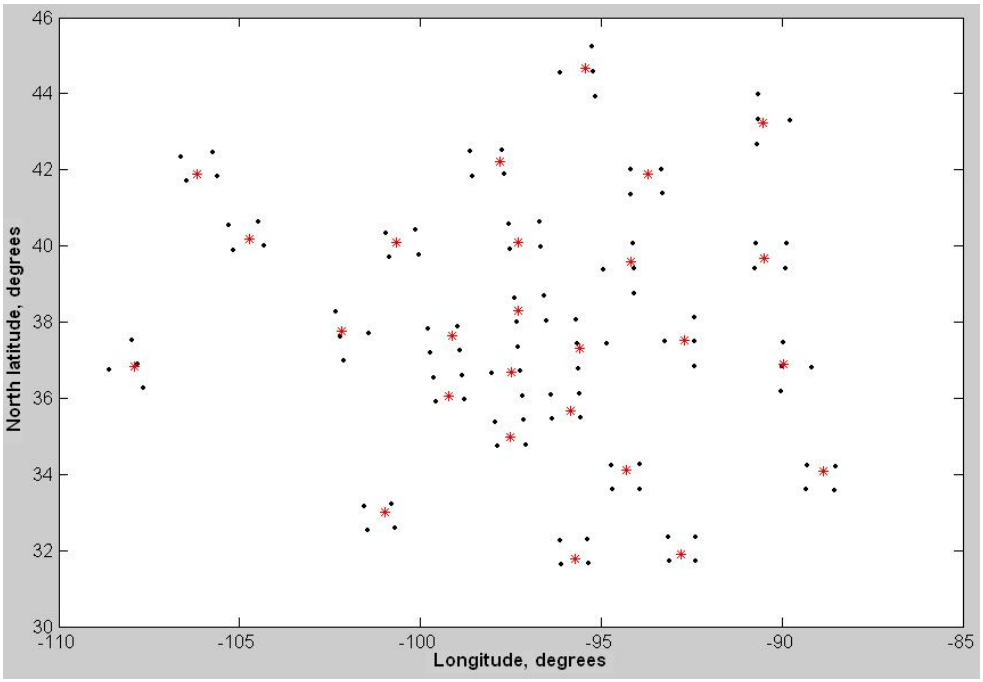

Figure 4.5. The sets of 4 gridpoints (black dots) closest to the location of the wind profiler sites (red stars).

The model domain covers the area of 20°- 60°N, 30°-140°W. Profiler sites are located near the center of the domain, where model resolution is the highest. Because the location of the model gridpoints does not correspond to the profiler site coordinates, and altitude levels are different from profiler sounding altitudes, an interpolation technique was used, as shown in figure 4.5 and described below:

- For each profiler location the closest 4 grid points were identified;
- The value of sought-for model output parameter for the location of the profiler is constructed as weighted average of the value for these 4 grid points, at the altitudes of the model sigma-levels;
- The values for needed altitude levels were linearly approximated using altitudes for sigma levels.

The weight coefficients for each gridpoint were chosen to be inversely proportional to the distance from the profiler site to that gridpoint, i.e. the closest gridpoint would have the largest weight.

Straightforward comparison.

The time-altitude plots of vertical velocity for profiler measurements and corresponding model output for the whole comparison period (09th-23rd of March 2003, 384 hours total) are presented in figure 4.6. The HKL site is shown; the plots for the other sites are similar (not shown). In general the amplitudes of profiler velocity are significantly larger than model output. Large-scale features, that are visible in model data, are not as obvious in profiler data as they are masked by strong variability, but still discernable during the first half of the observational period: large-scale ascending motion at 50-100 hours, followed by mostly descending motion at 100-150 hours.

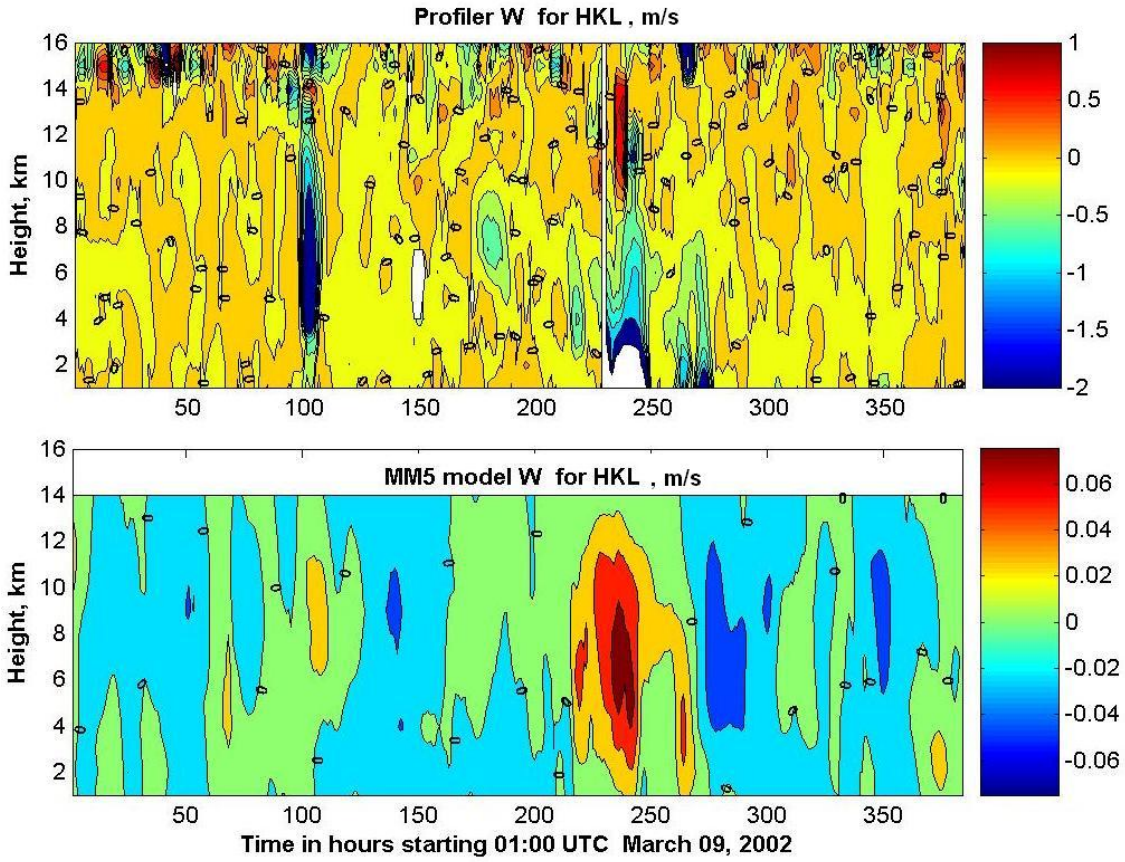

Figure 4.6. The Time-altitude field of the vertical velocities for March 9-24th, 2003 for the HKL wind profiler and the MM5 model.

The common feature of these comparison plots is the presence of strong downward motion in the profiler measurements at times that coincide with positive vertical wind predicted by the model. Positive model *w* correspond to the frontal-scale precipitation events, organized by synoptic disturbance, so it's obvious that profiler *w* at these times was contaminated by precipitation. For example, the positive *w* area in model data at ~100 hours corresponds to a cold front with squall line that passed above the profiler, and the strong ascending area at ~220 - 250 hours corresponds to a complex system of stationary and occluded fronts that was slowly moving northward above the site. Negative vertical velocities during the latter event have reached -1.5 m/s for a

prolonged period of time. Above the rain-contaminated area in the profiler data, the narrow area of strong positive velocities is visible at 8-14 km that corresponds well to model-predicted ascent at altitudes up to 12 km at ~240 hours.

Using the data for 363 hours, a correlation coefficient between hourly profiler and model vertical velocity was calculated separately for 3 altitudes: boundary layer (1 km), midtroposphere (5 km) and upper troposphere (9 km), for 25 profilers, as shown on figure 4.7. The correlation for most of the locations is similar for midtroposphere and the boundary layer, being negative with average value of -0.45, exceeding -0.7 for HVL and LMN. Stations JTN and SLA demonstrate significantly different behavior (correlation coefficients close to zero) than the rest of the stations.

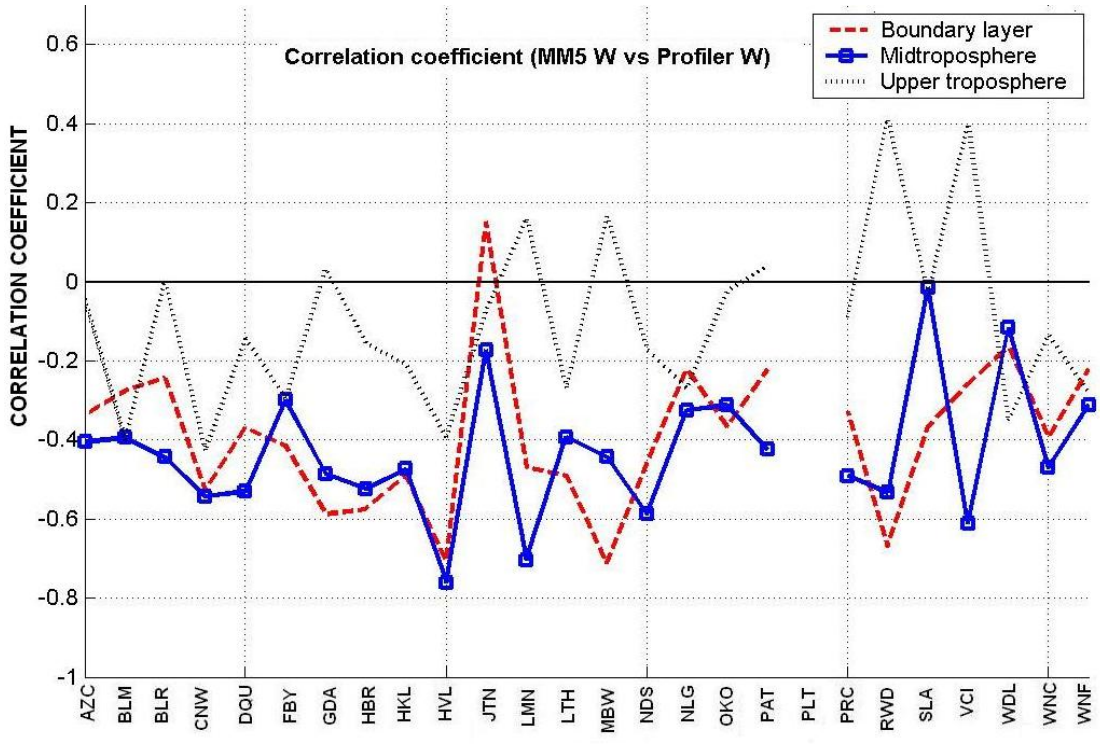

Figure 4.7. Correlation coefficient between the MM5 model and profiler vertical velocities for the lower, middle and upper troposphere, for 25 profilers.

The negative correlation (strong for HVL and LMN) is not surprising, as it is explained well by the observed rain contamination pattern: positive model velocities are consistent with precipitation events, which in turn results in negative raindrop-induced velocities seen by profiler.

Upper tropospheric vertical winds seems to be uncorrelated between profiler and model, which can be explained by their lower magnitudes, possible effects of strong upper tropospheric winds on profiler's measurements and generally lower signal-to-noise ratio affecting radar performance at upper limit of it's operational altitudes.

In the following section, we will discuss the characteristics of rain-affected data, propose a simple rain-correction procedure and discuss the results of this correction applied to the NPN profiler dataset used in this study, by comparing the corrected data to reanalysis and MM5 model vertical winds.

4.3 Procedures and thresholds for the correction of precipitation-affected vertical velocities. Comparison of the corrected profiler data to reanalysis and MM5 vertical wind data

In order to develop the procedures for correcting the rain-contaminated data, we will examine the wind profiler measurements presented above, and determine the criteria, that would allow detection and correction of precipitation-contaminated data. In the context of this study we will define the precipitation particles (as opposed to regular cloud particles) as droplets or ice crystals that possess fall velocities significantly exceeding the velocities of the typical air motions. Following Ralph et al., (1995a) we

will assume that these "significant" velocities correspond to the water droplets with radius >25 μm, or ice crystals with radius >100 μm. The hydrometeors of these sizes have a fall velocities of ~ 10 cm/s (Ralph et al., 1995a) that is still comparable to air velocities outside of strong convective events and gravity waves. The precipitation identification problem therefore is linked to the question: what is the fall velocity of the precipitating particles at which their reflectivity would exceed the one from clear air, and therefore the profiler radar signal spectra processing system would erroneously attribute precipitation fall velocities to clear air velocities.

The first and the best criterion to separate the clear air data from precipitation data would probably be the received power of the signal, as it is significantly enhanced by precipitation. The Raleigh scattering from raindrops (described by equation 2.4 in chapter 2) is stronger than Bragg scattering from clear air (equations 2.2 and 2.3) when the radar reflectivity factor Z in the precipitation exceeds 0 - 15 dBZ (Ralph, 1995b). Unfortunately, the data reported by NPN profilers and archived do not contain reflectivity values and the transmitting/receiving system is not calibrated for reflectivity measurements. Therefore the only available source of information for precipitation identification is a vertical velocity measured by the profiler itself.

The long-term distribution of velocities measured by the wind profilers discussed in section 3.2 might give a valuable insight into this issue, particularly - the skewness of the distribution. In order to assess this skewness, we have subtracted the positive half of the distribution from the negative one, with typical results shown in figure 4.8. The upper curve on each graph corresponds to the negative velocities, and the lower curve – to positive velocities.

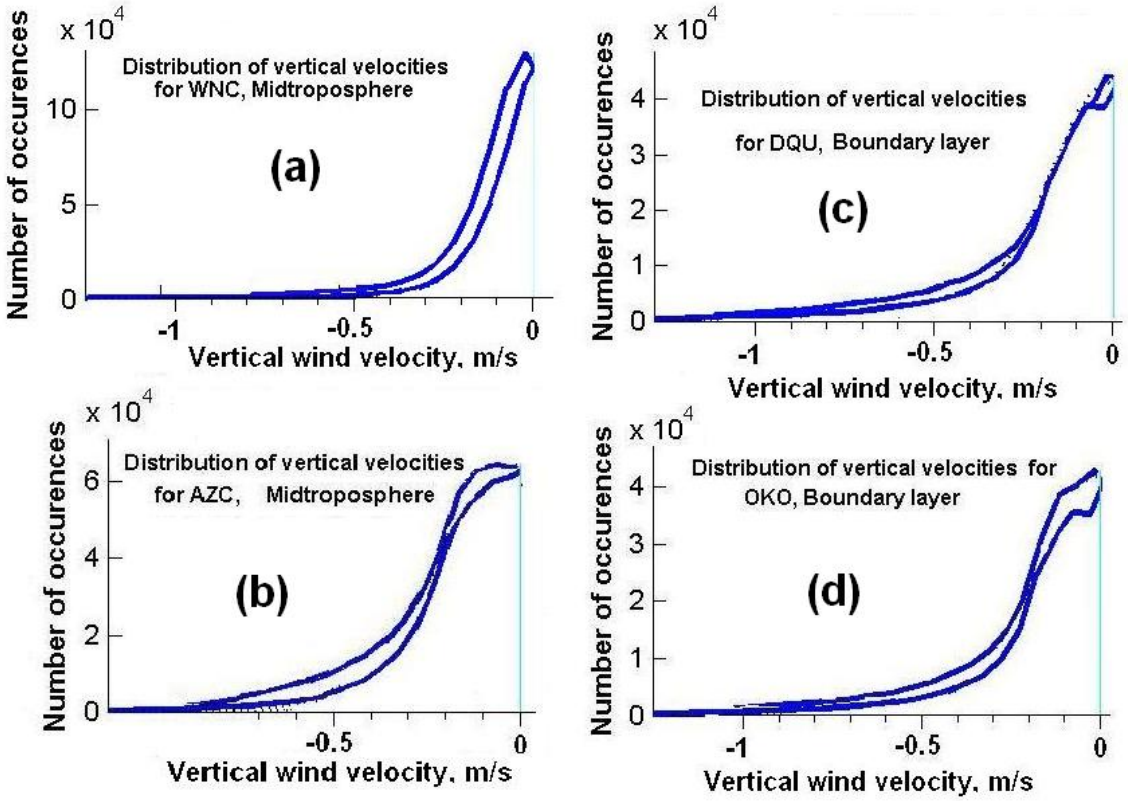

Figure 4.8. Difference between the positive and negative parts of the velocity distributions for the midtroposphere - (a) WNC, (b) AZC; for the boundary layer - (c) DQU and (d) OKO.

The difference between curves can be attributed to both the precipitation and gravity wave effects. It is known from publications (Nastrom and VanZandt, 1994; Nastrom and VanZandt, 1996) that the gravity waves introduce the negative bias in vertical wind measurements by profilers. The wave-induced motion of the air parcels modifies the reflectivity of the parcel (downward moving parcels have higher static stability and hence, reflectivity, than upward-moving ones) thus biasing the measurements toward negative values. The mean magnitude of this bias has been estimated as ~5 cm/s (same reference) with an uncertainty factor of 2.

The gravity wave bias appears in the upper part of the plots (b) - (d) in figure 4.8, and corresponds to velocities about 0…-0.2 m/s (area of the difference between curves at

close to zero velocities). The maximum value of the bias (difference between curves) is observed at about 10 cm/s and decreases at higher and lower velocities, that correspond well with the findings of Nastrom and VanZandt. In the hypothetical case, when the gravity waves would not bias the vertical wind measurements, the positive and negative parts of the distribution would be symmetrical and the curves would coincide within the velocity range corresponding to typical gravity wave bias.

It is reasonable to assume then, that the differences in the lower part of the curves, that extends from about -0.25 m/s to larger negative values can be attributed to precipitation, as these velocities are significantly larger than bias due to gravity waves. The plot (a) in figure 4.8 represents the case when two areas, corresponding to gravity wave and precipitation effects, are smoothly blended into each other. This might be due to a larger fraction of small precipitation velocities present, in the form of snow and ice crystals with low fall velocities. A similar distribution was found at WDL – the most northerly located site, where one would expect to observe a larger fraction of the precipitation to be in the form of snow (low fall velocities), at least at high altitudes.

Another possible way to determine the precipitation effects is to look at the scatter plots of the MM5 model vertical velocities and profiler-measured velocities. The typical plot for the HBR profiler location is presented in figure 4.9. In this figure, the values of MM5 vertical velocities are on the x-axis, while corresponding profiler velocities are plotted on the y-axis. Each dot represents a one hourly-averaged velocity data point.

While most of the points are concentrated in the center, there is a distinct cluster of points in the lower part of the plot that corresponds to positive MM5 model velocities, and negative profiler velocities. Positive model velocities denote rising air motion and,

likely, resulting in precipitation. Note that larger positive MM5 velocities correspond to larger negative values of profiler wind. This cluster of profiler vertical wind data points is most likely precipitation-contaminated. From the plot, the velocities corresponding to precipitation-affected data start at ~0.25 m/s. For comparison, a subset of this data for non-precipitation conditions is shown in figure 4.10.

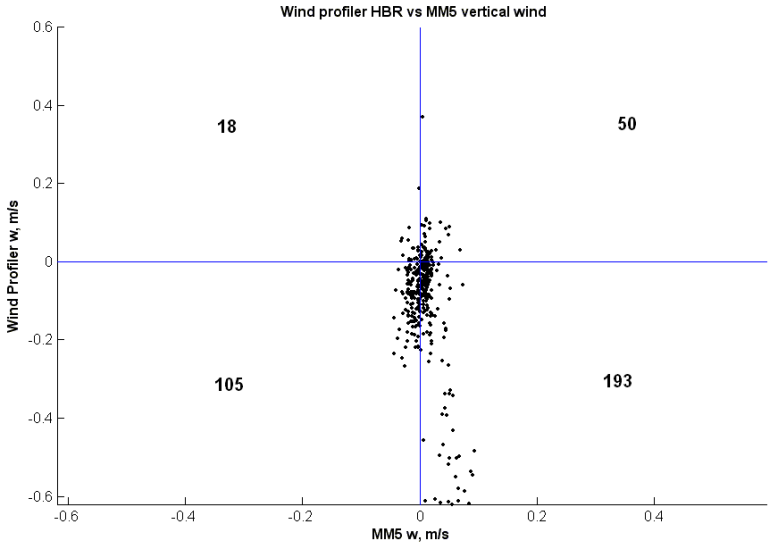

Figure 4.9. Scatterplot of the MM5 versus the HBR profiler vertical velocities. The number of points in each quadrant is shown at the middle.

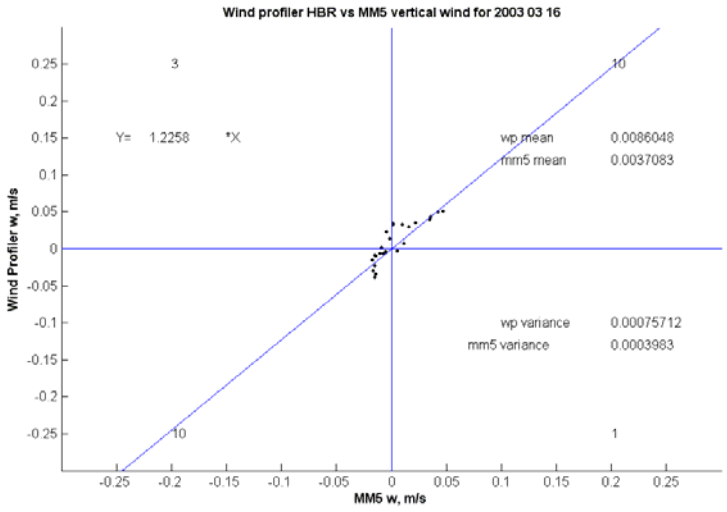

Figure 4.10. Same as above figure, but based on the data subset for a non-precipitation period (16/03/2003).

The results of the above comparison are similar to the values obtained above using wind velocity distributions, and correlate well with the threshold values obtained by Ralph et al. (1996), who compared the profiler-measured vertical velocities and range-corrected radar signal power (not available in this study). The threshold estimates of Ralph et al. ranged from 0.28 m/s to 0.39 m/s, and were found to have only 5.7% probability of incorrect identification of air motions as precipitation fall velocities.

Comparison of corrected profiler vertical winds to reanalysis data.

Based on the threshold values determined above, the original 6-minute resolution NPN dataset was edited and rain-contaminated data corrected. Three thresholds were used: -0.25 m/s, -0.35 m/s, and -0.45 m/s. We have chosen to use three thresholds because only the lower range of the threshold values obtained by Ralph et al. coincides with our findings, and it is of interest to roughly estimate the sensitivity of the rain removal procedures to the values of thresholds.

The rain-removed vertical velocity data from NPN were then compared to NCAR/NCEP reanalysis monthly mean vertical velocities using the same approach, as before, in section 4.1. The correlation coefficients between rain-removed profiler vertical wind and reanalysis vertical wind for 25 profiler sites are presented in figure 4.11.

To facilitate the comparison, the original (non-rain-corrected) correlation coefficients are shown on the same plot, too. As the result of correction, for all locations the correlation coefficients have increased; for the most of the sites they become weak positive, and have reached ~0.55 for 2 stations, RWD and SLA.

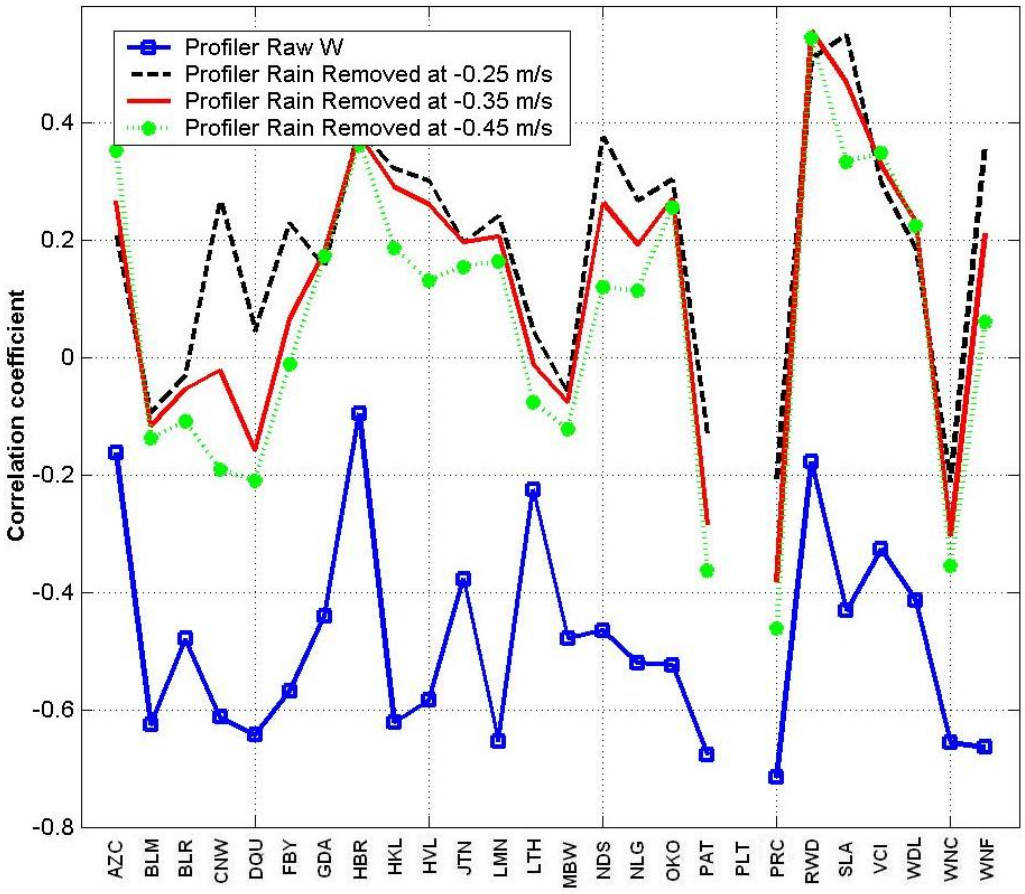

Figure 4.11. Correlation coefficient between monthly mean reanalysis *w* and profiler rain-corrected *w* at 500 mb for 25 profiler sites.

From the figure 4.11 we see that the correlation coefficients are robust with respect to rain-removal threshold, with slightly better correlation achieved based on a -0.25 m/s threshold. The fact that correlation coefficients have not reached high positive values is indicative of incomplete correction of the rain bias, presence of some other factors affecting profiler's vertical wind measurements, or possible errors in reanalysis data.

Comparison of corrected profiler vertical winds to MM5 model data.

The rain correction was applied to the 6-minute resolution profiler data used for comparison with the MM5 model. As with the comparison in section 4.2, correlation

coefficients between MM5 model and profiler vertical winds for the 36-month period were obtained for 25 sites, as shown in figure 4.12. Comparison with figure 4.7 for non-corrected velocities leads to the following conclusions:

- The performance of the wind profilers in the midtroposphere when compared to the MM5 model is increased significantly by the rain-correction procedures. Correlation coefficients have reached 0.65 for HBR, ~0.4 for a number of stations, with an average value of 0.24.
- The performance of the wind profilers in the upper troposphere have not changed significantly. It's logical to assume, that the reason for the discrepancies at the higher altitudes is not connected to precipitation. Our data seem to support the suggestion of Worthington et al., (2001) that the gravity waves and mountain waves are responsible for vertical wind biases in the upper troposphere.
- As with the upper troposphere, the correlation varies in the boundary layer, with the average close to zero. This is an unexpected result, as one would anticipate the maximum of precipitation influence to take place in the lower troposphere.

It's not clear whether the performance of the model could be the reason for this discrepancy (due to the pure representation of the topography and therefore vertical motions on small scales), or a random episodic behavior of the convective events, that can not be represented adequately in the model. This issue requires additional attention and probably can be resolved if a high-resolution regional model was used for comparison. Longer datasets and more statistical approach based on multiple model runs with slightly adjusted boundary conditions and initialization data would be the most suitable way of addressing this problem.

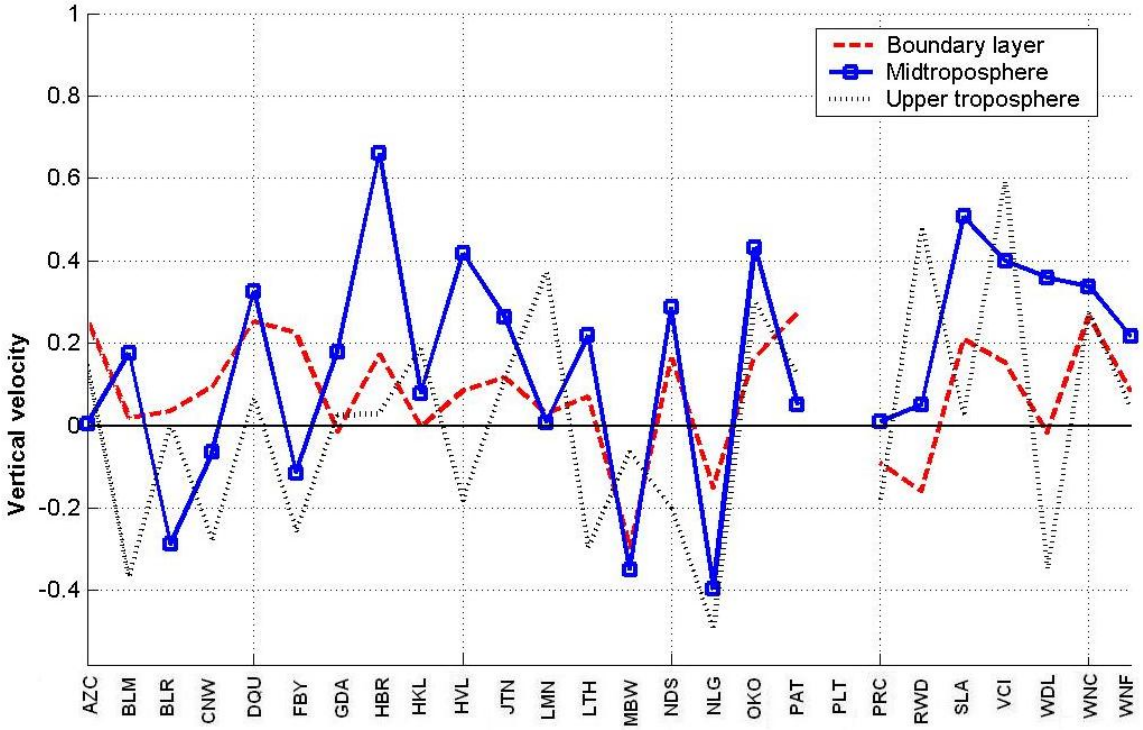

Figure 4.12. Correlation coefficient between profiler and model vertical velocity in the lower, middle and upper troposphere for 25 profiler sites. Profiler data have rain correction at -0.25 m/s. Correlations are based on 363 hourly data points.

In the midtroposphere, the rain-corrected and additionally smoothed profiler vertical velocities show good agreement with the MM5 model vertical velocity for 8 locations and is especially noticeable for DQU, FBY, HBR and NDS. The time realizations of vertical winds for DQU and SLA at 5 km are shown in figure 4.13, for the whole duration of the comparison period (16 days). The first and last 11 hours of profiler data shown in the plot are distorted due to the smoothing window algorithm. On the shorter time scales, the correlations were found to be significant and positive in some data subsets; up to 0.7 - 0.8 (e.g. figure 4.14, showing the selected 6-day period for DQU with a correlation coefficient of 0.78). At the same time for some periods the observed correlation was large and negative (e.g. on March 14 for the HBR profiler the correlation coefficient was -0.7, not shown).

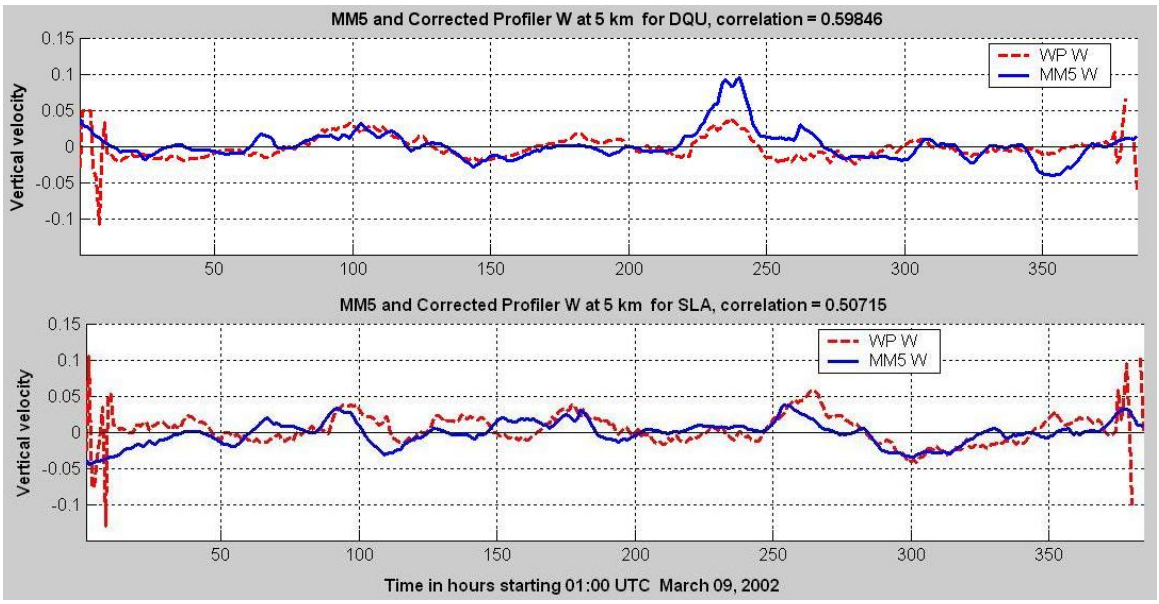

Figure 4.13. Comparison of vertical velocity for the whole period at midtroposphere for the SLA (lower plot) and the DQU (upper plot) profilers.

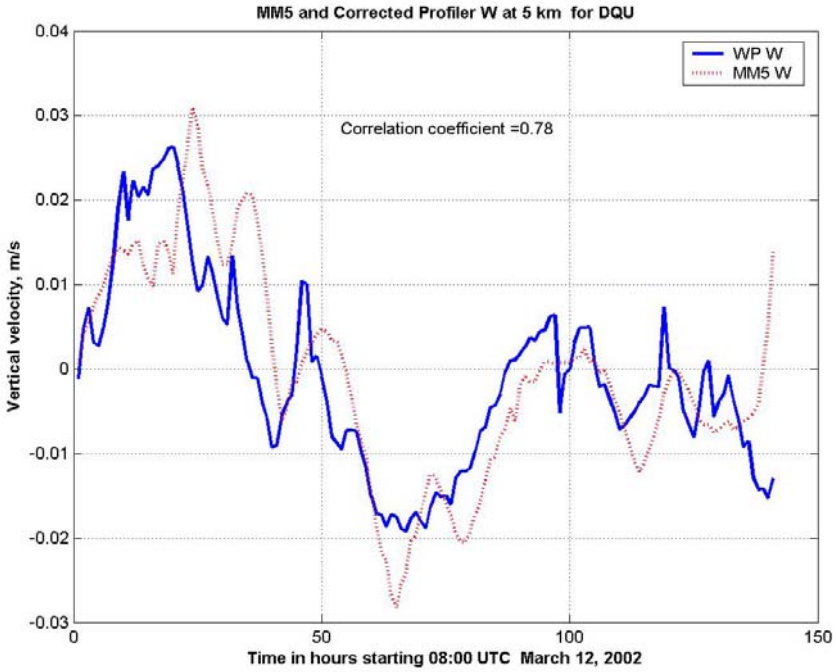

Figure 4.14. DQU profiler and MM5 model vertical velocities at 5 km. Profiler data have rain correction at -0.25 m/s and are smoothed with a 21-hour window.

The analysis of the vertical winds measured by the wind profilers have shown that for the NOAA profiler network sensitivity to rain is a more significant problem than for VHF radars, especially at ~1 to 3 km altitudes. The results of the precipitation correction, applied to the wind profilers' vertical wind showed significant improvement in the agreement between the model (and reanalysis), but at the same time gave an indication that other factors might be the same as, or even more important than, precipitation in biasing the vertical wind measurements by wind profilers. These factors include gravity waves and topography. In the next two chapters we will focus on quantification of these factors. Then, we will return to the interpretation of the vertical wind measurements.

CHAPTER 5

GRAVITY WAVES AS SEEN BY THE NOAA PROFILER NETWORK

A detailed description of gravity wave theory is beyond the scope of this paper. The detailed theory can be found in many excellent monographs (e.g. Gossard and Hooke, 1975; Nappo, 2002; etc.). Instead of theoretical consideration, in this study we will be interested mostly in determining the parameters of the gravity waves "observable" by the wind profiling radars or affecting wind profiler measurements, among which the wave energy at different frequencies will receive the most consideration.

It is generally accepted (e.g. Nastrom et al., 1990a; Nastrom and VanZandt 1994b) that variance of the winds measured by wind profilers is an integral representation of gravity wave activity (of the corresponding component of gravity wave energy). An approach that uses the variance of the wind to obtain parameters of the gravity waves is somewhat limited, as no information about the frequencies of the waves can be obtained, and therefore no specifics of how gravity waves of certain frequencies are generated, can be inferred. In the following section we will discuss the temporal and spatial properties of the variance of the components and the total variance of the wind, but limit the use of these data to verification of the gravity wave climatology and parameters, that will be obtained later using spectral analysis. It is also of interest to compare the gravity wave energies obtained by Nastrom and VanZandt (1994b) and Wang and Geller, (2003) who used an approach similar to ours, but applied to the variance of vertical profiles of the

horizontal wind. Further in this chapter, more attention will be given to the results of the spectral analysis method, which we have used to obtain the gravity wave parameters for several frequency bands.

It is known that flow over rough terrain, convection and horizontal wind shear are possible sources of gravity waves (Nastrom at al., 1990; Hirota 1997; Fritts et al., 1984). The analysis of the possible sources of generation for different wave frequencies will be conducted in this chapter by obtaining correlations between the temporal changes of gravity wave energies and convective activity (using rainfall rates as a proxy for convection) and horizontal wind shear. The topographic effects on gravity wave generation will be considered in chapter 6.

5.1 Profiler-derived wind variance data

The variance of the hourly mean values of the three orthogonal components of the wind σ^2_u , σ^2_v and σ^2_w was obtained using the algorithms described in chapter 2, similar to the wind variances presented in chapter 3. Three orthogonal components of the variance were obtained for each month of the 36-month study period for 25 profiler sites. Using the σ^2_u , σ^2_v and σ^2_w , the total 3-D wind variance was then obtained as the sum of the variance components:

$$\sigma^2_{total} = \frac{1}{2}(\sigma_u^{\,2} + \sigma_v^{\,2} + \sigma_w^{\,2}) , \qquad (5.1)$$

as was done by Wang and Geller (2003) in the altitude domain. The factor of 1/2 was introduced to convert the wind variance into gravity wave energies, and for consistency

with Wang and Geller's calculations. The time-altitude fields of the profiler-measured monthly-averaged σ^2_{total} are presented in APPENDIX E. Sample plots are presented in figure 5.1 for the AZC, WNF and MBW wind profilers.

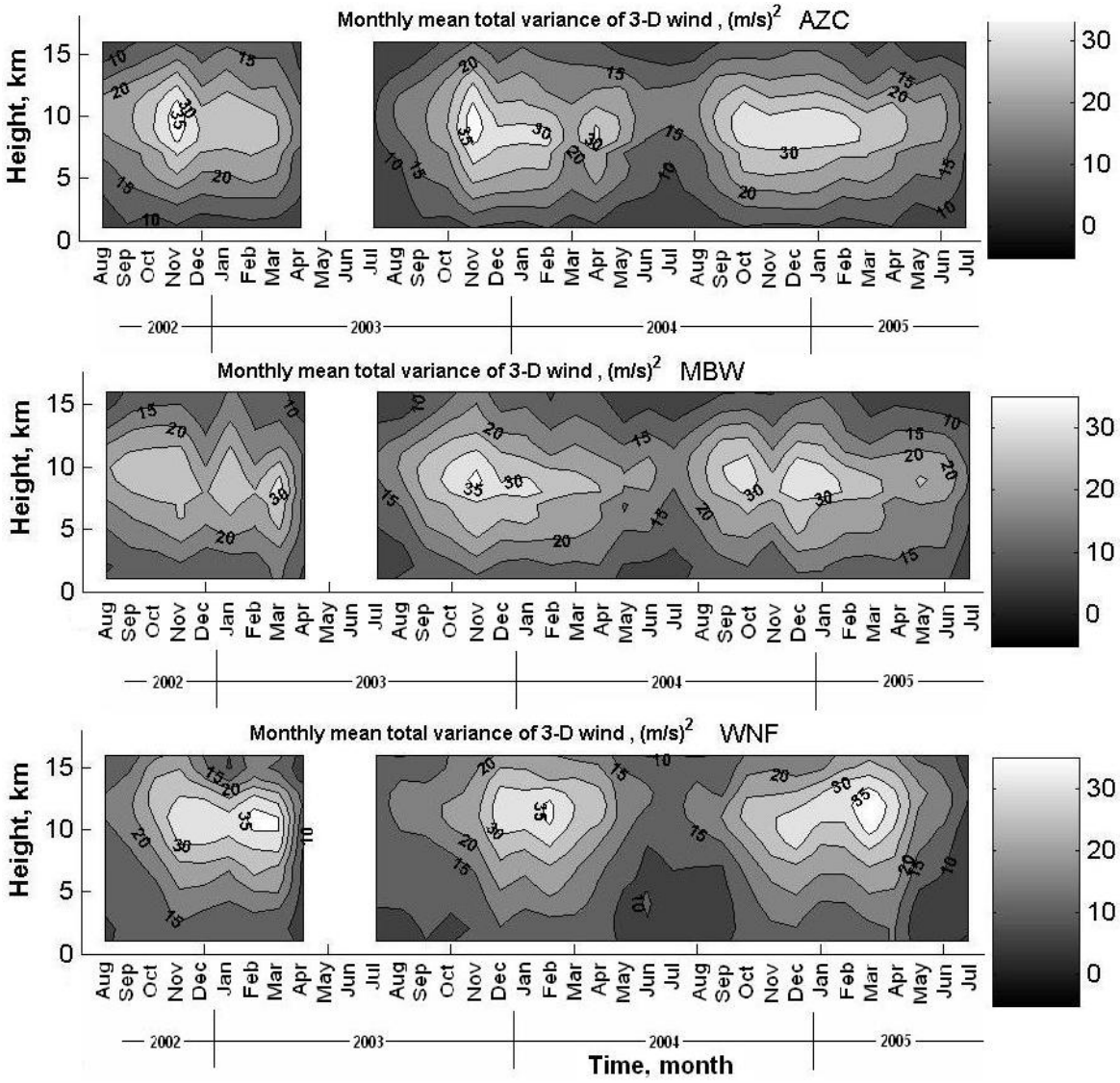

Figure 5.1 Time-altitude fields of monthly averaged total wind variance for the AZC (upper plot) WNF (lower plot) and MBW (middle plot) for the 36 month study period.

Analysis of the individual variances σ^2_u , σ^2_v and σ^2_w (not shown) and figure 5.1 have revealed the following features, common for most of the sites:

- σ^2_u and σ^2_v have a definite seasonal cycle, with maximum in late fall/winter, and minimum in summer.
- The amplitudes of the variance of the horizontal wind components σ^2_u and σ^2_v are similar, with summer minima of ~ 6 m^2/s^2 in midtroposphere and ~12 m^2/s^2 at the level of maximum winds. Winter maxima of the variance of the horizontal wind components are also similar, with values of ~20 m^2/s^2 for both components.
- The amplitudes of the vertical wind variance σ^2_w are significantly smaller, up to 1 m^2/s^2 in active periods, and typically as low as 0.1 - 0.2 m^2/s^2 during the other times. The time-altitude structure of σ^2_w is more complicated than for σ^2_u and σ^2_v , as shown in figure 5.2 for the WNF profiler. The vertical wind variance has several periods of enhancement in the lower troposphere, typically both in fall/winter and summer, with winter maximum often extending into the upper troposphere. High variance is also observed in the lower stratosphere. Rather than being a real atmospheric feature, this stratospheric maximum more likely is a result of the low signal-to-noise ratio at these heights.
- Total variance σ^2_{total} is very close in behavior to horizontal wind variance, and has a distinct seasonal variation, with maximum in fall/winter months (November-February) and minimum in summer;

- The altitude of the seasonal maximum is within 8-12 km for different locations, with northern sites having a maximum at lower altitudes (~8 km), and southern sites – at higher altitudes (11-12 km);
- The amplitudes of the maxima are about 30 - 35 m^2/s^2 (J/kg), and "low activity period" waves have energies of ~ 10 m^2/s^2 (J/kg);

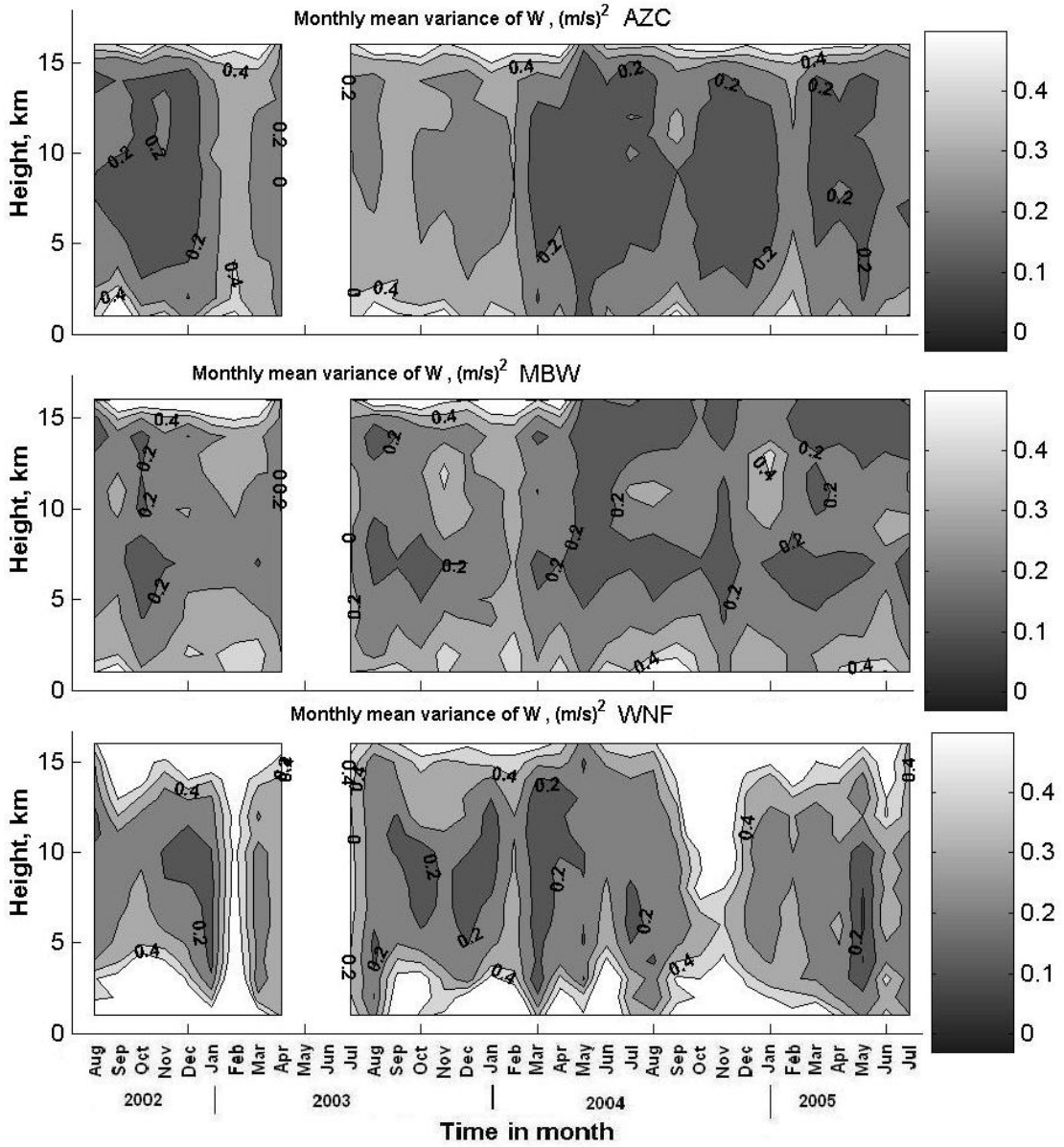

Figure 5.2. Same as fig 5.1, but for variance of the vertical wind.

The complex structure of the vertical wind variance is determined by the superposition of three possible sources generating vertical waves. These sources: convection, the jet stream and topography are located at different altitudes – topography at the ground, convection in the lower troposphere and the jet at upper troposphere. Comparison of fig. 5.1 (lower plot) and fig. 5.2 reveals that two vertically extended maxima (February 2002 and October-December 2004 in figure 5.2) coincide with maxima of horizontal wind variance at ~ 10 km, and seem to propagate upward and downward creating vertically-extended high-variance areas. Similar features were observed for the other profiler sites, too.

The variations of the horizontal wind seem to be the dominant source explaining the variability of the total variance, as could be seen from comparison of figures 3.1 and 3.2 and figure 5.1. Both seasonal changes and altitudes of maxima coincide extremely well for horizontal wind and wind shear form one side, and total variance from the other side. More detailed analysis of this dependence will be presented later.

5.2 Spectral analysis technique and implementation to profiler data

To obtain the gravity wave energy we have used an approach similar to one used by Hansen et al., (2001). Rather than using the lagged autocorrelation function to estimate the power spectra, as was done by Hansen et al., we have chosen to use the Fourier transform, which is a more straightforward technique. In order to implement spectral analysis, the data should be continuous, with no gaps. Filtered and quality-controlled time realizations of u, v and w data at each altitude were searched for

continuous segments with length from 6 to 12 hours. The choice of the period is determined by several factors. First, the gravity wave frequencies are confined within the Brunt-Vaisala and inertial frequencies, which for the latitudes considered in this study typically found to be ~ 5min. and ~21 hours respectively. Second, uninterrupted data with lengths of more than 12 hours (120 6-minute data points) are rare, which decreases the total amount of data used in calculations. Third, data segments shorter than 12 hours would capture less than a full period of an oscillation with 12-hour period, therefore lower frequencies will be missing from the spectral domain. And, finally, we wanted to minimize leakage of the energy from the synoptic-scale disturbances and Rossby waves into the gravity wave energy domain. With a 21-hour upper limit of data segment length, chosen by Hansen at al., this contamination may be significant.

The highest distinguishable frequency is determined by the Nyquist frequency and is 1/720 Hz (period of 12 minutes) for this case. During the search, if a gap in data was detected, and data segment length was less than 6 hours, the search would restart. If the segment is longer than 6 hours long, and the gap in data was encountered, the data segment was padded with zeroes to the length of 120 points, and Fourier analysis was performed. If the continuous data segment has reached 12 hours, the search was stopped, Fourier analysis was then performed and a new search started. The digital Fourier analysis of a data segment x(n), n=1 - N, N=120 was performed using the standard subroutine, yielding the complex spectral coefficients

$$X(k) = \sum_{n=1}^{N} \mathrm{x(n)} \cdot \exp\left[\frac{-\mathrm{j} \cdot 2\pi \cdot (\mathrm{k}-1) \cdot (\mathrm{n}-1)}{N}\right], \quad 1 \le \mathrm{k} \le \mathrm{N}. \tag{5.2}$$

The power spectra were then obtained as

$$S(k) = X(k) \cdot X^{*}(k), \tag{5.3}$$

where (*) denotes the complex conjugate. The resulting power spectra were then trimmed to remove a "mirror" half. At the next step, the power spectra from subsequent data segments at the same altitude were integrated within a month, to obtain monthly mean gravity wave energy at 1-km height resolution, and scaled in magnitude to provide unbiased estimates of "instantaneous" mean gravity waves energy in the corresponding wind component (*u*, *v* or *w*). In order to distinguish high- and low-frequency waves, the gravity wave energy was then divided into 3 frequency domains with periods of:

- 12 min - 1 hour (called high-frequency gravity waves);
- 1 hour - 3 hours (called mid-frequency gravity waves);
- 3 hours up to 12 hours (called low-frequency gravity waves).

The choice of the frequency bands for the gravity wave energy is somewhat different from the 6 min - 2 hour and 2 - 21 hour used by Hansen et al., (2001). We have used the division into 3 bands to facilitate analysis of frequency-specific generation sources. Following Hansen et al., (2001), the total gravity waves energy was obtained as sum of kinetic energy associated with vertical and horizontal components: $E_k = \frac{1}{2}(E_u + E_v + E_w)$, integrated for high-, mid- and low-frequencies. In the following section we present the results of the spectral analysis as applied to the profiler winds. The total gravity wave energy was used to establish climatology together with spatial plots describing variations of the gravity wave activity in the zonal and meridional directions. The *u, v* and *w* components of the total energy and gravity wave energies at high, medium and low frequencies were used to determine the wave sources.

5.3 Spatial and seasonal characteristics of the gravity waves over central USA derived using spectral analysis

The time-altitude plots of total gravity wave energy E_k for the AZC, MBW and WNF profiler locations are presented in figure 5.3 (the plots for the other locations are given in APPENDIX F). The plots shown are in units of J/kg, and represent monthly-averaged "instantaneous" total gravity wave energy observed above the specific location. The total gravity wave energy plots shown in figure 5.3 are similar in general features to

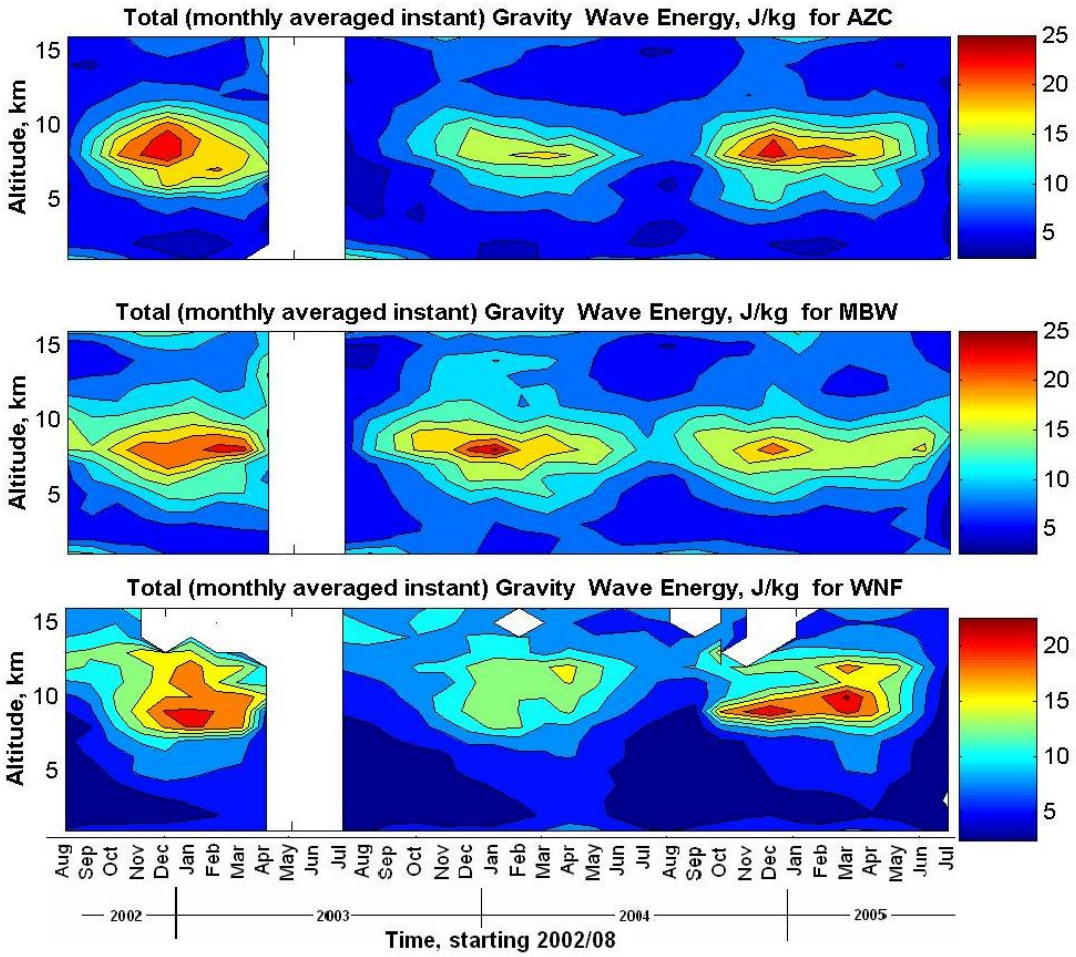

Figure 5.3. Time-altitude fields of total gravity wave energy E_k for the AZC (upper plot), MBW (middle plot) and WNF (lower plot) locations.

the plots for the other profiler sites. These features can be summarized as follows:

- Gravity wave energy has a pronounced seasonal cycle, with a maximum that typically extends from late fall to spring, and a minimum in July-September.
- The amplitudes of the total gravity wave energy maxima in winter reach 15 - 25 J/kg. Summer maximum values are within 8 - 15 J/kg. In the lower troposphere gravity wave energy values do not exceed 5 - 10 J/kg.
- The altitudinal level of maximum energy seems to fluctuate with season, being on average ~2 km higher in summer than in winter. The altitude of the winter maximum is within 9 - 11 km for different locations, and the altitude of the summer maximum of total energy is usually higher, at ~12 km.

Comparison of total wave energy with total wind variance (figure 5.1) shows very similar features, in both the altitude and time domains. Maximum values of the wave energy obtained from a 3-D wind variance σ^2_{total} are about 40 % higher (~35 J/kg vs. ~25 J/kg) than for gravity wave energy parameters obtained by spectral analysis. This difference is expected, as the variance represents energy in the all possible frequencies, including slow synoptic-scale changes with a timescales of weeks, while in spectral analysis we have limited ourselves with a 6 min - 12 hours spectral window. Also, uninterrupted data segments that are shorter than 6 hours were not used for spectral analysis, but contribute to variance calculations. Shorter data segments may be a result of data interruption with some extreme events, like thunderstorms, strong winds, etc., and therefore, variance would include these events while spectral analysis would not.

The structure of the total gravity wave energy field is mostly defined by the wave kinetic energy associated with horizontal components *u* and *v* (not shown) that are similar

in magnitude. Also, the total wave energy fields are very similar to the plots of the zonal wind and horizontal wind shear itself, as can be seen from comparison with figures 3.1-3.2. This suggests the importance of the jet-stream as a generation source for gravity waves.

Gravity wave energy associated with vertical component is significantly smaller than for the *u* or *v* components, and has a different structure, as shown in figure 5.4.

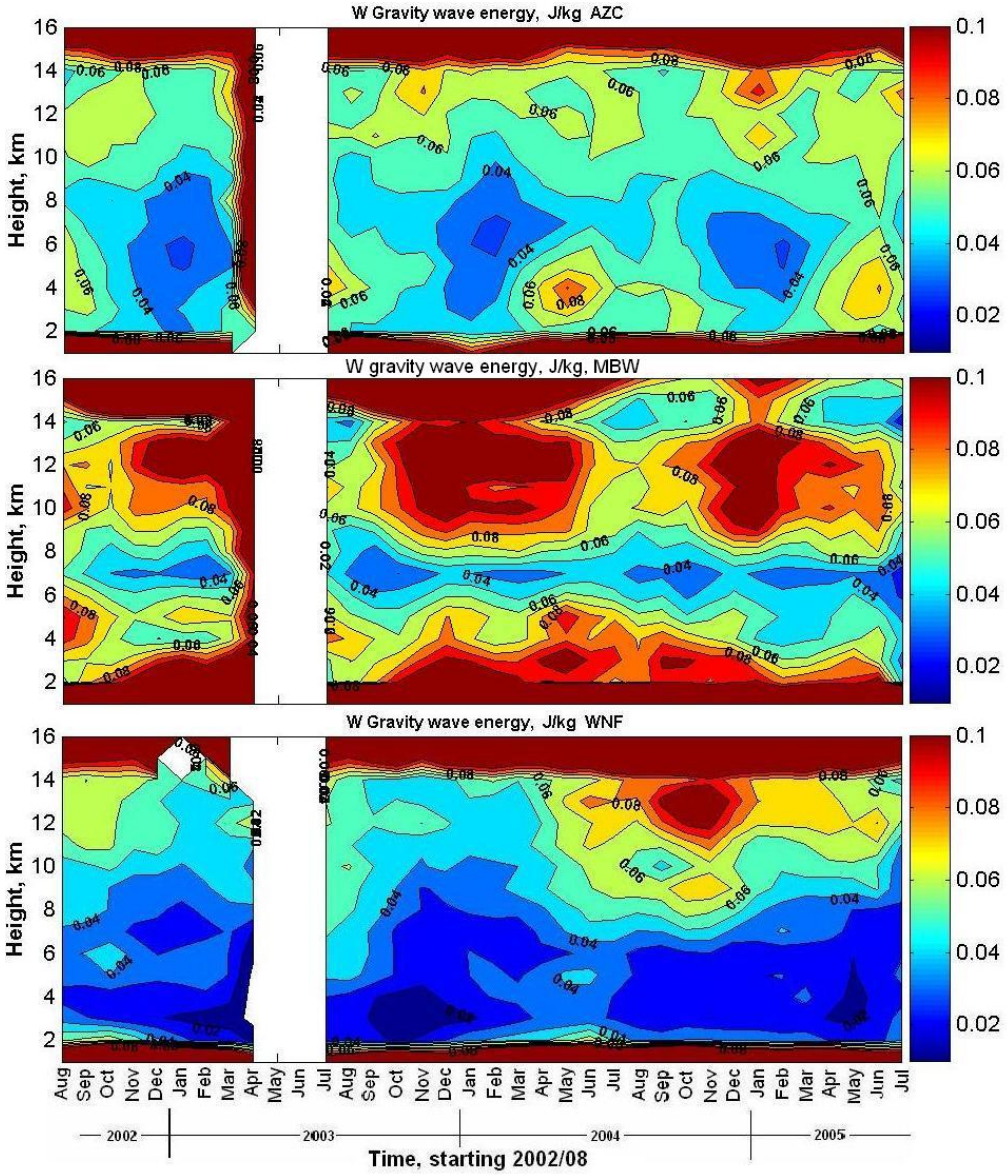

Figure 5.4. Same as figure 5.3, but for vertical gravity wave energy.

This figure presents the time-altitude fields of gravity wave kinetic energy associated with vertical component for the AZC, MBW and WNF profilers. These plots are obtained as the sum of low-, mid and high-frequency gravity wave energies of the vertical component.

The amplitudes of the vertical component of the wave kinetic energy in figure 5.4 are varying within 0.03 - 0.1 J/kg and up to 0.15 J/kg in some episodes. This is significantly smaller than the magnitudes obtained from the vertical wind variance (0.2-0.5 J/kg and up to 1 J/kg in extreme events). The general features of the gravity wave kinetic energy fields show poor similarity between the spectral analysis and the variance. Only the most prominent features, like the maximum in upper troposphere in October-December 2004 for the WNF or winter maxima at ~10 km in 2003/2004 and 2004/2005 for the MBW could be identified on both figure 5.2 and 5.4. The only explanation for these differences that seems feasible is the previously mentioned limitation of the spectral method that requires long uninterrupted data segments and therefore may omit periods of "active" atmospheric processes that make some data unusable or introduce gaps in data.

Another interesting feature of figure 5.4 is that the MBW profiler location has significantly higher gravity wave activity both in lower troposphere and at ~9 - 13 km, than the rest of the sites. This strong activity is present only in the vertical component of the gravity waves - the total gravity wave energy plots do not indicate significant enhancement at the MBW location. While the enhanced wave activity in the lower troposphere is easily explained by the topography of the location (MBW is the site at the highest altitude of all sites, located in the Rocky Mountains), the reason for high magnitudes of wave activity at ~9 - 13 km is unclear. Additional study is required to

clarify, if vertically propagating gravity waves generated by the mountains upstream are the responsible for this enhancement.

In the variance data at altitudes of 14 km and up the vertical component of the wave energy has uniformly high magnitudes. These high values seem to be unreasonable, as they are not present on the total energy plots, and have an abrupt lower boundary at almost constant altitude. Most likely this feature represents the upper boundary of reliable vertical wind measurements by the NPN wind profilers, and appears to be due to poor performing of the Doppler shift estimation algorithms in low signal-to-noise conditions.

In the plot 5.4, the lower 2 km have significantly larger wave energies than in the midtroposphere. Due to the scale, chosen for the plot, the structure of wave energy in this height range is not readily visible. Additional analysis of plots of gravity waves energy associated with vertical component for the lower troposphere (not shown) has revealed that vertical gravity wave kinetic energy in that height range (1-2 km above ground) has distinct seasonal variations, with two regimes occurring at different locations: 1) with maximum in summer and minimum in winter, occurring for both high- and low-frequency waves, and 2) with maxima occurring in winter for low frequencies and summer for high-frequencies, producing rather uniform total vertical gravity wave energy in that region. As an explanation for such structure we can suggest that three sources of gravity wave generation - convection (in summer), orographic generation (by stronger low-level winds in winter) and the jet-stream, are superimposed, and produce observed complex structure. These seasonal changes are usually more pronounced for the high- and medium-frequency waves, and occur less often for the low-frequency waves.

5.4 Zonal and meridional distribution of total gravity wave energy

In order to assess the meridional and zonal climatology of the gravity waves, total gravity wave energy data from multiple profilers was averaged within 1° latitude (longitude) bands. The meridional and zonal distributions were created separately for three altitude levels: lower troposphere (averaged over the heights 1-2 km), midtroposphere (heights 4-6 km) and upper troposphere (heights 8-9 km). The time evolution of these distributions is presented below, in figures 5.5 - 5.10.

The meridional distributions (figures 5.5 - 5.7 for lower, mid- and upper-troposphere correspondingly) cover the area from 32º N to 45º N.

In the lower troposphere, there is no distinct latitudinal dependence of the total gravity wave energy. Local maxima are visible in winter at ~ 36º N and 43º N, and might be the result of topographic excitation of gravity waves by low-level winds. The latitude of 36º N corresponds to the location of the Ouachita and Boston Mountains, while 43º N could be affected by Medicine Bow, Laramie Mountains and Black Hills. During active periods the energies do not exceed 10 J/kg and usually are within 4-8 J/kg.

In the midtroposphere, an obvious meridional gradient of total gravity energy is observed, superimposed on seasonal variations. The maximum is present every winter at 42 - 44 º N, with energies up to 10 - 12 J/kg. No enhancement is observed at 36º N and 43º N, suggesting a different mechanism of wave generation responsible for the observed gravity wave structure in the midtroposphere. It is interesting that winter maxima start at 42 - 44 º N in October-November and then propagate southward within 2-3 month. Similarly, in the lower troposphere (figure 5.5) the local enhancements first appear at ~43 º N and a month or two later – at 36º N.

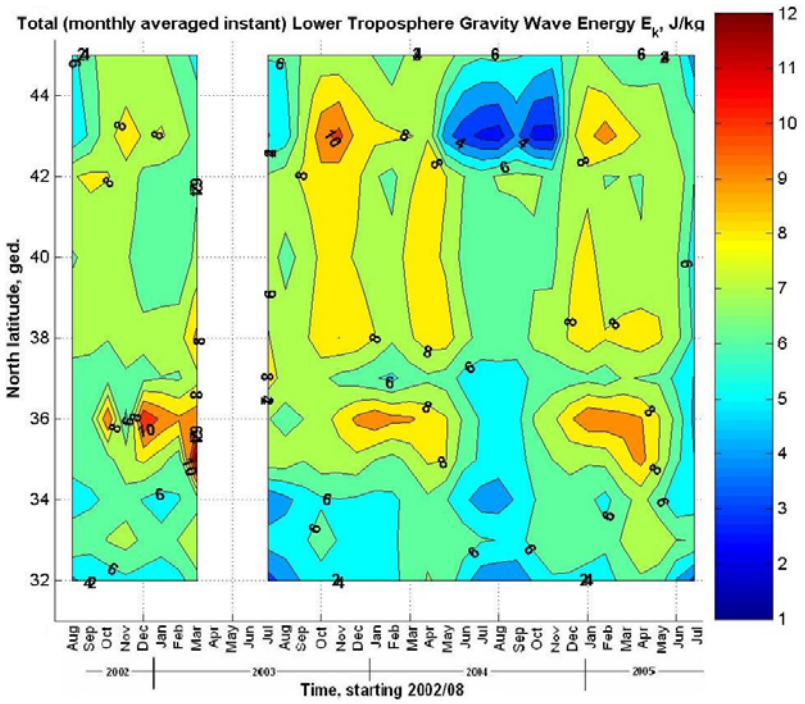

Figure 5.5. Meridional distribution of total gravity wave energy E_K for the lower troposphere.

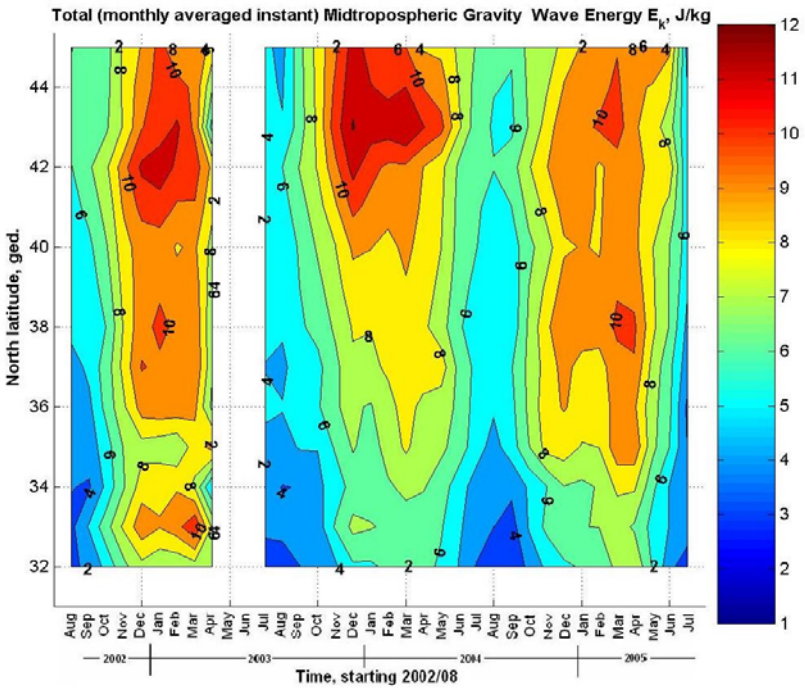

Figure 5.6. Same as figure 5.5, but for the midtroposphere.

In the upper troposphere, the meridional distribution is very similar to that in the midtroposphere, with magnitudes about twice as large, up to 25 J/kg for winter maxima. Within the plot latitudes, the gravity wave energy increases poleward, and, based on figure 5.7 it is difficult to judge if the maximum is located at 44º N or larger values could be observed further north. Summer minima have typical values of ~ 8 J/kg. Similar to figure 5.6, the winter episodes of increased gravity wave activity propagate from north to south.

The zonal distribution (shown in figures 5.8 - 5.10 for the lower, mid- and upper-troposphere) covers the area from 89º W to 108º W, with a 2-degree gap at 103-105º W. There are no NPN operational wind profilers located within these longitudes.

In the lower troposphere, we observe a lack of defined longitudinal structure of the total gravity wave energy. Weak local gravity wave activity enhancement is visible in winter at 99º W and, to a lesser extent, at 91º W, with magnitudes up to 10 J/kg. Outside of the active periods the energies are usually within 4-7 J/kg. The longitudes of 99º and 91º W do not seem to correlate with any significant topographic features, but, as mentioned above, the Ozarks, Ouachita and Boston Mountains are located just 1º west from 91º W so topographically generated gravity waves propagating downstream could be the cause of that feature. The reason for the seasonal increase of the gravity wave energy at 99º W most likely is not related to topography.

In the midtroposphere (figure 5.9), a consistent seasonal and zonal pattern of total gravity energy is observed.

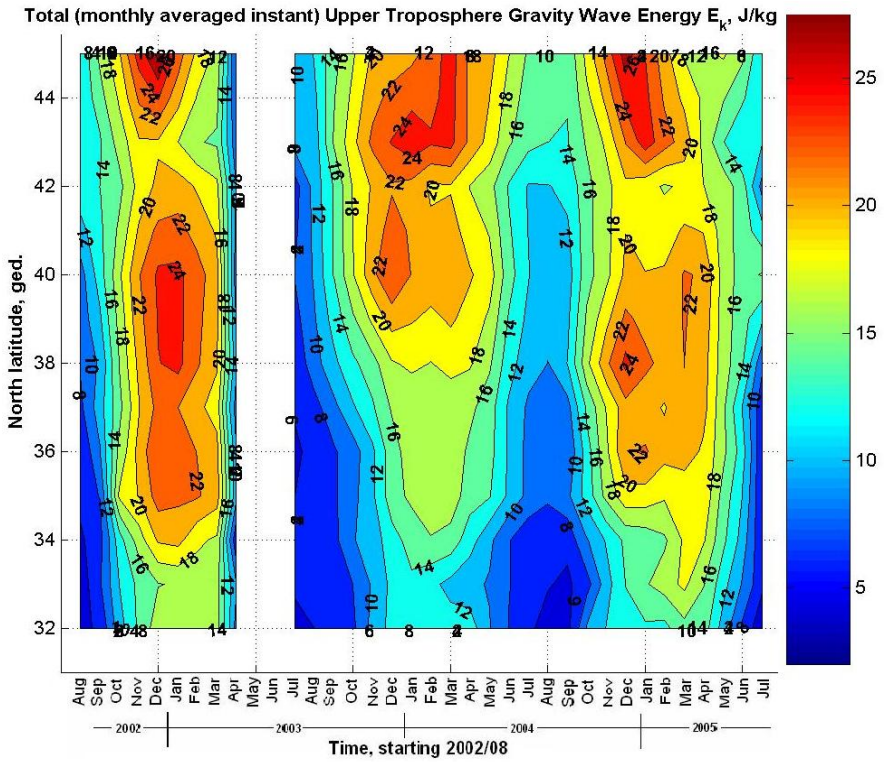

Figure 5.7. Same as figure 5.5, but for the upper troposphere.

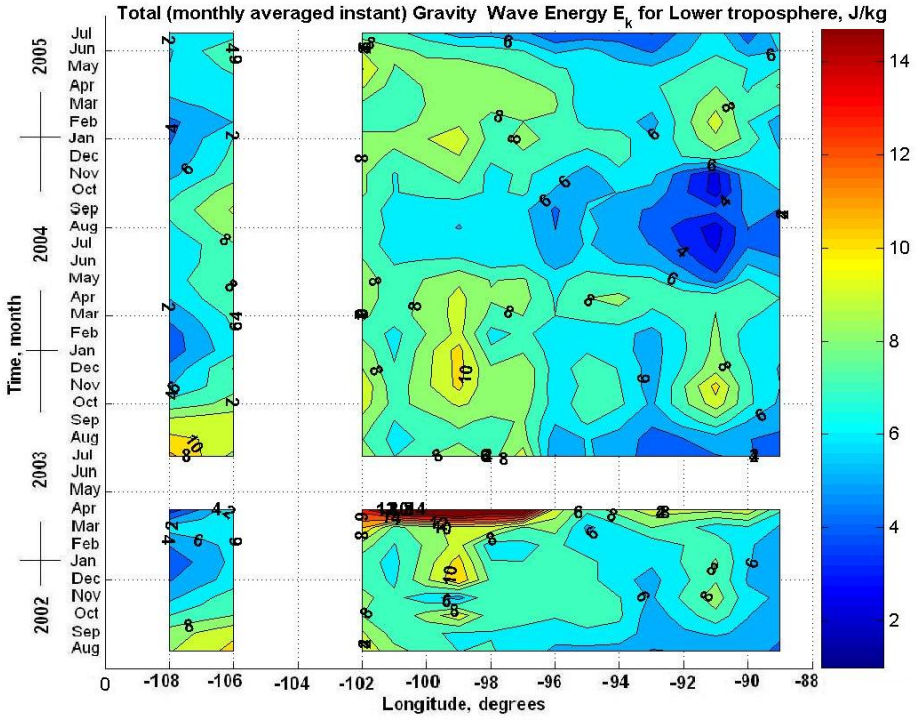

Figure 5.8. Zonal distribution of total gravity wave energy E_K for the lower troposphere.

Local gravity wave energy enhancements were found at 91º W and 95º W and in all western parts of the plot (102 - 108º W) in winter/early spring, with energies up to 10 - 14 J/kg. Strong wave activity in the west is a very robust and distinct feature, clearly visible despite the gap in the data at 103 - 105º W. Longitudes of 106-108º W correspond to the eastern branches of Rocky Mountains and, according to figure 5.9 are the most wave-active areas. The winter increase of wave energy at 99º W, present in the lower troposphere does not appear in the midtroposphere, while similar features at 91º W and 95º W are present.

In the upper troposphere (figure 5.10) the structure of the zonal distribution of gravity wave energy is more complicated than at lower altitudes, and apparently, has no significant longitudinal dependence, unlike in the midtroposphere. Winter maxima of wave energy are located at 99º, 97º, 95º and 91º W, while some irregular enhancements appear at 90º W. The organization of maxima seems to be periodic in the zonal direction, with 2º spacing. Amplitudes reach 24 J/kg in winter and are within 8-10 J/kg in summer. Another interesting feature of the upper tropospheric energy distribution is the absence of a maximum above the Rocky Mountains, which was found in the midtroposphere. It's not clear as of now, what is the cause of the different gravity wave structure in the upper troposphere.

The time variation of the total gravity wave energy averaged over all 25 profilers is shown in figure 5.11 for the lower, mid- and upper troposphere. The seasonal structure of the gravity waves is obvious at this figure, and, interestingly, while higher in winter, the energy in the midtroposphere is lower in summer, than in the lower troposphere.

The 3-year time averaged gravity wave energies for each profiler are shown in figure 5.12 for lower, mid- and upper troposphere.

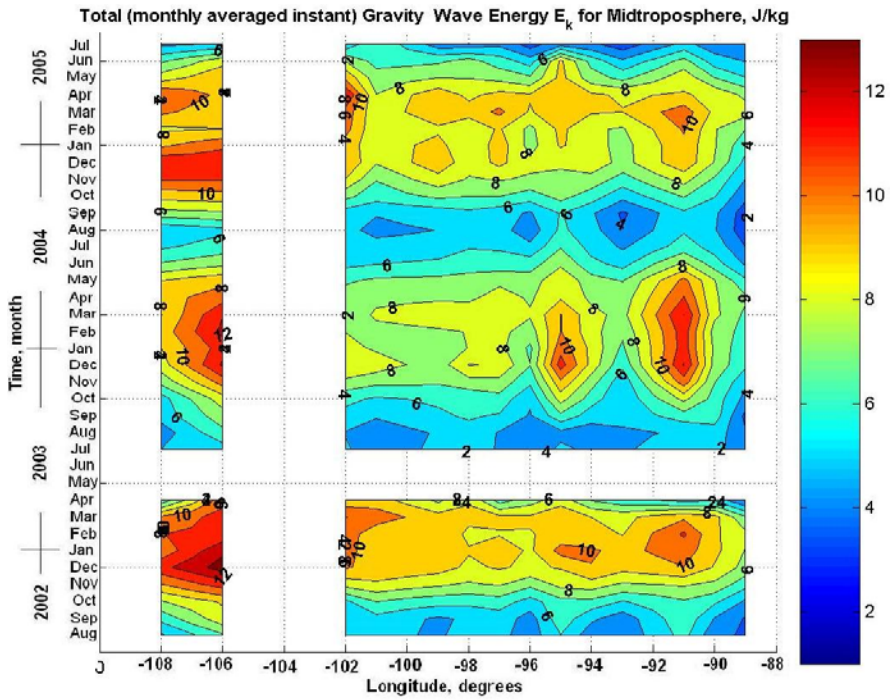

Figure 5.9. Same as fig. 5.8, but for the midtroposphere.

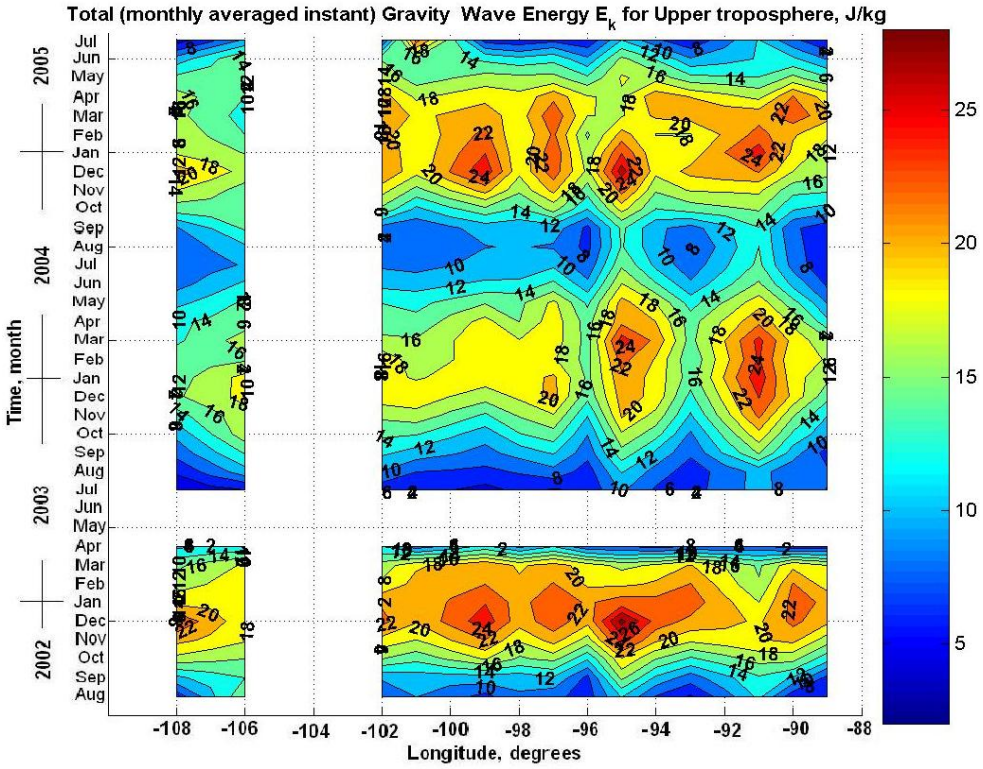

Figure 5.10. Same as fig. 5.8, but for the upper troposphere.

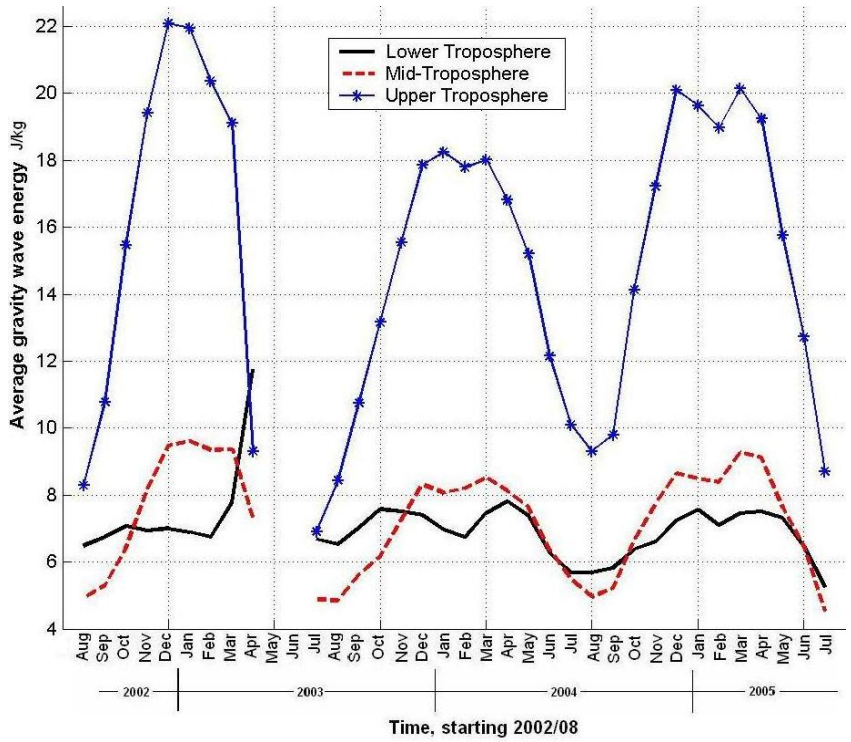

Figure 5.11. Total gravity wave energy variation in time, averaged over 25 profilers, for the lower, mid- and upper troposphere.

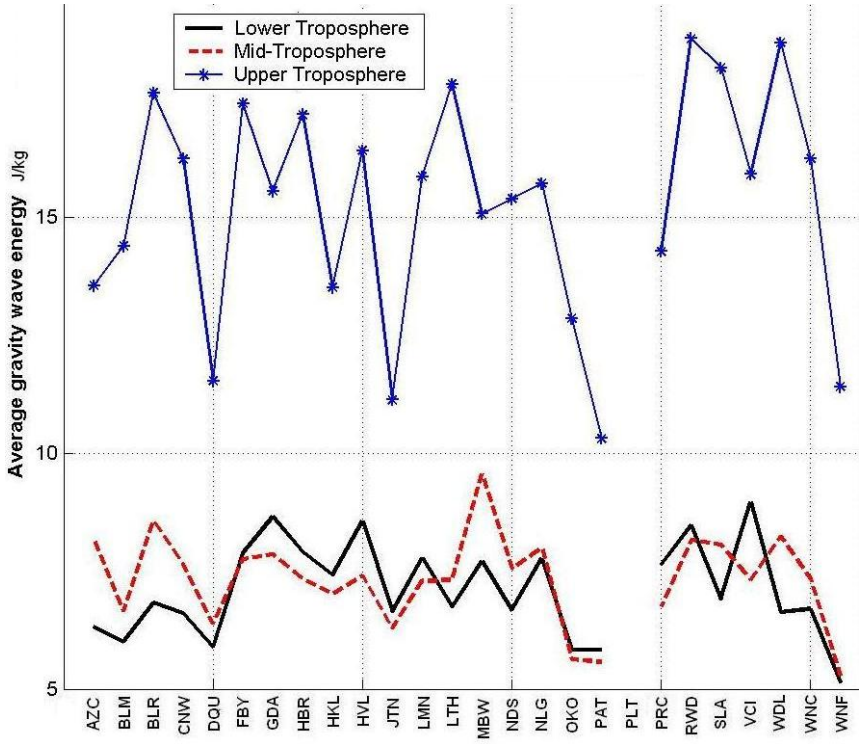

Figure 5.12. The 3-year time average of the total gravity wave energy for each profiler for the lower, mid- and upper troposphere.

5.6 Analysis of the wave generation sources

The analysis of altitude and time dependences of the total gravity wave energy, as well as the geographical distributions, resulted in suggestions about the wave generation mechanisms responsible for the observed patterns. Zonal wind and its vertical shear, convection and topography are known to be important wave generation sources. A detailed consideration of topography and its effects on gravity wave generation will be described in the following chapter. In this section, we quantitatively estimate the relative importance of the vertical shear of the horizontal wind and convection (using the precipitation as a proxy for convective activity) for generating different components of the total gravity wave energy (low-, mid- and high frequency, as well as u, v and w components) at different altitudes. To do this we have assessed the time correlation between gravity wave energy and 1) vertical shear of the horizontal wind defined and obtained as in section 3.1; 2) precipitation rate. For a precipitation rate both reanalysis and raingauge data were used. The correlation coefficients were calculated for each of 25 wind profilers, at altitudes from 1 to 16 km. Then the vertical profiles of the correlation coefficients were averaged between all profiler sites. The resulting plots are presented below.

Figure 5.13 shows the dependence of correlation coefficients on height for the zonal component of gravity waves. The correlation coefficient of high-frequency wave energy versus precipitation rate is positive below 6 km, and reaches a maximum value of 0.4 at 3 km height. At higher altitudes the correlation is low (~ 0.2) and negative. The correlation of high-frequency wave energy versus wind shear has a maximum of ~ 0.5 at 9 km and has a sign opposite to the sign of the precipitation correlation curve.

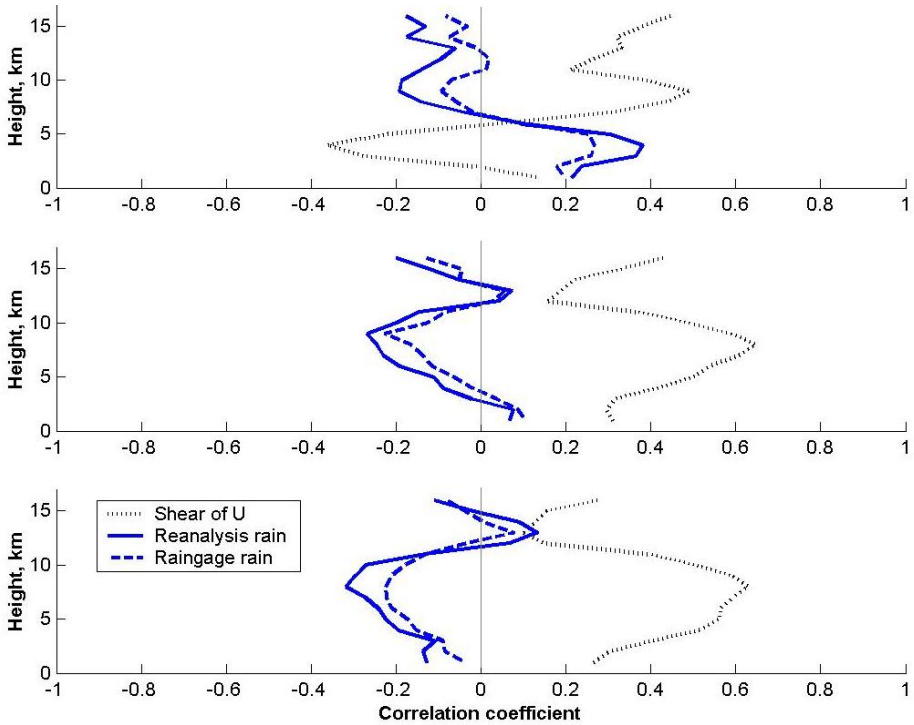

Figure 5.13. Vertical profiles of correlation coefficients of the zonal component of the E_k vs. rainfall rate (solid and long-dashed lines); zonal component of E_k vs. shear of horizontal wind (dotted line). The correlations are for high- (top), medium- (middle) and low-frequency waves (bottom).

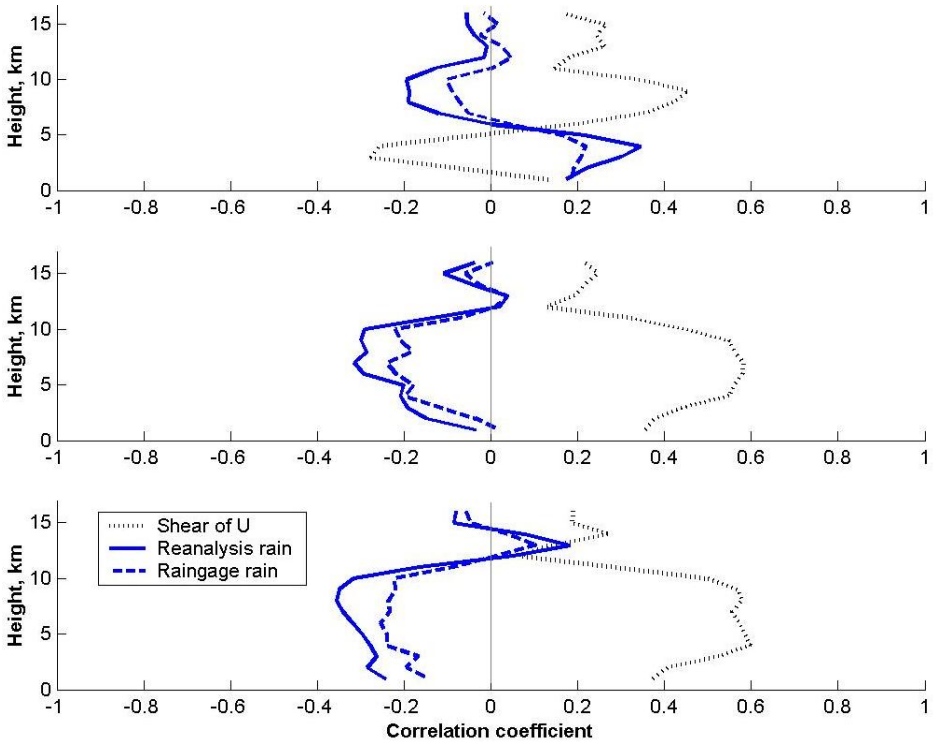

Figure 5.14. Same as fig. 5.13 but for the meridional component of E_k.

The correlation coefficient profiles for the medium- and low-frequencies are very similar, and have the following main features:

- Correlation coefficients for rainfall rates are close to zero, and have a minimum of -0.3 between 5 and 10 km;
- Correlation coefficients for horizontal wind shear are close to zero at the ground, and steadily grow to a maximum of 0.65 at 7 km, then decrease to 0.2 at about 12 km, and increase again above that.
- The plots for rainfall and for shear correlation coefficients have opposite sign, which agrees with the fact that strong wind shear often opposes convective development, and, therefore high shear corresponds to low precipitation rates.

Figure 5.14 presents the dependence of the correlation coefficients on height for the meridional component of the gravity waves. These plots are very similar to the ones discussed above for the zonal component of the wave energy, with comparable characteristic altitudes and values of correlation coefficients.

The vertical profiles of the correlation coefficients of the vertical component of gravity wave energy versus precipitation rate and wind shear are presented in figure 5.15. The correlation with precipitation has a positive sign at all altitudes, and has a maximum of ~0.5 at 2 to 3 km (high frequency waves). The same magnitude of maximum correlation is observed at ~7 km for mid-frequency waves and ~8 km for low-frequency waves. The correlation coefficients with wind shear have opposite sign and a maximum at similar altitudes as for precipitation, but the magnitude of maximum correlation is slightly lower, at about -0.4.

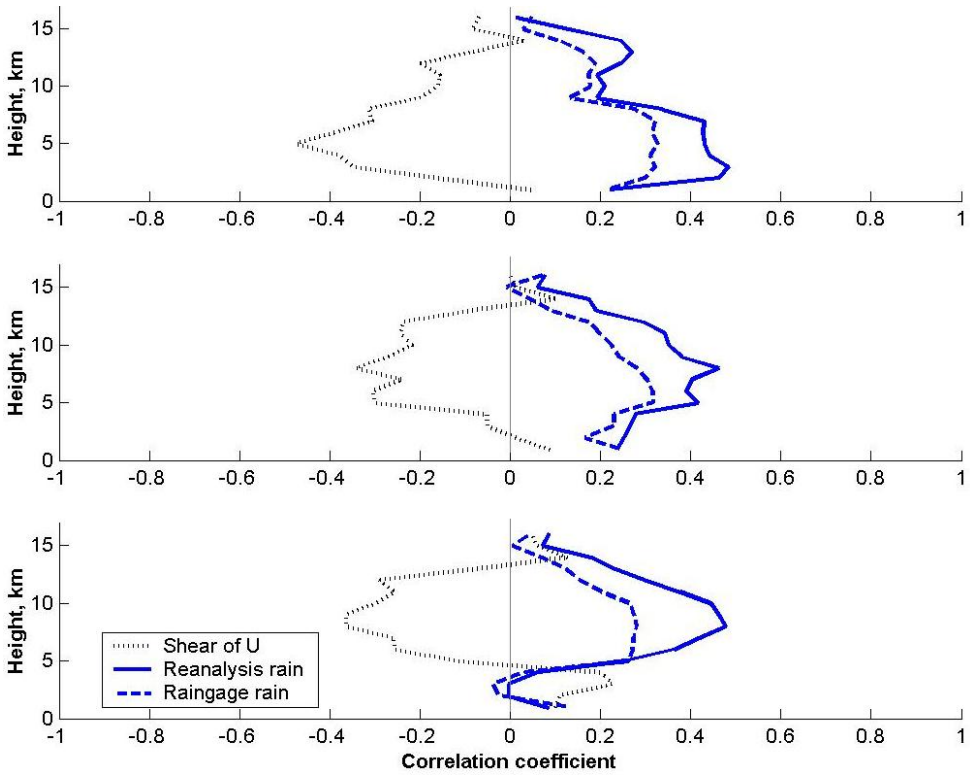

Figure 5.15 Same as fig. 5.13 but for the vertical component of E_k.

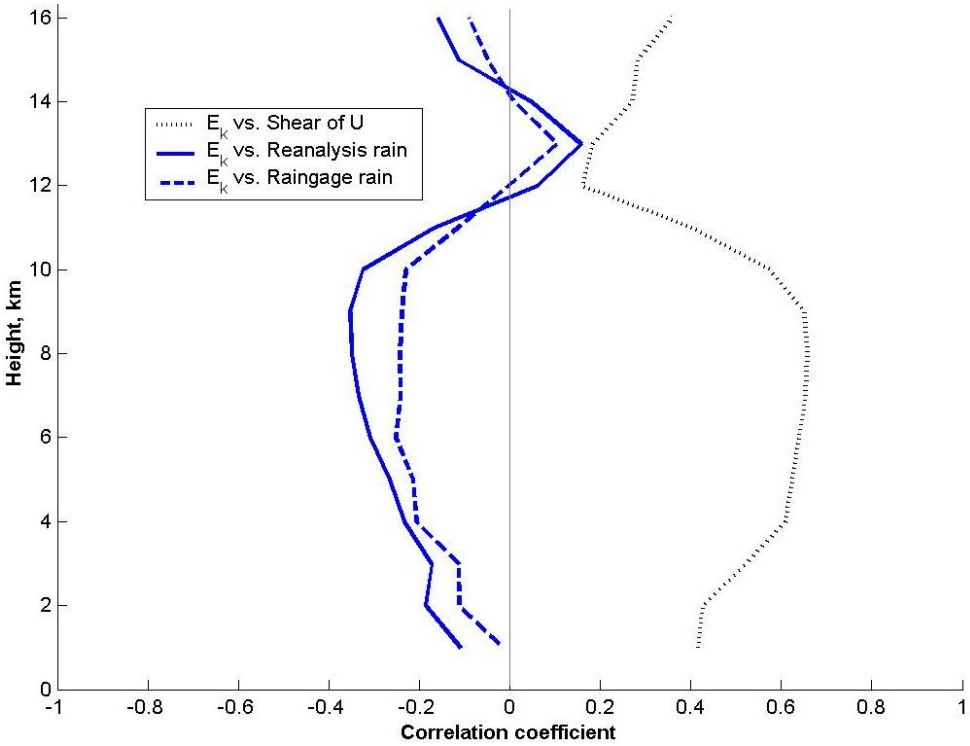

Figure 5.16 Same as fig. 5.13 but for the total gravity wave energy.

The dependence of the average correlation coefficients of total gravity wave energy vs. rainfall and horizontal wind shear is presented in figure 5.16. It was obtained as an average for 25 wind profilers, the same way the partial correlations were obtained above. The shape of the correlation (total energy vs. shear) resembles the one for both zonal and meridional components, with a smooth maximum of 0.6 - 0.65 at altitudes from 4 to 9 km. The correlations then decrease to almost zero at ~13 km. The correlation coefficients (total energy vs. rainfall) have opposite sign than (total energy vs. shear) and smaller values, similarly to the features discussed above in the plots 5.13-5.15.

It needs to be noted that the vertical profiles of the correlation coefficients for the individual wind profilers (not shown) have similar features, but the maxima of the correlations are observed to have higher values, typically 0.7-0.8. The altitudes at which these maxima occur do vary, though. Therefore on average (figures 5.13-5.15) the vertical dependence of the correlation coefficients is smoother, but they have smaller maximum values. Another interesting feature that has to be mentioned is that the correlations are typically higher for reanalysis rainfall then for raingauge rainfall rates.

The observed correlations and the height dependence of the correlations suggest a significant role for horizontal wind shear in the generation of most of the gravity wave energy in the middle and upper troposphere.

The fact that observed correlations (for vertical component of E_k vs. precipitation, and high-frequency zonal and meridional component of the E_k vs. precipitation in the lower and mid-troposphere) are higher for reanalysis rainfall than for raingauge rainfall even for profiler sites located extremely close to the raingauges, suggests that it's not the rain itself that is important for gravity wave generation. Instead, a condition of the

atmosphere that is favorable for the development of convection is probably a better indicator of possibility for gravity wave generation, and this condition seems to be better captured by the reanalysis. In order to prove this hypothesis a study that directly compares atmospheric stability with high-resolution gravity wave energy data would be necessary.

Convection as a generation mechanism was found to be important for high-frequency waves at 2-3 km, and for the wave kinetic energy associated with vertical component. Convection seems to be an important generation source of the vertical component of the energy at all altitudes up to 13 km. Below 2 - 3 km convection and horizontal wind shear need to be supplemented by another mechanism to explain the seasonal and spatial distribution of the gravity wave energy. Analysis of zonal and meridional distributions of the wave energy in section 5.5 suggests that topography might be such a source.

In the following chapter this assumption is given a more detailed and quantitative consideration.

CHAPTER 6

TOPOGRAPHY VARIATIONS AND ITS EFFECT ON GRAVITY WAVES OBSERVED BY NPN

In this chapter we propose a simple technique for the quantitative characterization of the terrain surrounding wind profiler measurement sites. The general approach is described in section 6.1; in section 6.2 we apply the suggested technique to evaluate the topography variation around the NOAA Wind profiling Network sites, and give a simple classification of different terrains in terms of our quantitative estimates. Section 6.3 presents the application of the topography quantification results to the analysis of gravity wave sources.

6.1 Method for evaluation of topography variations

The Point Cumulative Semivariogram (PCSV) technique, used by Z. Sen (1999) to obtain the quantitative characterization of behavior of some arbitrary variable *S* around the site, is based on the analysis of behavior of the function

$$y(d_i) = \frac{1}{2}\sum_{i=1}^{m-1}(S_r - S_i)^2 \ , \qquad (6.1)$$

with distance *d*, where S_r - variable at reference site (site of interest), S_i - variable at distance d_i. This PCSV is basically a non-decreasing sum of half-squared differences of variable S between the site of interest and surrounding sites, or in other words, a *cumulative sample variance*. This technique, while giving a valuable hint as to how to

deal with the problem of quantifying the terrain, needs significant modification if used in atmosphere-related applications.

First, the direction of wind has to be taken into account because of the following. Even significant variations of terrain are not going to affect atmospheric conditions if this terrain is relatively far downstream from the site of interest, i.e. mean air flow is from site toward the terrain.

Second, due to the dissipation and (or) propagation of excitations at some angle upward, the effect of terrain will become negligible when distance from the site of interest would exceed some threshold value; i.e. some distance scaling should be introduced.

Third, to obtain an *integral* quantity which can be used for quantitative comparative analysis of different sites, the function (i.e. the variances) should be summarized.

The suggested modifications can be summarized in mathematical form, and the integral estimate of wind weighted topography variations Δ_h expressed as

$$\Delta_h = \iint_{r,\varphi} Var_h(r,\varphi,h) \cdot R(r) \cdot V_h(\varphi,h) \cdot dr \cdot d\varphi \,, \qquad (6.2)$$

where: Δ_h - surface roughness estimate, Var_h – variation (variance) of topography in a $d\varphi \times dr$ bin (terrain is considered to be changing uniformly over the bin), *R(r)* - some decreasing function of distance from site, $V(\varphi, h)$ – probability of the horizontal wind from azimuth φ at the altitude h; φ changes from 0 to 360°, and r – from 0 to some R_{max}, radius of influence.

The method is illustrated in figure 6.1. In order to be able to compare the estimates for different sites obtained for different radiuses of influence, it's reasonable to introduce scaling by the total area included into the calculations. The final form of the expression for Δ_h modifies to

$$\Delta_h = \frac{1}{Area} \iint_{r,\varphi} Var_h(r,\varphi,h) \cdot R(r) \cdot V_H(\varphi,h) \cdot dr \cdot d\varphi \ . \qquad (6.3)$$

In the following paragraphs we will discuss the considerations relevant to the choice of the radius of influence, the distance and wind weight functions, as well as the available elevation data sources.

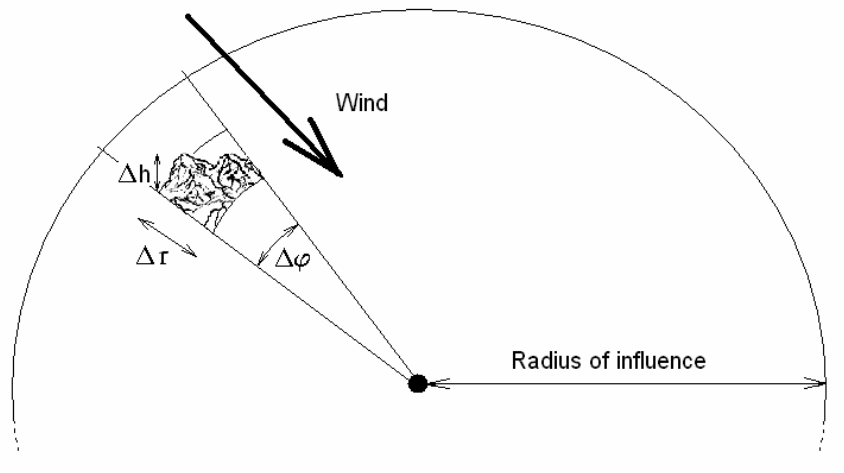

Figure 6.1. An illustration of the proposed technique for wind-weighted topography quantification.

Radius of influence.

The choice of the radius of influence is dictated by factors specific to the application where the estimate of topography variations is going to be used. The upwind fetch or source area affecting the wind speed measurements depends on surface roughness, wind speed, atmospheric stability and other characteristics (De Vries et al., 2003; Schmid, 1994). When interpreting NPN measurements of winds, the altitude

coverage of the wind measurements (500 – 16250 m) will be one of the defining factors. The results of De Vries et al., (2003) and Schuepp et al. (1990) show that for measurement heights from 3 to 10 m, surface features upwind from ~100 m to 1000 m have the most influence on the observations. If we scale the above ratio for wind profiler radar operating altitudes, then the radius of influence will be estimated between 160 and 1600 km. The upper limit of this radius of influence, determined by simple scaling, seems unacceptable for several reasons. First, this is a scale of weather systems and Rossby waves, therefore the wind field can not be considered uniform over the circle of the influence. In order for the wind field to be assumed uniform, the linear size of the area should be an order of magnitude less than the scale of weather systems, i.e. close to 100-200 km. Second, at the radius of ~1000 km the bin size will become significantly large (an order of ~170 km for $\Delta\varphi=10°$) to include terrains of different types. Third, the use of gridded elevation data with resolution high enough to capture the terrain features over the area of ~1000×1000 km (for each of the sites) would impose size and performance limitations for numerical calculations.

From the other side, results of the studies using modeling of the gravity waves generated by convection and, similarly, by orographic features, indicate that the gravity wave propagation is inclined; therefore the waves can vertically propagate out of the altitudes of interest. For example, modeling results of Beres et al., (2002) show that at distances over 200-400 km the gravity waves will propagate up and leave the altitude domain of interest - altitudes up to 10-15 km. Here we leave out of consideration some infrequent wave propagation phenomena, such as wave reflection, etc.

Based on the aforementioned considerations (scaling, modeling results, wind field uniformity and computational limitations) we have chosen two values of radius of influence, R=100 km and R=200 km for our further calculations. The calculations performed for two values can also allow for coarse assessment of the changes of topography close to the sites versus far from the sites. It should be note here, that by our choice of radius of influence we have left out of consideration the phenomena of distant wave propagation, e.g. trapped waves or near-horizontally propagating large-wavelength gravity waves, as they are not characteristic for the topography surrounding the site.

Wind weighting function.

To obtain the proper wind weighting function, we have used the following approach. First, we have considered the wind field as uniform all over the circle of influence, as discussed in the previous paragraph. Second, the characteristics of the wind field data were obtained for the location of the site of interest (center of the circle), and were assigned as a reference for the whole circle. Wind measurements at the site are readily available as the site location coincides with a wind profiler radar location. Based on the ~3 years of horizontal wind measurements by the wind profilers we have obtained the probabilities (relative frequencies of occurrence) of both the wind direction and the magnitude at each height level – from 500 m to 16250 m. Sample wind direction probabilities for 500 m, 1500 m and 5250 m are shown in figure 6.2 and 6.3 for two profiler sites, AZC and FBY. The graphs for the other NPN stations have, in general, features similar to either the AZC or FBY plots.

Two features of interest in the context of wind weighting were found. First, the most frequent direction of the wind coincides with the direction of the wind with strongest

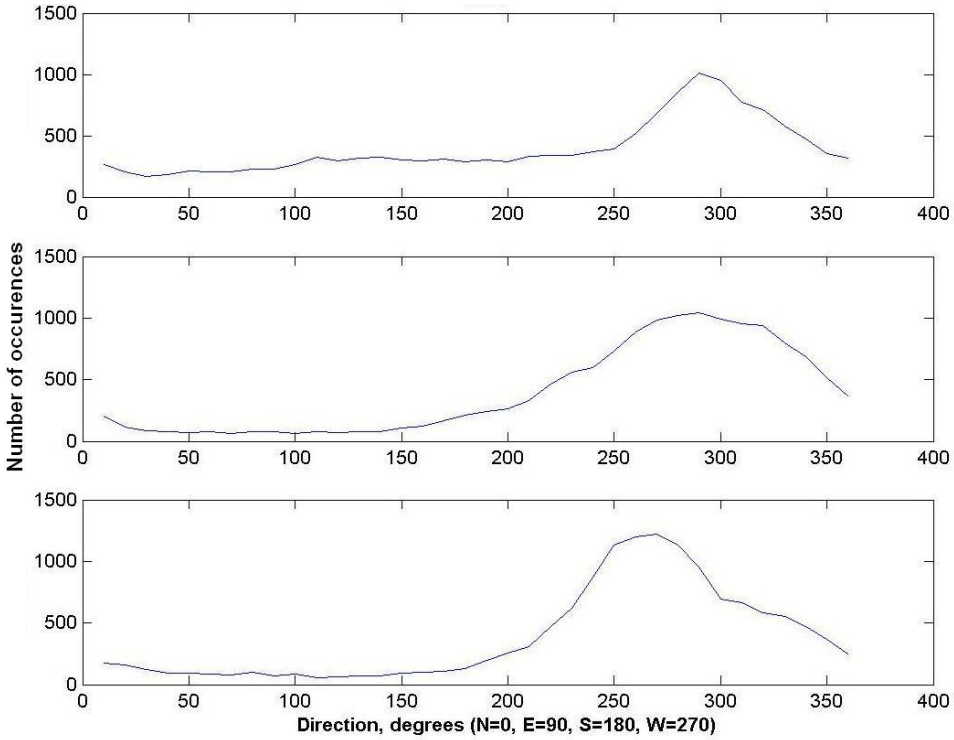

Figure 6.2. Relative frequency of occurrence of the wind direction (the azimuth of the direction where the wind is blowing *from*) at altitudes (from the top down) 500 m, 1500 m, 5250 m for the AZC wind profiler.

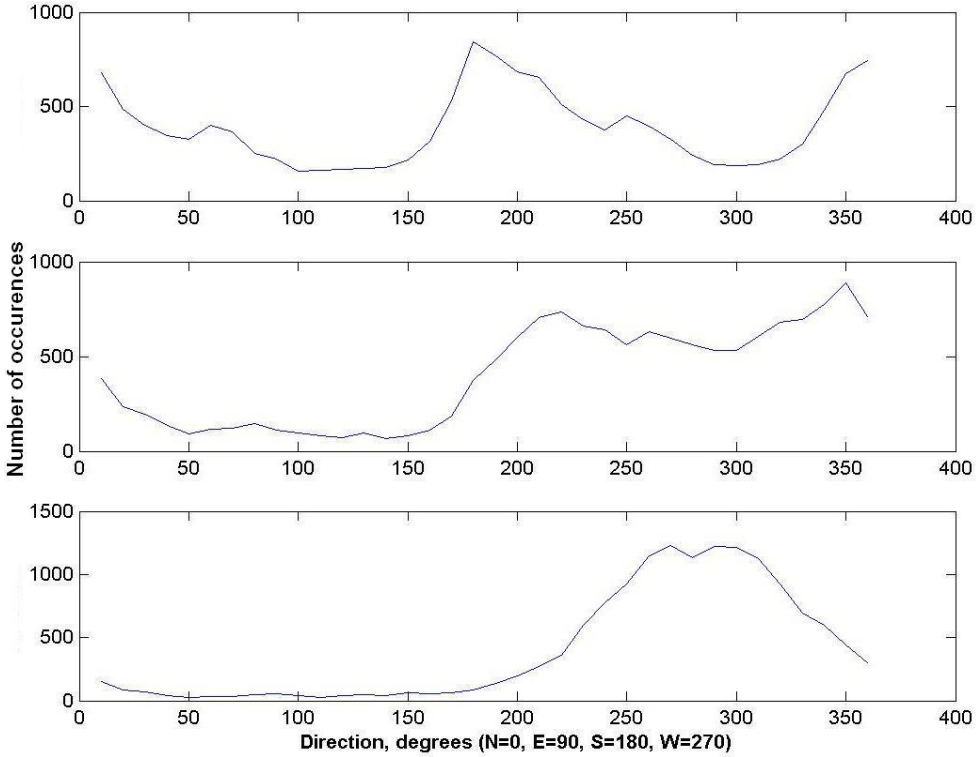

Figure 6.3. Same as previous figure, but for the FBY wind profiler.

magnitude. That is, if we expect most of the winds to be westerlies, then the strongest winds will also be from the west. Second, there were two types of wind distributions observed for the low altitudes, unimodal (as shown on upper part of figure 6.2) and bimodal (upper part of figure 6.3, with two maxima at ~180° and ~360°), while for the free atmosphere the distributions are always unimodal (lower graphs at figures 6.2 and 6.3) with the prevailing wind at ~ 270°. This bimodal structure for some locations shows the importance of using the *site-specific* wind weighting function as it might amplify the affect of topography variations at some azimuths for some locations.

Elevation Data.

The elevation data used for this study were obtained from the USGS 30-arc-second (1-km) gridded, quality-controlled global Digital Elevation Model from the Global Land One-km Base Elevation (GLOBE) Project. These elevation data are freely available from the National Geophysical Data Center, with both plots and data files available at: *http://iridl.ldeo.columbia.edu/SOURCES/.NOAA/.NGDC/.GLOBE/html+viewer*

The elevation data were downloaded for 6°×6° square polygons centered on each profiler location as determined from table 2.1. A sample 3-D plot of the elevations at one of the polygons is shown in figure 6.4.

6.2 Sample calculations for the NOAA Profiler Network sites

As the first approach to obtaining estimates of the topography variation for NPN profiler sites, the expression (6.3) was modified to a simplified version suitable for numerical calculation as shown below:

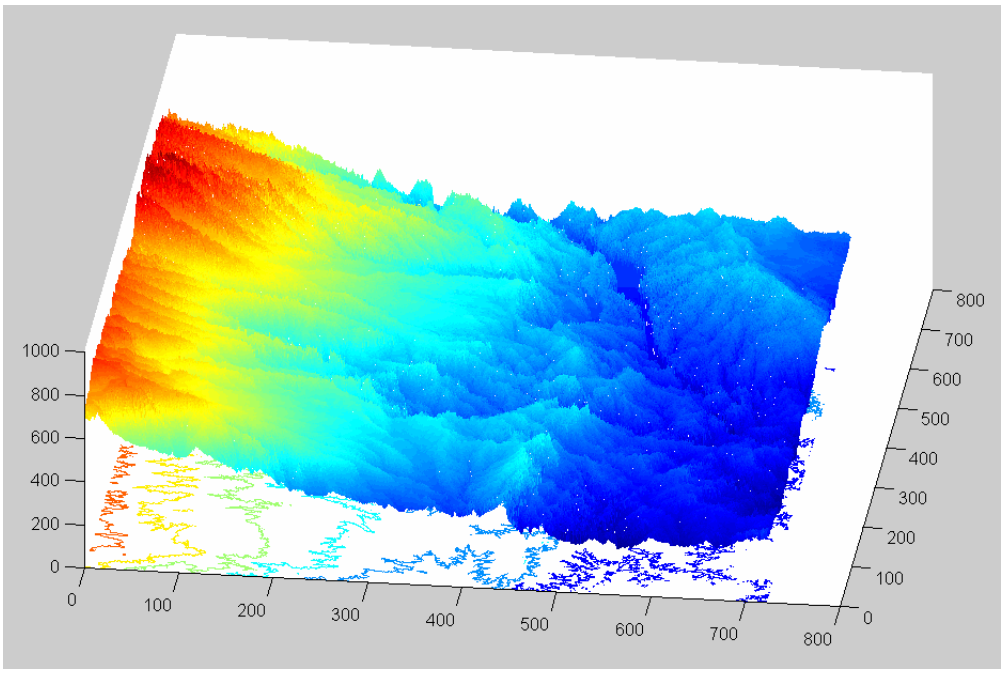

Figure 6.4. Sample 6ºx6º elevation data around the profiler site. X and Y-axis are in kilometers, and Z axis is in meters. The profiler is located at the coordinates (350, 350).

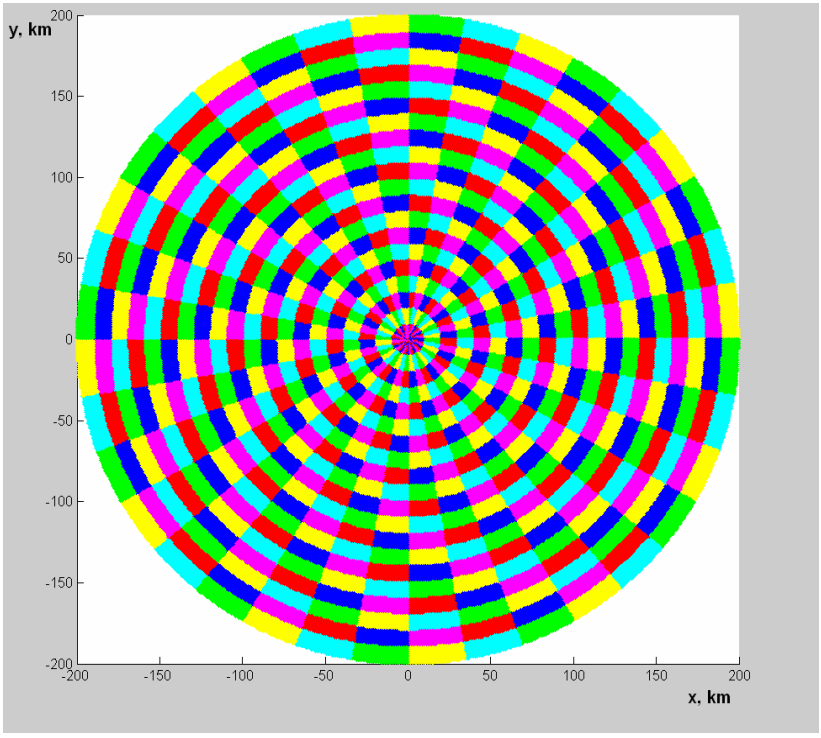

Figure 6.5. Area of influence divided into 10º sectors and 10-km distance bins. Each section is shown in a different color. The measurement site is located at the center of the circle.

$$\Delta_h = \frac{1}{\#\,bins} \sum_{i=1}^{\#bins} Var_i(r_i, \varphi_i) \cdot R(r_i) \cdot V_H(\varphi_i, h_i) \quad , \qquad (6.4)$$

where integration is replaced by summation over (10°, 10-km) bins and scaling by the area – i.e. scaling by the number of bins. The bin layout is shown in figure 6.5.

The calculations were performed according to expression (6.4) for each profiler site, using corresponding individual wind weighting functions and linear distance weighting functions, changing from 1 at 0 km to 0 at 300 km. We have used two radiuses of influence, 100 and 200 km. For the latter radius calculations were done with and without a wind weighting function. The results of the calculations are shown in table 6.1 and in figure 6.5.

Table 6.1 Calculated values of the topography variations Δ_h for the locations of NPN profilers.

Profiler station	Profiler ID #	Elevation, m	Estimate of topography variation Δ_h, m^2, for:		
			R=200 km, no weighting	R=200 km,	R=100 km, weighting
AZC	1	1901	327.54	**240.39**	158.86
BLM	2	129	6.28	5.72	4.75
BLR	3	225	16.78	18.64	27.66
CNW	4	390	11.96	13.38	10.96
DQU	5	195	30.57	22.9	26.8
FBY	6	432	4.37	4.12	3.6
GDA	7	1155	8.58	12.84	5.84
HBR	8	446	4.03	3.49	2.44
HKL	9	218	14.18	11.59	7.83
HVL	10	647	4.64	5.83	4.36
JTN	11	707	10.44	10.12	10.7
LMN	12	306	3.89	3.63	2.62
LTH	13	297	4.64	4.68	5.4
MBW	14	1996	164.38	**143.83**	127.8
NDS	15	265	4.63	4.47	3.84
NLG	16	524	6.17	6.86	7.43
OKO	17	125	4.45	4.23	3.9
PAT	18	119	4.07	3.94	5.16
PLT	19	1500	192.19	**444.89**	238.7
PRC	20	330	55.5	5.1	5.02
RWD	21	800	6.97	7.1	8.06
SLA	22	315	2.73	2.68	2.97
VCI	23	647	8.5	9.45	9.65
WDL	24	318	3.25	3.16	2.6
WNC	25	169	4.47	5.05	5.79
WNF	26	93	2.06	1.96	2.33

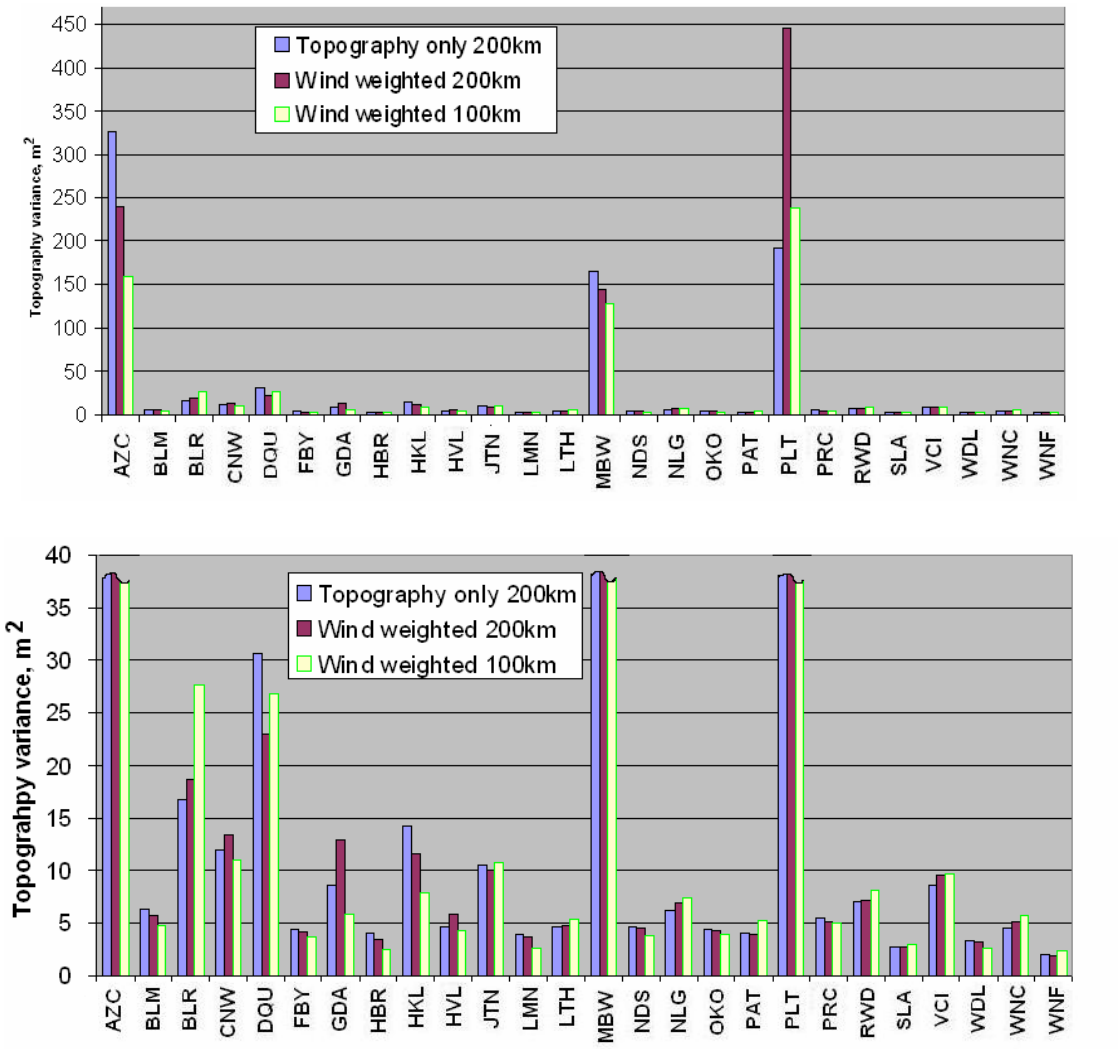

Figure 6.6. Estimates of topography variance for 26 wind profiler sites. Lower plot is scaled to show the details in the lower variance range.

The analysis of the table 6.1 and figure 6.5 leads to the following conclusions:

1. Topography variation for the sites located at the outskirts of the Rocky Mountains (AZC, MBW, and PLT) is significantly larger (150 - 400 m^2) than for the rest of the sites (1 - 30 m^2). This is an expected result which correlates well with the elevations of the sites above sea level (~1900 - 1500 m for AZC, MBW, and PLT versus 100 - 1000 m for the rest of the sites).

2. Several groups of sites with similar values of topography variation within the group can be distinguished, e.g. :
   - very flat terrain sites with $\Delta_h \sim 0 - 5$ m^2 (WNF, SLA, OKO, LMN, and others), located either in the Great Planes or in the low-lands of south-east Texas, Mississippi and Louisiana;
   - relatively flat terrain (e.g. HKL - East Oklahoma, CNW – Ozark Plato, Missouri) with $\Delta_h \sim 5 - 15$ m^2 ;
   - hilly terrain (DQU - Ouachita mountains, Arkansas, BLR - Wisconsin) with $\Delta_h \sim 15 - 35$ m^2 .

Based on this analysis, a preliminary classification of the terrain types is suggested, as summarized in table 6.2. Such a classification would allow for "quick and dirty" comparison of sites where the topography-affected atmospheric phenomena is measured, as demonstrated in the following paragraph.

Table 6.2.Terrain classification based on quantitative estimates of topography variations Δ_h.

Type of terrain	Δ_h, m^2	Example of location
Mountains	>100 - 500	Rocky mountains
Hilly terrain	15 - 35	Ozark mountains, Ouachita mountains, AR
Relatively flat terrain	5 - 15	East KS
Very flat terrain	0 - 5	Great plains, East TX, coastal low-lands

This suggested classification should be considered as only preliminary, until more rigorous analysis is available.

6.3 Gravity wave activity and topography

In order to quantify the effect of topography on the gravity waves, the integral estimates of the gravity wave energy over 3 years at the lower, mid- and upper troposphere for total gravity wave energy and separately for components of the gravity wave energy were used, as obtained in chapter 5, and compared to topography variation estimates, from the above table 6.1.

The results are presented in a table 6.3 and in figure 6.7. Figure 6.7 shows the topography variations and average kinetic gravity wave energy associated with vertical component in the midtroposphere for 25 profiler sites. The correspondence of the two plots is striking, and the average correlation is high (~0.83). Analysis of table 6.3 brings us the following conclusions:

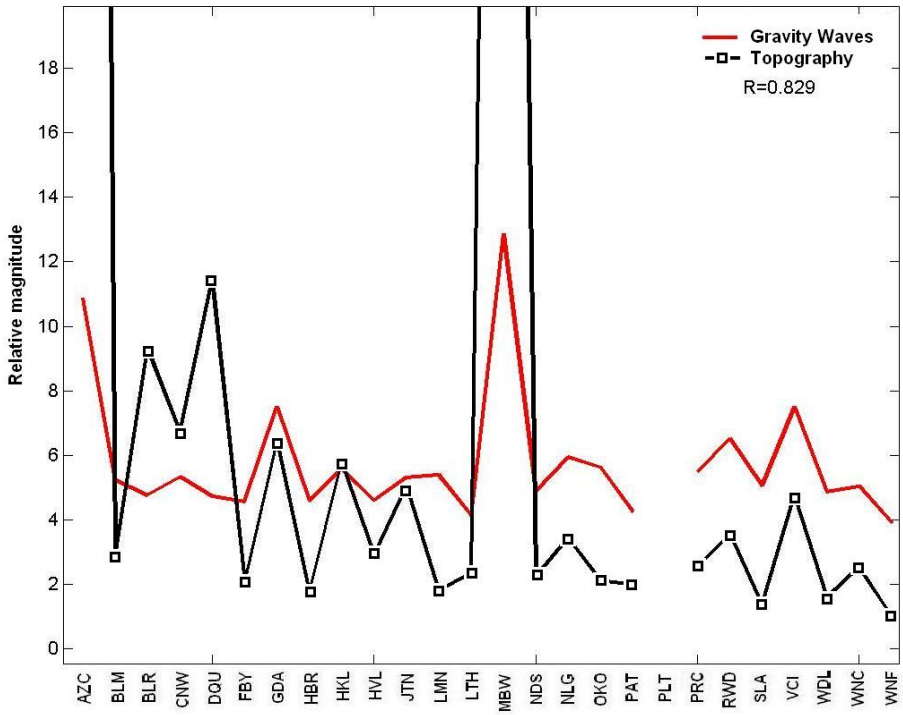

Figure 6.7 The topography variation Δ_h and vertical component of the medium-frequency gravity wave energy for mid-troposphere for 25 profiler sites.

Table 6.3. Correlation coefficient (based on 25 wind profiling radar sites) between 3-year average gravity wave energy and estimates of topography variations Δ_h.

Gravity Wave components	Altitude and gravity wave frequency								
	Lower Troposphere			Mid-Troposphere			Upper Troposphere		
	Frequency			Frequency			Frequency		
	High	Med.	Low	High	Med.	Low	High	Med.	Low
u	0.65	0.55	0.11	0.76	0.71	0.42	0.25	0.25	-0.03
v	-0.01	-0.11	-0.27	0.61	0.44	0.20	0.02	0. 01	-0.01
w	0.18	0.37	0.03	0.63	0.83	0.59	0.36	0.66	0.39
Total Energy	-0.07			0.41			0.01		

- For the midtroposphere, topography is an important source of waves, especially for waves with periods of 1 to 3 hours. The vertical and zonal components of the wave energy are affected by topography the most, and the meridional component- the least, but still significant at high frequencies (correlation of 0.6).
- In the lower troposphere, only the zonal component with high to medium frequencies is generated in significant amounts by topography. This is an interesting result, as not the zonal, but the vertical components are expected to be generated by topography in the case of mountain ranges located in a cross-wind direction.
- In the upper troposphere, only the vertical component with medium frequencies is correlated with topography.

To summarize the findings, the topography was found to be an important source of the gravity waves in the midtroposphere, and to a lesser extent for the zonal component of the low-to medium frequency waves in the lower troposphere and for the vertical component of the medium frequency waves in the upper troposphere.

CHAPTER 7

MULTIPLE REGRESSION ANALYSIS OF THE VERTICAL WINDS AND GRAVITY WAVES

7.1 Regression analysis of vertical wind biases

While the effect of precipitation on vertical wind measurements by UHF profilers was investigated in chapter 4, additional data that are important for the interpretation of profiler measurements were obtained in chapter 5: the distributions of gravity wave energy in altitude and it's seasonal variations. To evaluate the combined effects of precipitation and gravity waves on vertical wind measurement, as well as to estimate the contamination of the vertical wind by horizontal winds due to slight inaccuracies in pointing the radar beam vertically, a linear multiple regression model was used. The vertical wind bias was expressed to be a linear combination of precipitation, gravity wave energy and zonal wind:

$$w' = b_1 + b_2 P + b_3 E_w + b_4 u \,, \tag{7.1}$$

where w' - total bias of vertical wind measurement at time t_i at some height h_j; b_1, b_2, b_3, b_4 – regression coefficients; P - precipitation rate for time t_i; E_w - vertical component of the gravity wave energy at time t_i at height h_j; u - zonal wind at time t_i at height h_j. In matrix form the model for 36 monthly mean observations can be written as

$$w' = Xb + \varepsilon \,, \tag{7.2}$$

where w' is an n-by-1 vector of observations; X is an n-by-p matrix of regressors, b is a p-by-1 vector of regression coefficients; ε is an n-by-1 vector of random disturbances;

n=36 and p=4. The validity of the linear model is justified by the following considerations. The gravity wave effect on the measurement of vertical winds was theoretically studied by Nastrom et al., (1994) and Nastrom and VanZandt (1996). They have shown that the bias of the mean vertical velocity approximately equal

$$\overline{w}_{bias} \approx -\frac{1}{2}\frac{m}{\nu}\hat{w}^2 \ , \tag{7.3}$$

where m – vertical wavenumber, ν - frequency of the wave, $\hat{w}$ - amplitude of the vertical perturbation velocity. It is known that the square of the perturbation velocity is proportional to the kinetic energy of the vertical component of the gravity wave, and therefore the bias is proportional to the vertical component of the wave energy.

The bias due to the contamination of the vertical wind by the horizontal winds appears when the position of the vertical beam is slightly off. In this case the horizontal wind (which magnitude is significantly higher than magnitude of vertical wind) has a non-zero projection on the vertical beam axis that results in a contamination of the vertical velocity by a fraction of a horizontal velocity. This bias is approximately proportional to the sine of the off-vertical angle multiplied by the magnitude of horizontal wind, i.e. also linearly depends on the regressor. In most of the troposphere the zonal wind on a timescale of a month is significantly larger than the meridional, and therefore can substitute for the horizontal wind.

The dependence of the mean precipitation-induced bias derived from the rainfall rates could be a complicated function, as the fall velocities depend nonlinearly on the droplet size, and the precipitation rate in turn is a function of droplet size. But for a fixed altitude the droplet size and therefore the raindrop velocity should be less variable, and, averaged over a one month period (multiple precipitation events with different intensity),

we can expect simpler dependence between rainfall rates and induced velocities. As a first approach we have assumed a linear dependence. This assumption will be additionally checked for validity by assessing the residual errors of the regression fit.

The general least squares solution of the expression (7.3) for the regression coefficient is well known (e.g. Neter et al., 1996), and in matrix form can be written as:

$$b = (X^T X)^{-1} X^T w' \quad , \tag{7.4}$$

where index (^{T}) denotes the transpose and ($^{-1}$) denotes matrix inversion. We have calculated the regression coefficients for altitudes from 1 to 14 km in 1 km steps for each profiler site, using 36-month precipitation rate data from both raingauges and reanalysis, and vertical gravity wave energy for corresponding altitudes as determined in chapter 5. In these calculations *w'* was profiler-measured monthly average vertical velocity, i.e. we have assumed that the synoptic scale vertical velocities are significantly smaller than profiler-measured velocities.

The results of the regression analysis are presented below. In figure 7.1 we present the altitude dependence of the regression coefficients for the DQU profiler, as well as the R^2 statistics (the measure of total variance explained by the model).

DQU was one of the several profiler site with relatively high R^2 statistics (lower plot in figure 7.1) - between 0.6 and 0.7 from the ground up to ~8 km, which is equivalent of 60 to 70% of the variance explained by the model. For several sites the R^2 reaches ~0.6 - 0.7 at one or several altitude levels, and is significantly smaller at others. This altitude of maximum R^2 varies with locations and as a result the average R^2 statistics over the 25 profilers was not very high, about ~ 0.5 for 10 km and decreasing to ~0.3 in

the boundary layer and stratosphere. The altitude dependence of the regression coefficients was the parameter of most interest.

The vertical dependence of the 25-site average regression coefficients for precipitation, zonal wind and gravity waves is shown in figure 7.2.

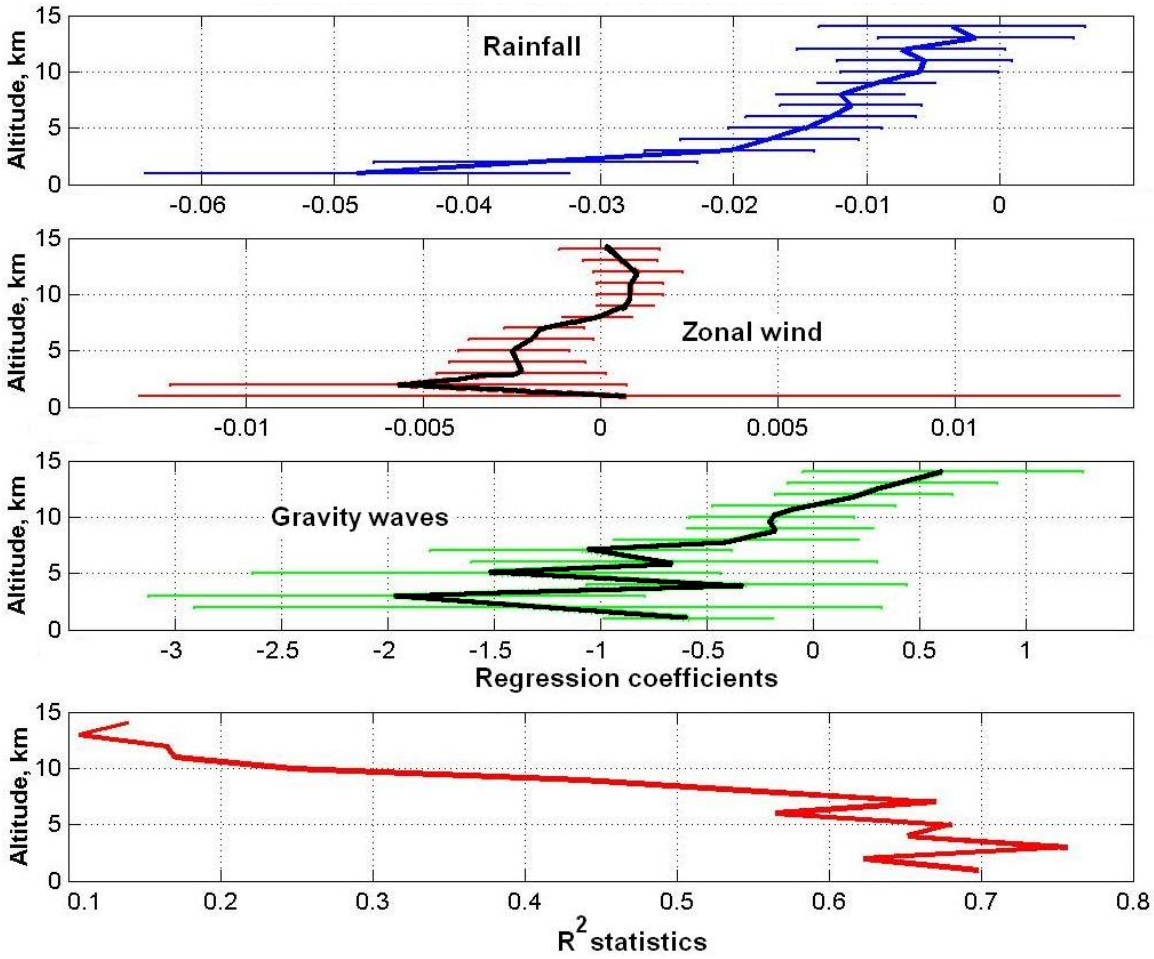

Figure 7.1 Altitude dependence of the regression coefficients and their 95% confidence intervals for the DQU profiler-measured vertical wind (rainfall rates are from raingauges). The lower graph shows the R^2 statistics.

At the upper plot in figure 7.1 (for the DQU) the precipitation regression coefficient is negative, same as for average plot in figure 7.2; that means precipitation results in negative bias of the vertical wind measurements. The magnitude of the coefficient is largest in the lower troposphere and decreases to almost zero at 14 km.

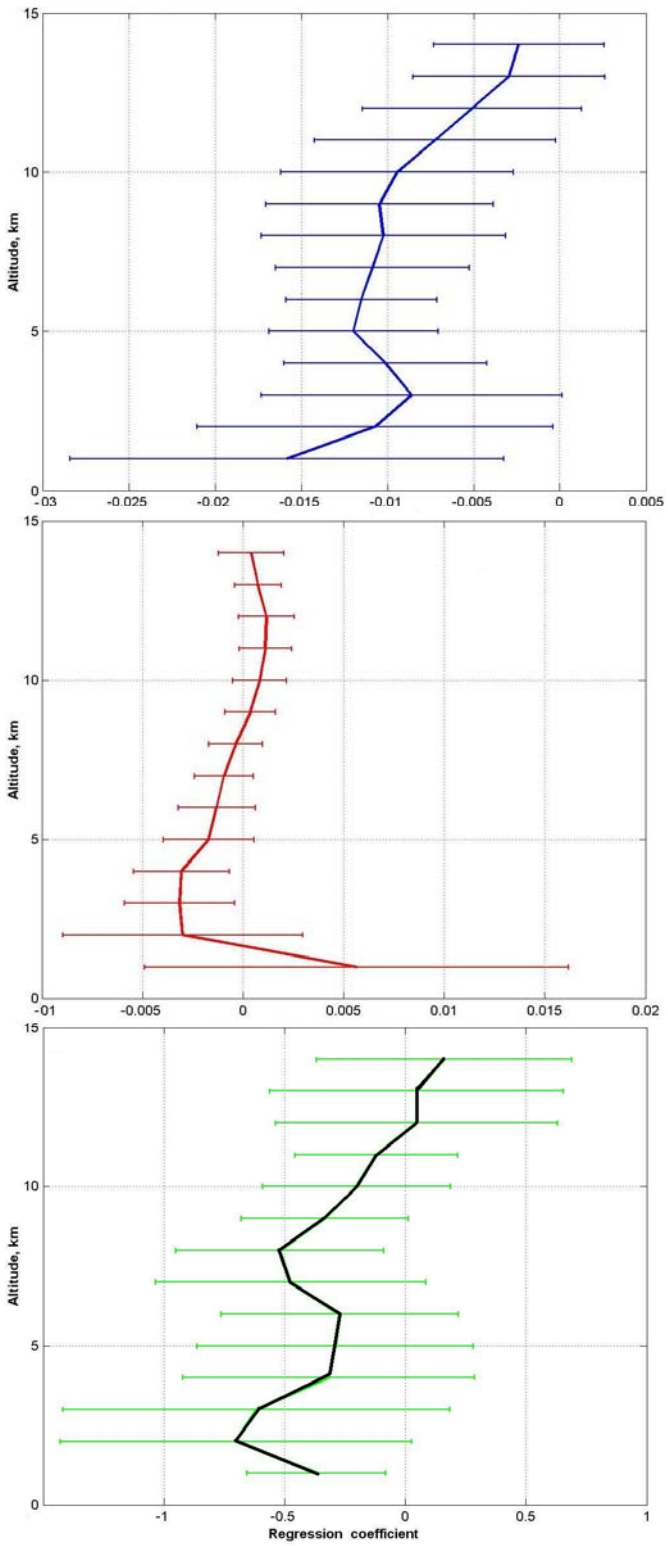

Figure 7.2 Altitude dependence of average regression coefficients. Upper plot is for rainfall; middle- for zonal wind and lower – for vertical component of the gravity wave energy. Rainfall rates are from reanalysis.

The average regression coefficient for the zonal wind in figure 7.2 is maximum (positive) at the lower altitudes, changing to smaller negative values at tropospheric heights, and is changing sign again in the stratosphere.

Large values in the lower troposphere and the significant variance between the profilers are probably the result of significantly different topography with, as a consequence, mountain waves being generated by the zonal flow and the phase of the wave vertical velocity changing sign.

The average regression coefficient for the gravity waves is variable, but negative most of the time for most of the locations, with an exception at altitudes of 12 km and up, where it becomes positive. Negative sign corresponds to the findings of Nastrom et al., (1994) and Nastrom and VanZandt (1996) that gravity waves introduce a negative bias in vertical wind measurements.

In order to validate the linearity of the precipitation effects on vertical wind bias and as a general diagnostics of the model we have checked the distribution of the residuals r :

$$r = w' - Xb, \tag{7.5}$$

and plotted the residuals versus corresponding values of the regressors (precipitation, zonal wind and gravity waves). Sample scatterplots for DQU profiler are presented in figure 7.3. Scatterplots for all profilers were assessed, and were found to be similar.

The main conclusion from this test is that residuals do not show any tendency with increasing regressor values, i.e. they are not correlated. Another conclusion is that no curvature effects were observed, and therefore the assumption of linearity of the vertical wind bias with respect to the regressors is valid. The residual errors for a strong

gravity wave episode (the right part of the lower plot in figure 7.3, with energies of 0.4 - 0.6 J/kg) do not differ significantly from the areas of the plot that correspond to low energies.

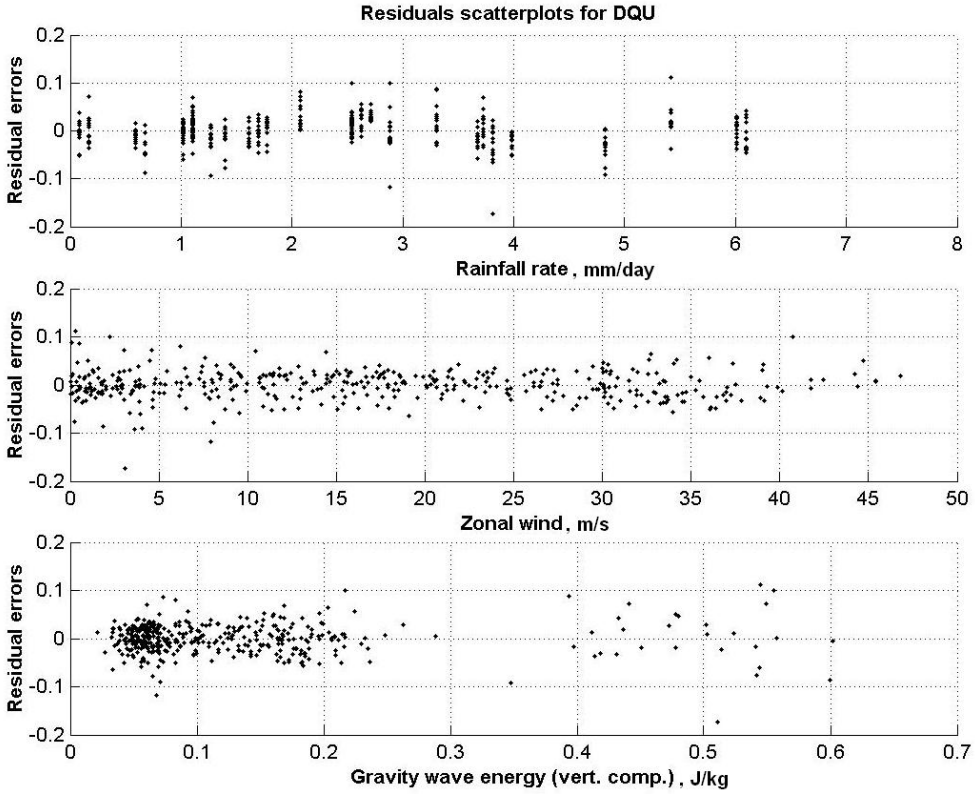

Figure 7.3 Scatterplot of regression residual errors for DQU versus regressors (rainfall rate, zonal wind and vertical component of gravity wave energy).

The discrete appearance of the upper plot in figure 7.3 (rainfall rates) is due to the nature of the rainfall data, that are reported in fractions of an inches and were then converted into millimeters per day.

7.2 Regression analysis of gravity wave sources

In chapter 5 we have analyzed the possible sources of generation of gravity waves using the correlations of gravity wave energy with precipitation rates and the vertical shear of the horizontal wind separately. It is of interest to see how joint effect of shear, rainfall and topography would represent the actual total gravity wave energy observed.

As in section 7.1, we have presented the total gravity wave energy as a linear combination of precipitation, zonal wind factored by topography variance and wind shear:

$$E_{\Sigma} = b_1 + b_2 P + b_3 (u \cdot \Delta_h) + b_4 u_{shear}, \qquad (7.6)$$

where E_{Σ} - total gravity wave energy at time t_i at some height h_j ; b_1 , b_2 , b_3 , b_4 – regression coefficients; P - precipitation rate for time t_i; u – zonal wind at time t_i at height h_j; u_{shear} - vertical shear of horizontal wind at time t_i at height h_j , and $\mathbf{\Delta_h}$ - estimates of topography variation as calculated in chapter 6.

In the expression (7.6) we have assumed a linear dependence between the regressors and the modeled parameters. Unlike in the previous case (the vertical wind bias model) the explicit expression of the dependence of gravity wave energy on convective activity is unknown and likely to be very complicated (to a larger extent for the precipitation as a proxy of convection). The same can be said about dependencies on wind shear and zonal wind. Multiple model experiments with different nonlinear (squared, square roots etc.) dependencies of, for example wave energy on zonal wind have shown the robustness of the results with higher variances of the regression coefficients compared to simple linear model. Therefore we have used the linear model

here. It should be kept in mind, though, that the question of how good this model is, is far from being answered and requires additional thorough treatment.

As in the previous section, we have calculated the regression coefficients for altitudes from 1 to 14 km in 1 km steps for each profiler site, using 36-month precipitation rate data from both the raingauges and reanalysis, profiler-measured zonal winds and wind shear as determined in chapter 3. In these calculations to represent E_Σ we have used the monthly averaged values of total gravity wave energy at the corresponding altitudes, as obtained in chapter 5.

The results of the linear multiple regression analysis are presented below. In figure 7.4 we present the altitude dependence of the regression coefficients for the WNF profiler, together with the R^2 statistics for this profiler.

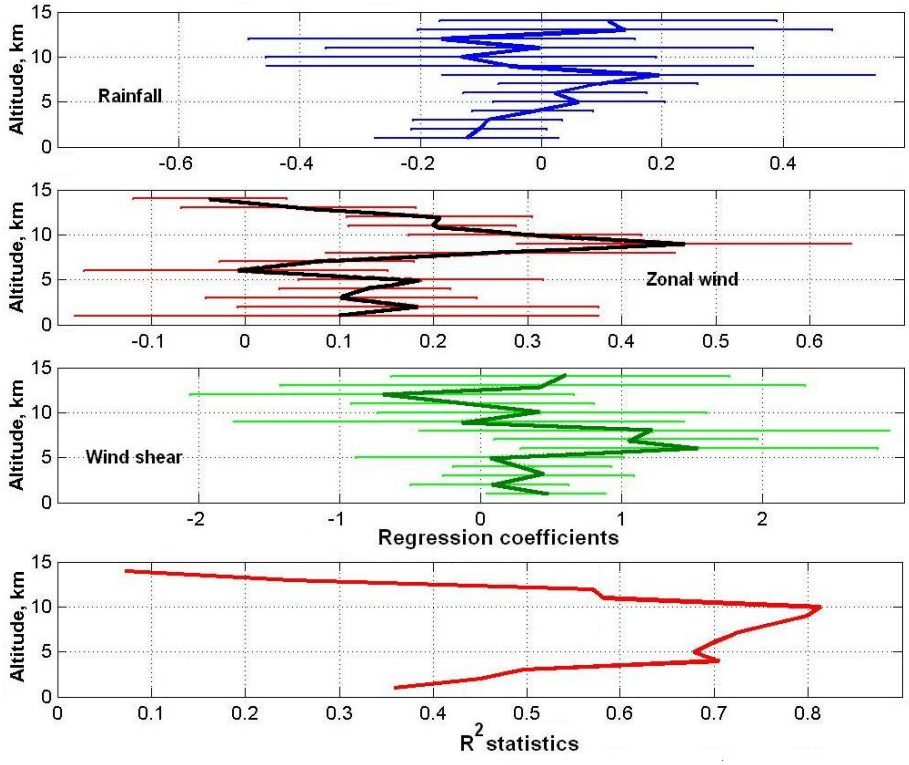

Figure 7.4 Altitude dependence of regression coefficients and their 95% confidence intervals for the WNF profiler total gravity wave energy (rainfall rates are from raingauge). The lower graph shows the R^2 statistics.

The amount of variance explained by the model is quite high, in the range of 70-80% at 5 to 10 km and decreasing both above and below these heights. Despite the high R^2 statistics, the regression coefficients have large confidence intervals, and are highly variable in altitude. Still, the regression coefficients for both zonal wind and shear could be identified as positive in almost all heights and having a maximum in the upper troposphere.

The average regression coefficients for the 25 profiler sites are shown in figure 7.5. For convenience in comparison in this plot the coefficients where scaled by the maximum value, so that each coefficient has a maximum value of one. The average regression coefficient for precipitation (upper plot in figure 7.5) is close to zero in the lower and midtroposphere and becomes negative in the upper troposphere, reaching a maximum at ~ 9 km. This result shows that convection (determined through precipitation as a proxy in this study) is not an important source of the total gravity wave energy. This could be explained if the waves launched by convection were one-dimensional, *w*-component waves. From chapter 5 we know that they represent an insignificant part of the total wave energy. The negative sign in this case is due to the fact that the development of convection requires low background winds, and therefore the precipitation regression coefficient would have opposite sign to the coefficient for shear. This could be verified by comparison with the lower plot in fig. 7.5 that shows the altitudinal dependence of the average regression coefficient for wind shear. Wind shear appears to be the most effective mechanism in influencing wave energy at the upper troposphere, with maximum at ~9 km. The regression coefficient for shear is positive almost everywhere, but with a variability that results in wide confidence intervals.

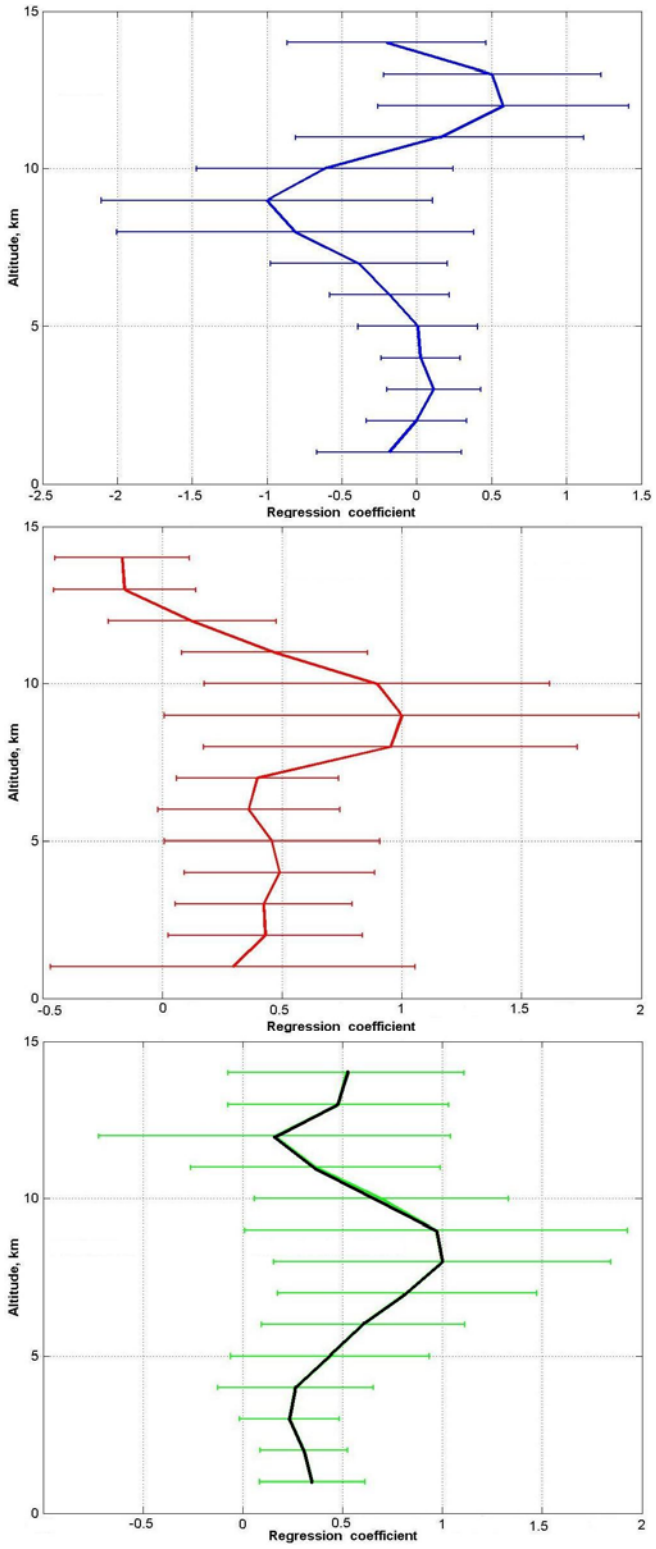

Figure 7.5 Altitude dependence of average regression coefficients for profiler-measured total gravity waves. Upper plot is for rainfall; middle- for zonal wind and lower – for horizontal wind shear. Rainfall rates are from reanalysis.

The average regression coefficient for the zonal wind (middle plot) is similar to the coefficient for shear, with a distinct maximum that extends from 8 to 10 km. It has a rather constant value of about half of the maximum in all of the lower and middle troposphere, that, in our opinion, reflects gravity wave generated by topography.

The R^2 statistics for all the locations (figure 7.6) showed that on average between 50 and 60% of the total gravity wave energy variance was explained by the model at the 4 - 10 km altitudes. Larger values, up to 85% were observed at almost every location, but within a narrow altitude range in the upper troposphere, with significant variations at other heights.

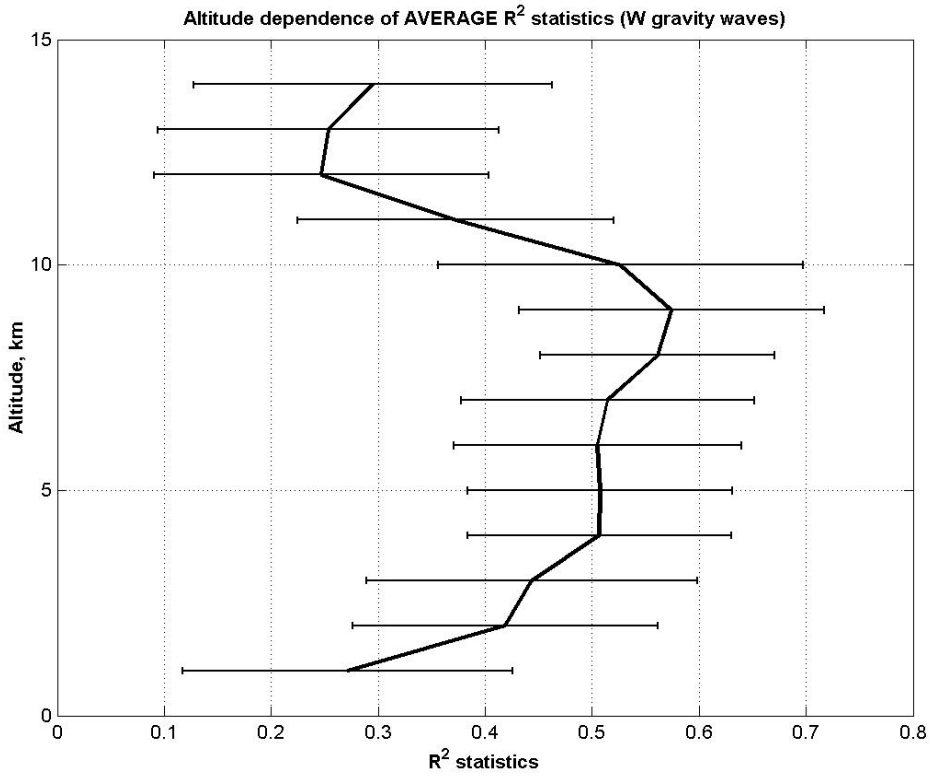

Figure 7.6 Average R^2 statistics of gravity wave regression model for 25 profiler locations.

An analysis of the residuals was performed for this model as in section 7.1, and produced similar results. As was mentioned above, the distribution of errors was found to be more uniform and the R^2 statistics more significant for the linear relationship given above in expression (7.6) than for the non-linear models for rainfall and zonal wind.

Because of the variability (low significance) of the regression coefficients found in this analysis we qualify these results as only preliminary and qualitative, rather than quantitative. Still, the profiles of the regression coefficients were found to be quite robust to small changes in the model, and therefore the inferences made about the altitudinal variations of the gravity wave sources could be important.

CHAPTER 8

DISCUSSION OF THE RESULTS AND CONCLUSIONS

8.1 Factors affecting wind measurements by NPN profilers

Horizontal winds

Despite the generally good agreement between the reanalysis zonal wind and profiler zonal wind measurements, five locations (BLR, MBW, NLG, SLA, WDL) were found to have noticeably lower correlations than most of the profilers, as can be seen in figure 3.3. Two of these locations have either very high topography variations (MBW, Δ_h ~144 m^2) or high rainfall rates (WDL). The BLR site is also located in moderately hilly terrain, and is characterized by the strongest low-level winds of all the profiler locations. The NLG and SLA lack extremes in topography or rainfall, but they both have higher than average gravity wave activity, which is also true for BLR, MBW and WDL. Average gravity wave activity (E_k) for these five locations was found to be higher (8.5±0.6 J/kg) than the average for all 25 stations in the mid-troposphere (7.3±0.9 J/kg), as shown in figure 5.12. This is a noticeable difference, considering the range of variations of the gravity wave energy at those altitudes for all profilers (between 5.3 and 9.6 J/kg). Comparison of figures 3.8 and 5.12 shows that high gravity wave activity has affected the performance of the horizontal wind measurements by the NPN profilers, but to a lesser extent than it has affected vertical wind measurements.

The vertical shear of the horizontal wind was also found to be indicative of the special conditions at the MBW site – high shear at this site most likely is associated with

extreme variations of topography and the highest elevation of this site in between all network profilers.

Vertical winds

The long-term average characteristics of the vertical winds, measured by the NPN profilers and presented in this study, have provided new information that can improve our interpretation of the profiler measurements.

The analysis of long-term average vertical profiles of vertical wind (figure 3.13 and appendix D) and comparison to similar profiles obtained by VHF radar, suggest that the precipitation-related bias present a serious problem for NPN profilers. McAfee et al., (1995), using 43-day measurements in late fall/winter have found that differences between VHF and UHF profilers are the largest below ~ 6 - 7 km. In this study the largest differences have been observed starting at 3 - 4 km and below. A closer look at the seasonal behavior of the vertical profiles provides an explanation for the discrepancy between our findings and those of McAfee. Winter and fall profiles in our data do have a larger negative bias starting from ~ 6 km and below, while in summer/spring the negative bias is smaller in magnitude and extends up only to 2-3 km from the ground. Therefore multi-seasonal averaging, as applied to our data, leads to an inference of lower altitudes at which VHF and UHF profiles differ significantly.

The influence of precipitation on vertical wind measurements by profilers, and the altitudes affected can be inferred from table 8.1, where we have grouped the 36-month average vertical velocities measured by 25 wind profilers, based on the amount of average annual precipitation at the measurement site. The precipitation bias (larger

negative velocities for high-rainfall sites) is visible at 1 and 2 km, and becomes negligible above 3 km.

Analysis of the experimental distributions of the frequency of occurrence of vertical wind velocities, and especially of skewness and asymmetric shape of these velocity distributions, have supplied the valuable information on finding a velocity threshold to separate the effect of the hydrometeors from the effect of gravity wave bias on the vertical wind measurements. Despite using a different method, the threshold values for hydrometeor fall velocities in our results (-0.25 m/s) were found to be close to thresholds obtained by Ralph et al. (1996): -0.28 m/s to -0.39 m/s.

Table 8.1. Average vertical velocities measured by wind profilers based on 36 month of data. The averages obtained for raingauge-defined high/low rainfall locations are given in brackets.

Locations	36-month average vertical velocity $\overline{w}$, m/s				
	At 1 km	At 2 km	At 3 km	At 4 km	At 9 km
All locations (25 sites)	-0.16±0.05	-0.11±0.02	-0.08±0.02	-0.08±0.02	-0.04±0.02
High-rainfall locations BLM, DQU, OKO, PAT,WNF	-0.23±0.18	-0.14±0.02	-0.1±0.01	-0.08±0.01	-0.04±0.002
Low-rainfall locations AZC, HVL, JTN, MBW, VCI (AZC,GDA,MBW,RWD, WDL)	-0.13±0.04 (-0.12±0.02)	-0.09±0.01 (-0.09±0.02)	-0.08 ±0.01 (-0.08±0.02)	-0.08±0.01 (-0.08±0.02)	-0.04±0.02 (-0.03±0.01)

A simple correction, based on this threshold, was applied to the profiler data. It has significantly improved the agreement between the profiler vertical winds and both the reanalysis and MM5 vertical winds. For reanalysis comparisons, from being negative (-0.4…-0.6), correlations have changed to positive, with correlation coefficients reaching up to 0.55 (SLA) as shown in figure 4.11. Still, even after correction, 8 stations had low

or negative correlations. The low correlations at three of the locations (BLR, CNW, and MBW) may be explained by the effects of strong gravity wave activity or topography, as these sites are characterized by high values of gravity wave energy and topography variance Δ_h. The reasons for low correlations at PAT, PRC, WNC, DQU, and BLM are not very clear, and might include reanalysis errors and local effects. We have noticed that these locations have a higher than average vertical component of gravity wave energy in the lower troposphere, bit not in the midtroposphere, where comparison with reanalysis took place. Additional studies are required to explain these results.

Overall, we speculate that there are three reasons that can be responsible for the observed profiler vs. reanalysis discrepancies, beside the precipitation bias.

First, the effects of terrain and terrain-related gravity waves could introduce both (a) specific local features of vertical velocity and (b) biases in the profiler measurements due to the reflectivity modification by waves as suggested by Worthington et al., (2001) and Nastrom and VanZandt (1996). The indirect proof of this possibility can be found in the dependence of the correlation coefficient of reanalysis (or MM5 model) vertical winds vs. profiler vertical winds on the topography variance Δ_h which is demonstrated in table 8.2. This table represents correlation coefficients from figure 4.11, grouped for the stations located in mountainous, hilly and flat terrain. In this table we observe a certain increase in correlation as the terrain (defined on the basis of the findings in chapter 6) changes from highly variable to very flat. This effect is observed in both the reanalysis and MM5 comparison.

Table 8.2. Grouped correlations of vertical velocities (Reanalysis versus profiler and MM5 vs. profiler) after rain correction at 5 km.

	Wind profilers grouped by location			
	All locations (25 sites)	Mountains (AZC, MBW)	Hilly terrain (BLR, CNW, DQU, GDA, HKL, JTN)	Flat terrain (HBR, LMN, PAT, SLA,WDL,WNF)
Correlation coefficient (Reanalysis vs. profiler at 5km)	0.18±0.2	0.08±0.2	0.16±0.1	0.35±0.1
Correlation coefficient (MM5 vs. profiler at 5km)	0.24±0.27	-0.1±0.4	0.2±0.26	0.32±0.2

Second, the approach that was used to correct the precipitation-induced bias utilizing a fixed vertical velocity threshold, could erroneously affect the areas of negative velocities which are introduced by individual gravity waves. The corresponding positive phase of the wave would therefore introduce a positive bias into long-term measurements. This is a definite drawback of the correction method used, which is difficult to eliminate in the absence of signal power data. Still some improvement could be made, for example precipitation correction procedures could be improved based on the use of altitude patterns of precipitation velocities (the precipitation fall velocity is typically increasing with decreasing altitude).

Third, we can not eliminate the possibility of poor performance of either certain profilers (due to undetected ground clutter, low transmitted power, etc.) or models at some locations or in some conditions.

The multiple linear regression analysis results do correspond well to the basic physics of the processes involved and to the mechanisms of vertical wind biases known from publications; at the same time some new and interesting details were found.

The effect of precipitation was found to decrease with increasing altitude (the upper plot in figure 7.2), but still be significant in the upper troposphere. The regression coefficients for precipitation and gravity waves were to some degree negatively correlated with each other, reflecting the fact that gravity waves can be generated by convection. Therefore, in addition to the direct precipitation effect (introduced by negative droplet velocity) which was found to be important below 3-4 km, a secondary bias may appear, through generation of gravity waves. These waves, in term, could be affecting vertical wind measurements via mechanism proposed by Nastrom and VanZandt (1994). Therefore it is plausible that the effect of precipitation on the vertical wind at altitudes above 5 km, found in our regression analysis, is a secondary effect of the convection-generated gravity waves.

In fact, all the variables used for regression analysis (regressors) were not completely independent, i.e. strong winds would suppress the convection, convection could be a source of the gravity waves, etc. This might in part explain relatively low percentage of the total variance explained by the model.

The regression coefficients for the zonal wind were found to be larger and more variable in the lower troposphere, which is understood since surface topography vary strongly between the profiler locations, and stronger winds would result in stronger mountain waves produced in the lower troposphere. The positive sign of this bias of the vertical wind is in agreement with the findings of Worthington et al., (2001) who suggested that the traditional location of wind profilers in valleys result in a steady pattern of mountain wave above the radars. The change of sign of the regression

coefficient for the zonal wind at ~3 km and again at ~ 10 km observed in our data is also in agreement with the model of Worthington et al., (2001).

Another interesting result of the regression analysis is the zero value of the zonal wind regression coefficient at the level of maximum horizontal winds, which proves that no significant antenna-pointing errors were present.

Analysis of the regression coefficient for the gravity waves suggested a negative bias of the vertical wind due to the gravity waves at altitudes from the ground up to ~12 km. The value of the regression coefficient is within 0.4 - 0.7 with two local maxima at 2 and 8 km. This could be a manifestation of two mechanisms of gravity wave generation – topographic (in the lower troposphere) and effects of the jet stream and wind shear in the upper troposphere.

Nastrom and VanZandt's (1994) formula (equation 7.3, chapter 7) estimates the vertical wind bias due to gravity waves using the gravity wave amplitude $\hat{w}$, vertical wavenumber *m* and frequency ν. Based on a vertical typical wavelength of 3000 m, a period of 2000 s and using the expression $\hat{w} = \sqrt{2\sigma_w^2}$ for dependence of wave amplitude $\hat{w}$ on the energy of the vertical wave component σ_w^2, Nastrom and VanZandt estimated the typical bias for the Flatland VHF profiler to be about -4.7 cm/s. According to Nastrom and VanZandt's calculations, the coefficient $\frac{1}{2}\frac{m}{\nu}$ in the equation (7.3) for the gravity-wave induced bias is equal to -0.68 for all measurements with σ_w^2 <0.13 J/kg at 4.25 km altitude, and decreases upward.

In this study the mean regression coefficient for gravity wave energy (which is equal to $\frac{1}{2}\frac{m}{\nu}$ in Nastrom and VanZandt's formulation) was found to vary from -0.3 to -0.7 at different altitudes (the lower plot in figure 7.2). The σ_w^2 in our data was larger than that for the VHF profiler used by Nastrom and VanZandt by a factor of 2, as can be seen e.g. in the lower plot of figure 7.3. Also, Flatland is located on very flat terrain, while the regression coefficient in our study represents an average for the 25 very different locations including ones in the mountains. Considering the mentioned differences between the two studies, similar results for $\frac{1}{2}\frac{m}{\nu}$ (gravity wave regression coefficient) validate one component of our regression model.

There is an interesting possibility for estimating the distribution of wavelengths and periods of gravity waves using (7.3), provided that estimates of gravity wave regression coefficients are available. Similarly, the vertical anisotropy of the gravity waves (the ratio of waves with upward and downward directions of energy propagation, after Nastrom and VanZandt, 1994) could be estimated over the range of altitudes.

8.2 Gravity wave morphology and sources

In this study we have used two approaches to determine the gravity wave morphology. The variance of the three orthogonal components of the wind vector was used in the first part of chapter 5 to estimate the components of gravity wave energy. The values of the variances of the zonal and meridional components of the wind, reported by Hansen et al., (2001) for the White Sands VHF profiler (10 - 30 m^2/s^2) are similar to

ours, e.g. presented in figure 5.1. The seasonal structure is also very similar, with broad maxima that stretch from late fall till the end of the spring.

The vertical wind variance data (corresponding to the vertical component of the gravity wave kinetic energy) in our study have similar magnitudes to those of Hansen et al., but with significantly different time structure – less pronounced seasonal changes, and presence of summer maxima for some locations. This is most likely an effect of precipitation contamination of the UHF profiler data, which is significantly lower at VHF. Therefore the results of the vertical wind variance presented here, should be used with caution.

Our second approach, that utilizes the spectral analysis technique, allowed the separation of high-, low- and medium frequency gravity waves. The filtering and smoothing properties of this technique, together with the selection of the data (the long uninterrupted data segments needed for spectral analysis) have eliminated part of the data contamination problems, and produced more viable results. For example, the mid-tropospheric vertical wind variance (figure 5.2) did not show any enhancement at the MBW location (highly mountainous and therefore active in topographic wave generation), while spectral analysis clearly identified high activity (figure 5.4) in both the lower and upper troposphere.

We have found that the energy of the low-frequency component of the gravity waves is significantly larger than the energy at mid- and high-frequencies. This result contradicts the findings of Hansen et al., (2001), who obtained comparable energies for 6 min-2 hours and 2-21 hours periods. Our results are in a better agreement with accepted

theoretical and experimental results (e.g. Vincent et al., 1997) as to how the energy is distributed within the spectrum of the gravity waves and how it is generated.

Using the sum of all three frequency components we have obtained temporal and altitudinal distributions of total gravity wave energy. Wang and Geller (2003) (to our knowledge one of the most extensive gravity wave climatology studies published) have used the *vertical* variations of radiosounding wind data (versus *temporal* variations in our study) and obtained climatology of the gravity wave energy over North America. The essence of their climatology for the troposphere is presented in figure 8.1.

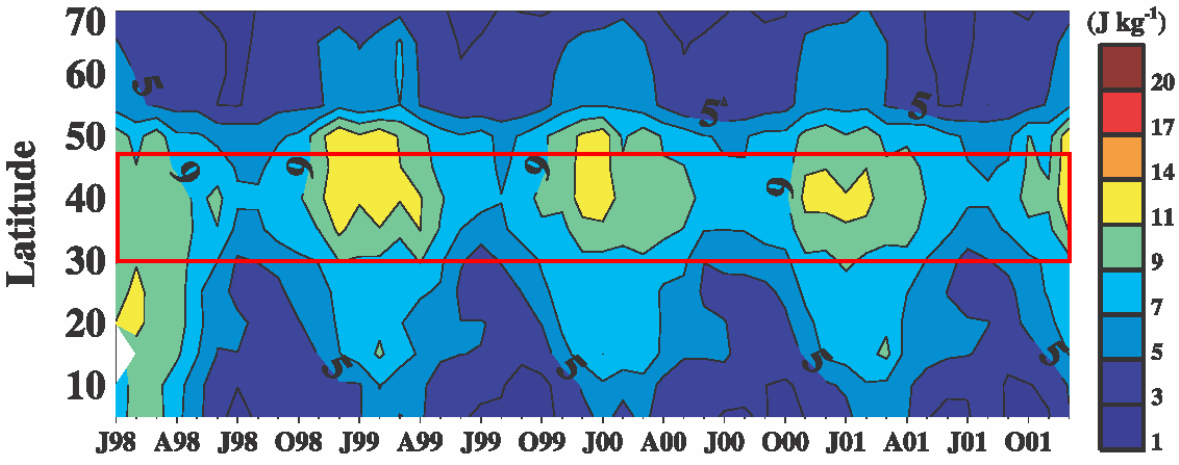

Figure 8.1. Total energy density in the troposphere. Adapted from Wang and Geller (2003); the troposphere defined as extending from 2 - 8.9 km. The latitudes shown in figures 5.5-5.7 are inside of the red rectangle.

The NPN (this study) covers only that part of the Wang and Geller's region inside the red rectangle in figure 8.1.

The observed seasonal and zonal structure of the total gravity wave energy in the troposphere obtained in this study (figures 5.5-5.7) generally coincides with the findings of Wang and Geller (2003). The maxima of mid-tropospheric gravity wave energy are

observed in late fall - early spring. The magnitude of gravity wave energy increases poleward within the region covered by the NPN. The longitudinal structure is also similar, with the Rocky Mountains identified as a significant source of midtropospheric gravity waves. These results suggest the equivalence of both methods (time vs. altitude domain analysis) in the troposphere/lower stratosphere.

At the same time the magnitude of the total gravity wave energy in our study is almost a factor of 2 larger in the upper troposphere than one presented by Wang and Geller (figure 7.1). Our analysis of the gravity wave energy behavior in the altitude domain suggests that the maximum is located at ~ 8 - 10 km, at the altitude of the tropospheric jet stream, which also indicates that the jet is the most significant source. Careful consideration of the averaging procedures and altitude domains used by Wang and Geller revealed that in their study the tropospheric gravity wave energies were averaged over 2 - 8.9 km altitude range. Therefore the area with the maximum gravity wave energy, found in our results at ~ 8 - 10 km, was partially excluded from consideration by Wang and Geller, due to their choice of altitudes averaged. The time-altitude fields presented in chapter 5 describe the structure of the gravity waves in better details, and, most importantly, identify the altitude of the gravity wave energy maxima.

Our results are also close to lidar-derived gravity wave energy data presented by Hertzog et al., (2001), who reported mean energies in the lower stratosphere to be about 10 J/kg. Also, at the highest altitudes of the profiler coverage (lower stratosphere) we observe much less developed seasonal structure than in the troposphere. This is also in agreement with Hertzog et al.

An interesting feature found in the gravity wave energy behavior in the upper troposphere is that the seasonal winter enhancement of gravity wave energy propagates downward from the tropopause height, supporting the suggestion that upper tropospheric winds are the dominant source of gravity waves at 30 - 40 °N.

Gravity wave generation sources.

Analysis of the correlation of the separate components and frequencies of the gravity wave energy versus precipitation rates and horizontal wind shear has revealed some important details about how and where waves are generated. Multiple regression analysis of the wave sources confirmed the results of section 5.5 that zonal wind and wind shear are the most important sources of gravity wave total energy in the midlatitudes, a finding that is similar to the results of Murayama et al., (1994) for gravity waves above the MU radar in Japan.

Zonal wind and vertical shear of horizontal wind were found to be most important in the upper and middle troposphere, from ~ 4 to 10 km. In this height region the regression results agree well with the correlations presented in figure 5.16, where correlations are >0.6 for 4 - 9 km. As was mentioned before, the regressors (independent variables) representing the zonal wind and wind shear may be correlated, which to some extent may bias the results.

The results for precipitation-related regression coefficients were somewhat surprising. It was found that precipitation and therefore convection does not have any significant effect on the total gravity wave energy. To the contrary, the coefficients were found to be negative for most of the altitudes. The explanation of this fact, offered in

section 7.2 is purely speculative. Taking into account the high variance of the results, additional study will be required to explain these findings.

Despite the simplified approach in formulating the regression model, and the wide confidence intervals of the results, we were able to predict 50 to 60% of the gravity wave variance on average for the altitudes from 4 to 11 km, with some locations showing even better results.

Topography was found to be an important source of midtropospheric waves, especially those of medium and high frequency. Similarly, based on the correlation analysis in section 5.6, precipitation (proxy for convection) was found to explain a significant part of the gravity wave kinetic energy associated with vertical component at all frequencies. Despite the fact that the vertical component, same as the medium- and high-frequency components, contribute less to the total gravity wave energy than low-frequency or horizontal components, our findings about sources of those waves are important because the vertical oscillations of high frequency affect the wind measurements by profilers the most.

8.3 Conclusions and suggestions for future work

In this work, we have presented long-term measurements of winds over central USA made by the NOAA network of UHF wind profilers. For the first time, altitude and time characteristics of the vertical wind fields have been analyzed based on data obtained by identical wind profilers at multiple locations.

Based on the long-term statistics of the vertical wind velocities we have determined a threshold for identifying and correcting the precipitation-contaminated data in vertical wind measurements by UHF profilers. Comparison of corrected profiler data with vertical winds from reanalysis (on a time scale of months and years) and from the MM5 model (on a timescale of days and weeks) showed a significantly improved agreement, versus uncorrected data. The comparison also demonstrated that a lot still remains to be done in developing and implementing a better algorithm for removal of precipitation-affected data to get unbiased estimates of synoptic-scale vertical motions.

The use of the presented velocity threshold for rain-removal could be very beneficial and lead to increased data quality, if imbedded into the profiler signal processing software at the NPN sites (similarly to the bird-correction algorithms already implemented). However, such an edited data should be flagged and original data preserved, so that subsequently developed precipitation-removal algorithms could be applied in future. In order to improve the detection and analysis of precipitation-affected data, raingauges should be installed at each profiler site. The raingauge precipitation data can be reported and archived using the same (already available) communication network as used to submit profiler's data.

The height range, affected by the direct influence of precipitation was found to be limited to the lowest 3 km of the troposphere. In addition, a secondary precipitation effect, due to convection-generated gravity waves, was identified by regression analysis. This second area extends up into the troposphere and lower stratosphere. The differentiation between the direct (by the rainfall velocities) and indirect (through gravity waves generated by convection) precipitation effects on the vertical wind measurements

is an interesting topic that needs to be addressed in more depth. Perhaps, an additional proxy for convective activity needs to be used, in addition to better precipitation data in the immediate vicinity of the profilers.

The inferences made in this work, that the horizontal wind measurements by UHF wind profilers are affected by gravity waves, should be used in data assimilation algorithms of forecast models that use the NPN data as a part of model initialization data. If the significance (weight) of profiler's horizontal wind measurements in data assimilation procedures is lowered for the cases when profiler data are biased by gravity waves, the operational weather forecasts can be improved.

For the first time the climatology of the gravity waves above the central USA has been obtained using a network of wind-profiling radars. We have presented gravity waves with high altitude resolution, and, most importantly, separation of the total energy by periods (6 min-1 hour, 1-3 hours, 3-12 hours) and spatial components (vertical and 2 horizontal). While comparable to previous results in the main features of the gravity wave energy field (seasonal behavior and zonal/meridional distribution), the new results identified energy maxima with values twice as large as in the climatology presented by Wang and Geller (2003).

This is an important result, as gravity wave parameterization schemes for GCMs that are based on the gravity wave energy data at the tropopause level can now be updated according to the real distribution of the gravity wave energy. This correction would lead to better estimates of gravity wave effects on the mean flow in the middle and upper atmosphere, and therefore improve the performance of the models in the upper atmosphere.

To extend the results of this study to other types of parameterizations, gravity wave spectral characteristics need to be obtained, which could easily be done in future, as the spectral analysis is already a part of the gravity wave energy estimation technique used here.

An interesting modification of this work would be to apply the methodology of Wang and Geller (2003), i.e. to look at the wind oscillations in altitude using individual profiles, which would allow estimating the vertical wavelength of the waves. In addition, information about wave propagation direction could be inferred by analyzing the rotation of the velocity perturbation vector with height (hodograph analysis).

Another improvement could result if the possible leakage of synoptic scale energy into the low-frequency gravity wave region is quantified and taken into account. To do this, spatial filtering of the horizontal oscillations with synoptic-scale wavelength should be performed, utilizing the spatial distribution of the profilers in the network.

The method for quantitative estimation of topography variations around the measurement sites, developed in this work, resulted in useful findings about topographic sources of the gravity waves. This method can also be applied to analyze various kinds of geophysical measurements that might be affected by terrain variations around the measurement sites. For more general use, the terrain classification suggested in chapter 6 should be updated and calculations with a larger number of sites for statistically significant cluster analysis should be performed.

APPENDIX A. Description of the NPN wind profiling radars

The NOAA Profiler Network was first deployed in 1990-1992 and has in continuous operation since. The original network consisted of 31 profiler sites located in the central United States and one site in Alaska. Since January of 2000, there are 32 profilers (404 MHz) in the central United States and three profilers (449 MHz) in Alaska. Not all of them were operational at the time of the study (www.profiler.noaa.gov/npn/aboutNpnProfilers.jsp).

The typical NPN profiler operates at 404.37 MHz (wavelength of ≈74 cm), and consist of solid-state transmitting system, antenna system and receiving/processing system.

Transmitter has a peak power 6 kW, and radiates a pulse of 3.3μs (low mode) or 20μs (high mode). Two modes are used to increase the signal-to-noise ratio at high altitudes. In a low-mode (0.5-9.25 km above ground level) the sampling is performed every 1.67 μs, yielding height resolution of 250 m. In a high-mode (7.5 to 16.25 km) the sampling is performed at the same rate and data are reported at 250 m step, while the actual resolution is ~ 900 m due to the signal coding and longer pulse length and therefore the data at 250 m samples represent the average over the larger vertical interval. In the overlap region (7.5 to 9.25 km) usually the data from a high-mode are reported, unless they do not pass a quality control. In this case the low-mode data will be used.

The antenna system is made of by two coaxial-collinear phased arrays (grids), arranged at 90-degree angle to each other to provide two orthogonal off-vertical beams at 16.3° zenith angle in North and East direction. The half-power bandwidth of the antenna

beam is 4.1° (Ralph et al., 1995a). The area of the antenna field is ~ 40x40 feet. Each grid has 20 rows of coaxial elements, fed by power dividers through a fixed-length radio frequency cables providing necessary phase shift. Antenna beam steering between three beams is performed electronically, by switching between the transmitting grids.

Receiving system is performing an amplification, sampling and digitizing and 128-point Fast Fourier Transform of the signal. Then signal spectra are processed to obtain an estimate of radial velocities corresponding to a current beam position.

The operation of the profilers is completely automated, and does not require a human presence except for periodic maintenance or repairs.

The data from individual wind profilers is submitted to the Profiler Control Center via satellite link (hourly data) or a landline (six-minute data). The Profiler Control Center is located in Boulder, CO. The computer hub at the Center performs the consensus averaging of the six-minute data, quality control and provides the data for open use over the Internet. Also, the data are provided to the National Weather Service Telecommunications Gateway.

APPENDIX B. Sample frequency of occurrence of the vertical wind velocities for 36-month measurement period for boundary layer, mid- and upper troposphere.

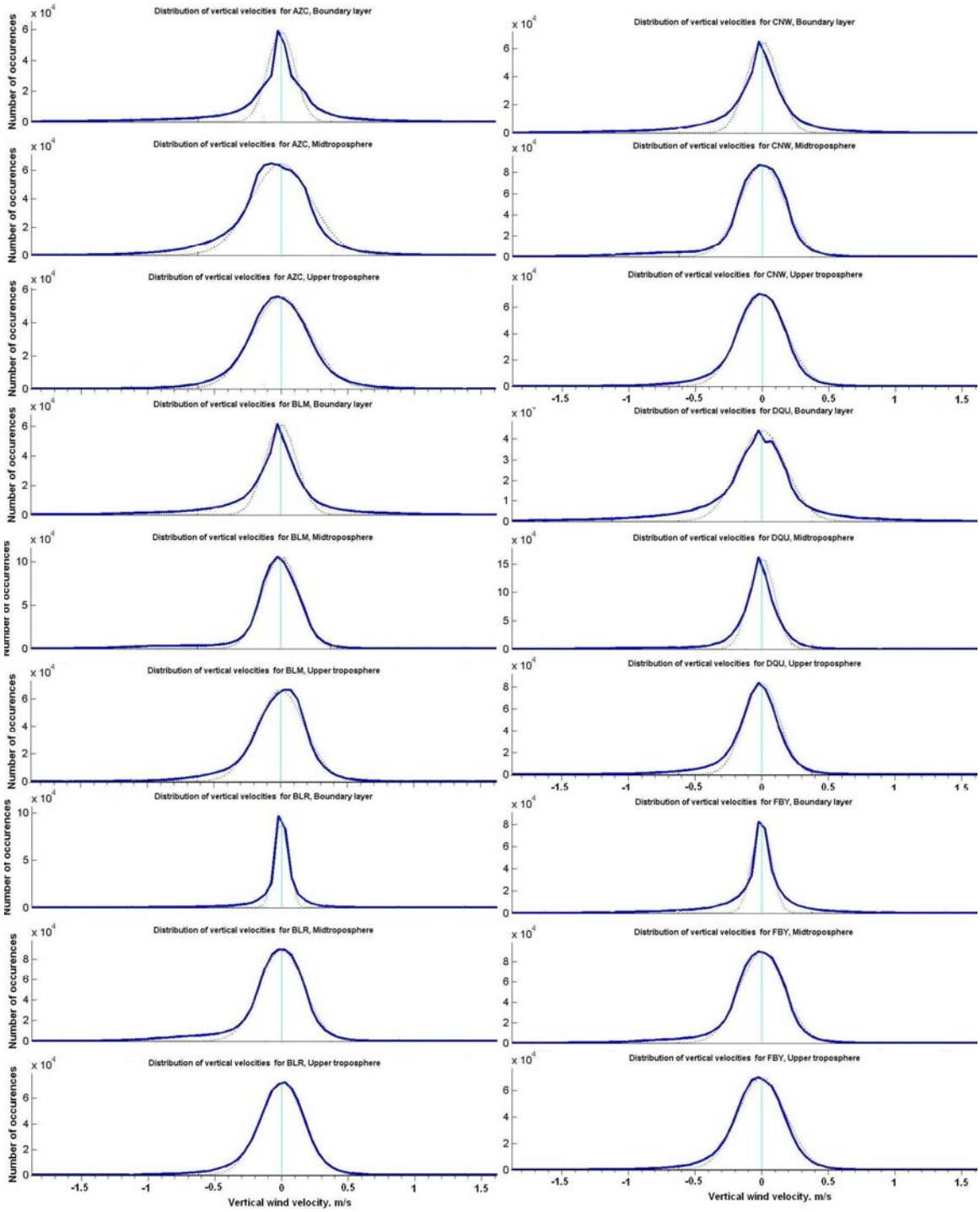

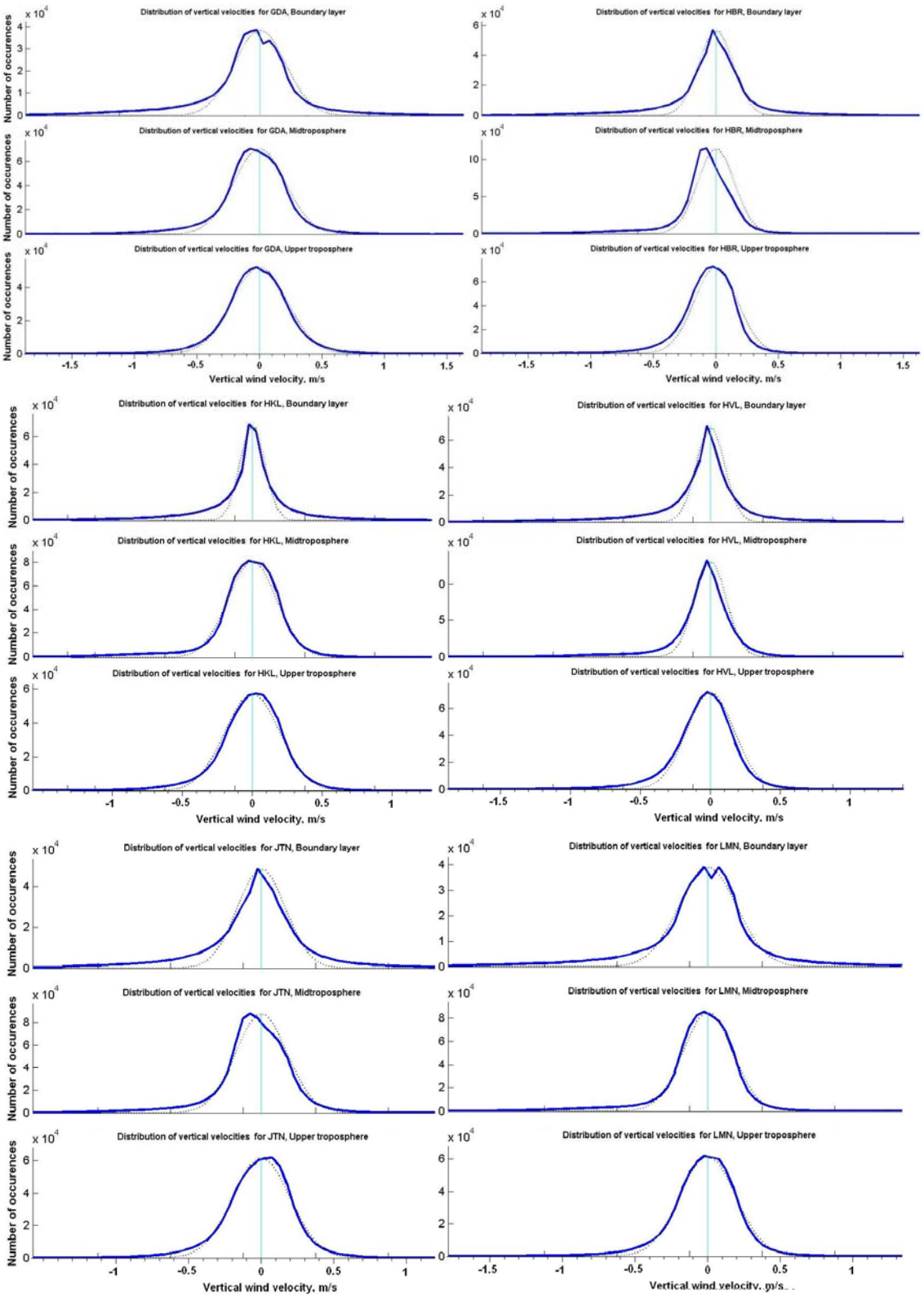
Distribution of vertical velocities for GDA, Boundary layer
Distribution of vertical velocities for HBR, Boundary layer
Distribution of vertical velocities for GDA, Midtroposphere
Distribution of vertical velocities for HBR, Midtroposphere
Distribution of vertical velocities for GDA, Upper troposphere
Distribution of vertical velocities for HBR, Upper troposphere
Distribution of vertical velocities for HKL, Boundary layer
Distribution of vertical velocities for HVL, Boundary layer
Distribution of vertical velocities for HKL, Midtroposphere
Distribution of vertical velocities for HVL, Midtroposphere
Distribution of vertical velocities for HKL, Upper troposphere
Distribution of vertical velocities for HVL, Upper troposphere
Distribution of vertical velocities for JTN, Boundary layer
Distribution of vertical velocities for LMN, Boundary layer
Distribution of vertical velocities for JTN, Midtroposphere
Distribution of vertical velocities for LMN, Midtroposphere
Distribution of vertical velocities for JTN, Upper troposphere
Distribution of vertical velocities for LMN, Upper troposphere
Number of occurences
x 10^4
Vertical wind velocity, m/s

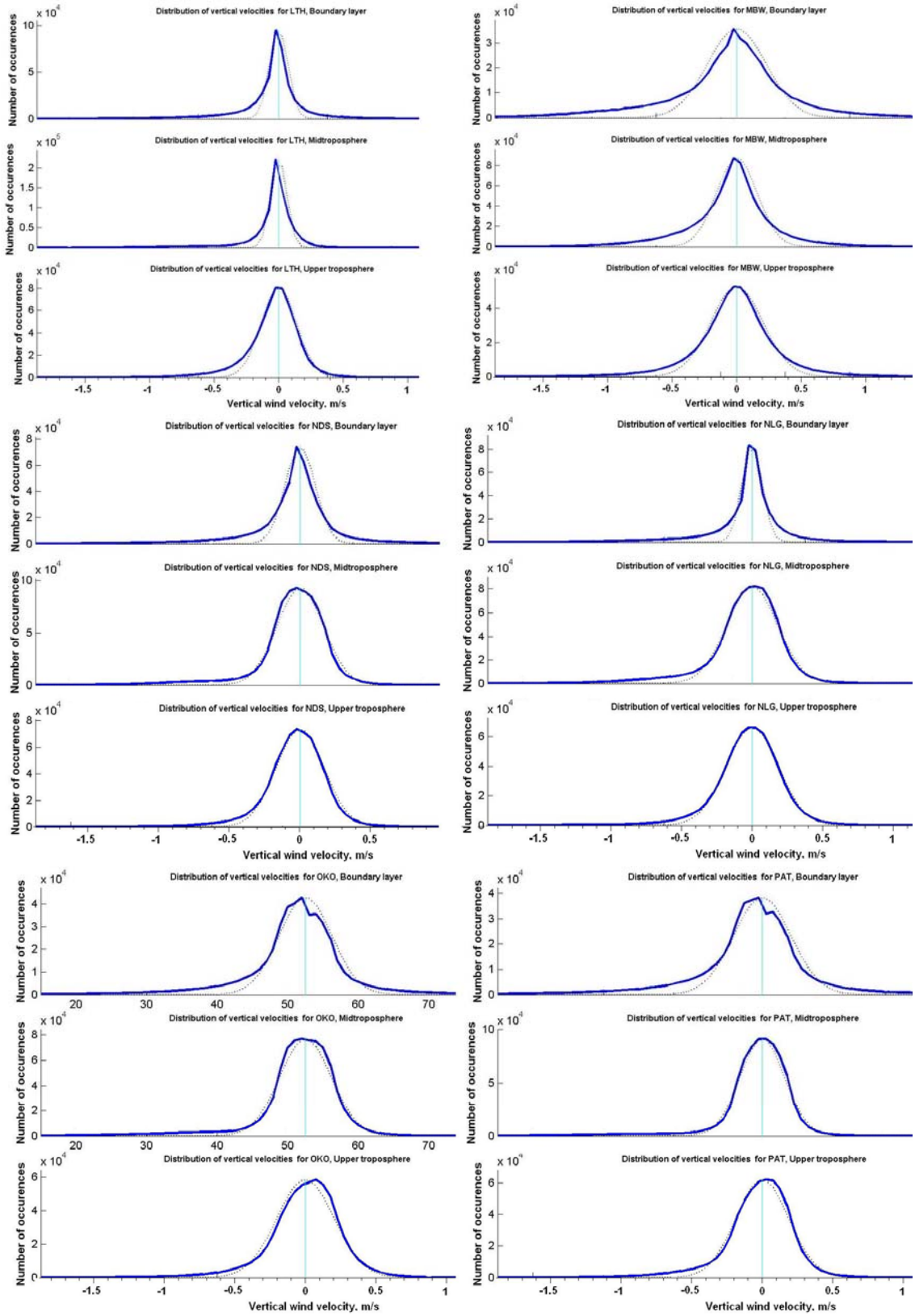
Distribution of vertical velocities for LTH, Boundary layer
Distribution of vertical velocities for MBW, Boundary layer
Distribution of vertical velocities for LTH, Midtroposphere
Distribution of vertical velocities for MBW, Midtroposphere
Distribution of vertical velocities for LTH, Upper troposphere
Distribution of vertical velocities for MBW, Upper troposphere
Distribution of vertical velocities for NDS, Boundary layer
Distribution of vertical velocities for NLG, Boundary layer
Distribution of vertical velocities for NDS, Midtroposphere
Distribution of vertical velocities for NLG, Midtroposphere
Distribution of vertical velocities for NDS, Upper troposphere
Distribution of vertical velocities for NLG, Upper troposphere
Distribution of vertical velocities for OKO, Boundary layer
Distribution of vertical velocities for PAT, Boundary layer
Distribution of vertical velocities for OKO, Midtroposphere
Distribution of vertical velocities for PAT, Midtroposphere
Distribution of vertical velocities for OKO, Upper troposphere
Distribution of vertical velocities for PAT, Upper troposphere
Number of occurences
Vertical wind velocity, m/s

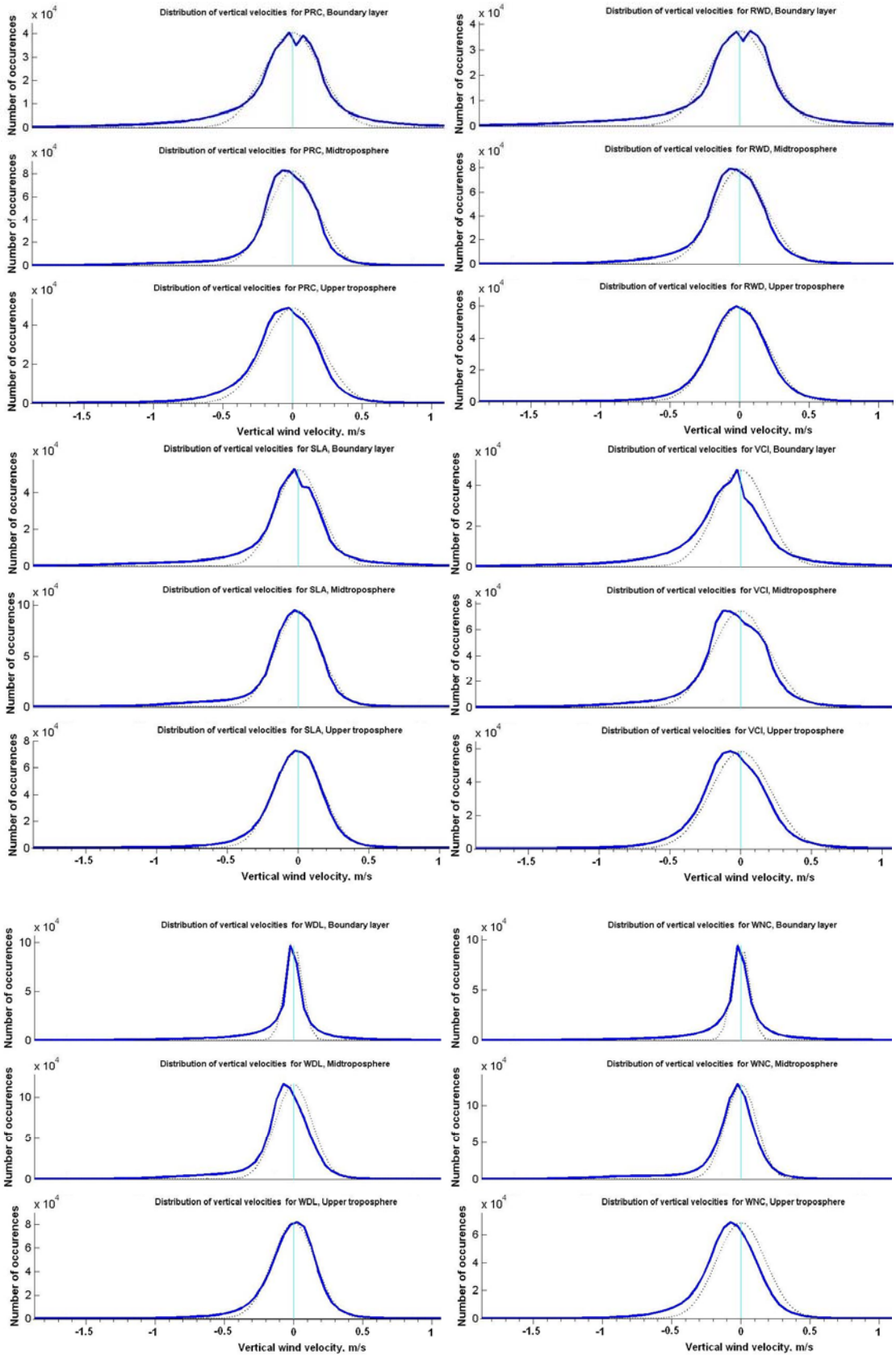
Distribution of vertical velocities for PRC, Boundary layer
Distribution of vertical velocities for RWD, Boundary layer
Distribution of vertical velocities for PRC, Midtroposphere
Distribution of vertical velocities for RWD, Midtroposphere
Distribution of vertical velocities for PRC, Upper troposphere
Distribution of vertical velocities for RWD, Upper troposphere
Distribution of vertical velocities for SLA, Boundary layer
Distribution of vertical velocities for VCI, Boundary layer
Distribution of vertical velocities for SLA, Midtroposphere
Distribution of vertical velocities for VCI, Midtroposphere
Distribution of vertical velocities for SLA, Upper troposphere
Distribution of vertical velocities for VCI, Upper troposphere
Distribution of vertical velocities for WDL, Boundary layer
Distribution of vertical velocities for WNC, Boundary layer
Distribution of vertical velocities for WDL, Midtroposphere
Distribution of vertical velocities for WNC, Midtroposphere
Distribution of vertical velocities for WDL, Upper troposphere
Distribution of vertical velocities for WNC, Upper troposphere
Number of occurences
x 10^4
Vertical wind velocity. m/s

APPENDIX C. Time-altitude plots of monthly mean vertical velocities measured by NPN wind profilers.

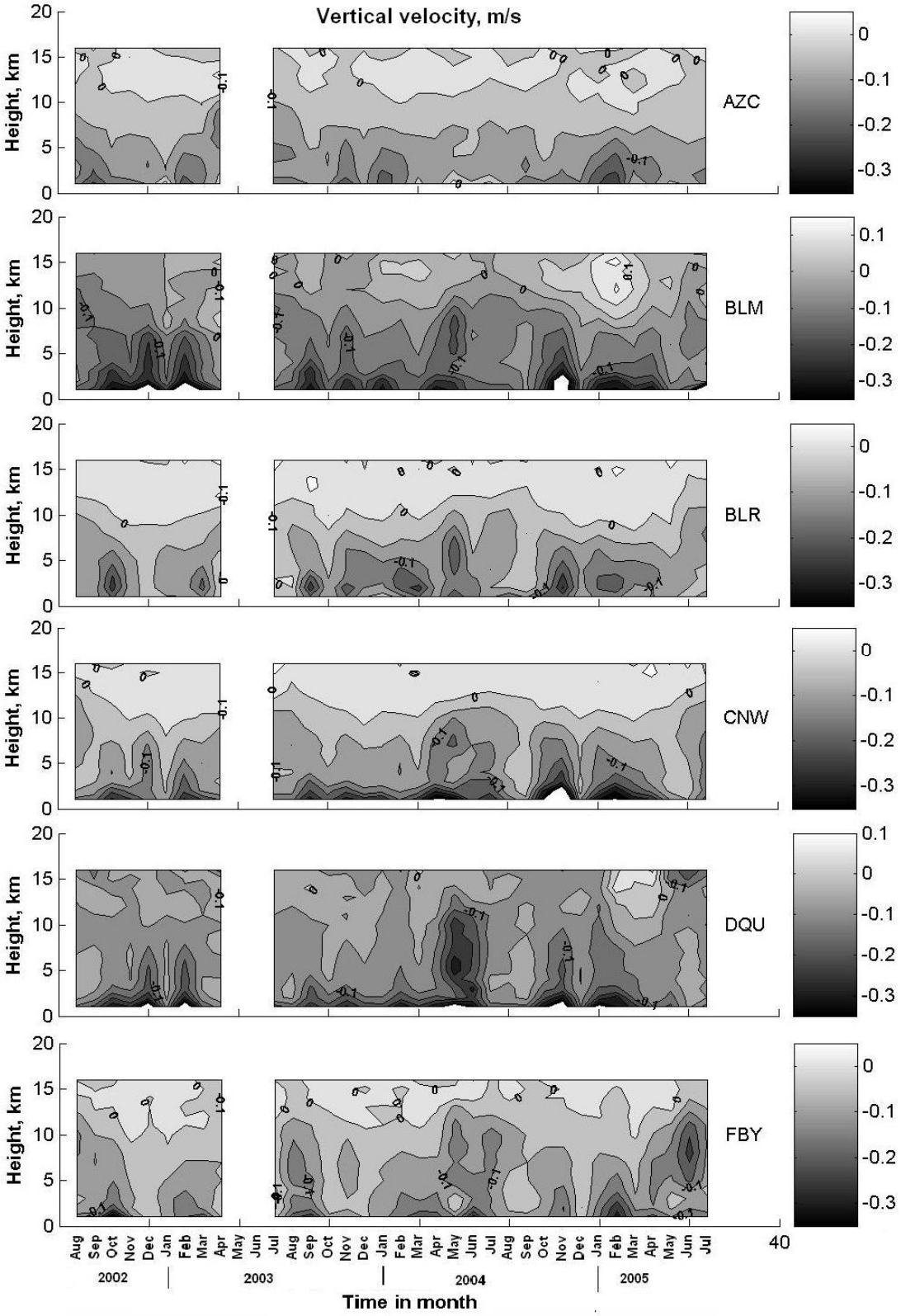

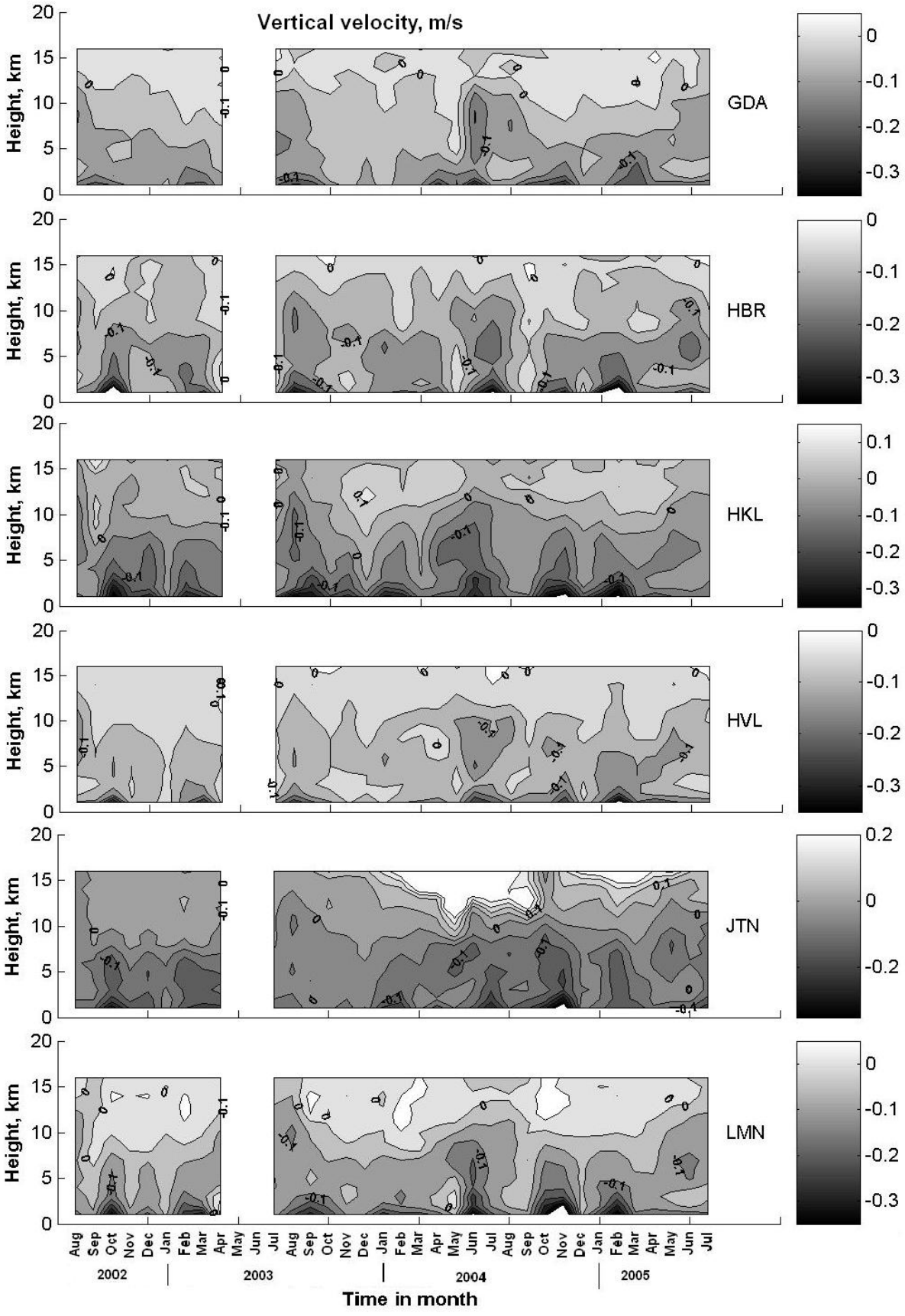
Vertical velocity, m/s
Height, km
GDA
HBR
HKL
HVL
JTN
LMN
Aug Sep Oct Nov Dec Jan Feb Mar Apr May Jun Jul Aug Sep Oct Nov Dec Jan Feb Mar Apr May Jun Jul Aug Sep Oct Nov Dec Jan Feb Mar Apr May Jun Jul
2002
2003
2004
2005
Time in month

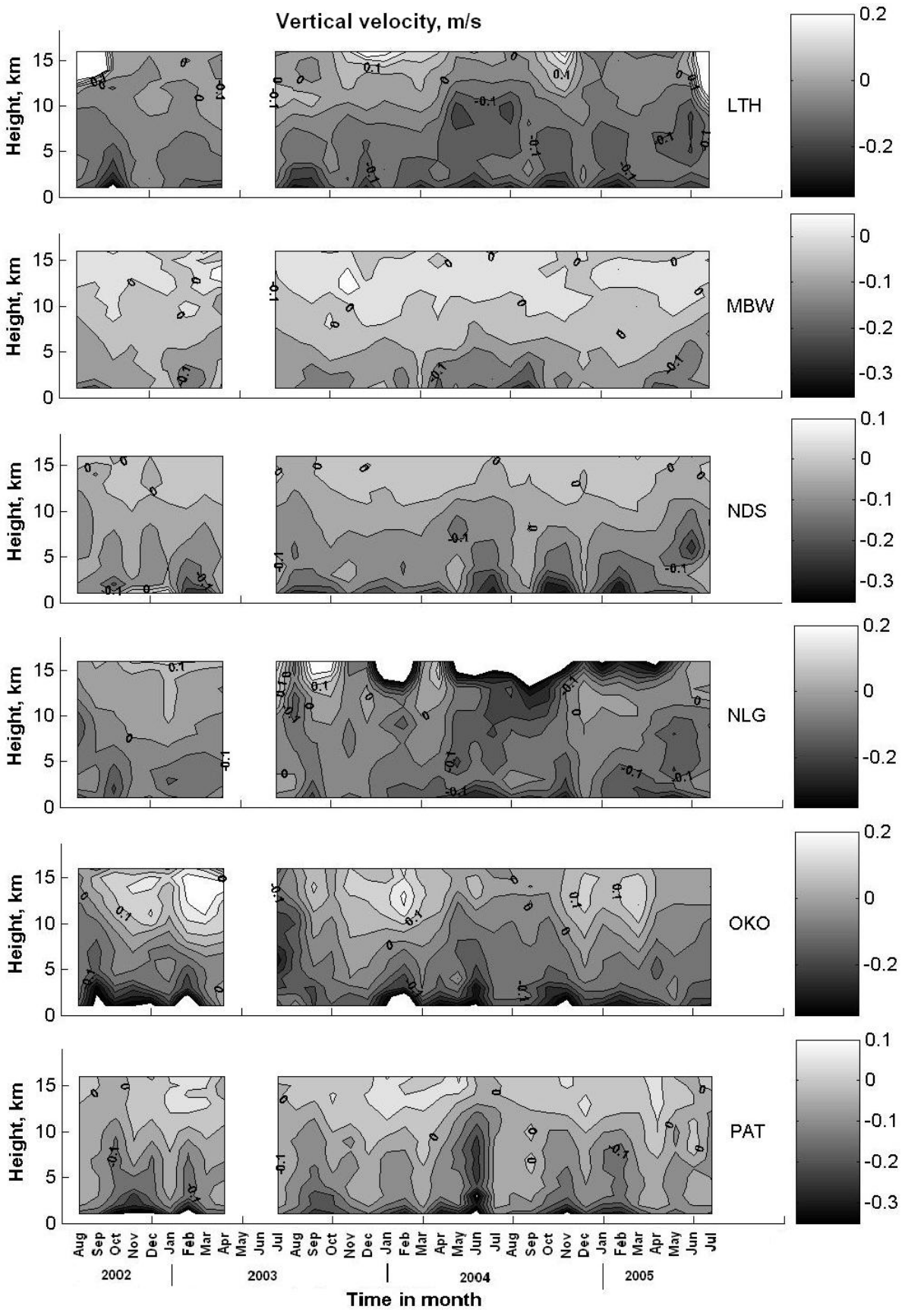
Vertical velocity, m/s
Height, km
LTH
MBW
NDS
NLG
OKO
PAT
Aug Sep Oct Nov Dec Jan Feb Mar Apr May Jun Jul Aug Sep Oct Nov Dec Jan Feb Mar Apr May Jun Jul Aug Sep Oct Nov Dec Jan Feb Mar Apr May Jun Jul
2002
2003
2004
2005
Time in month

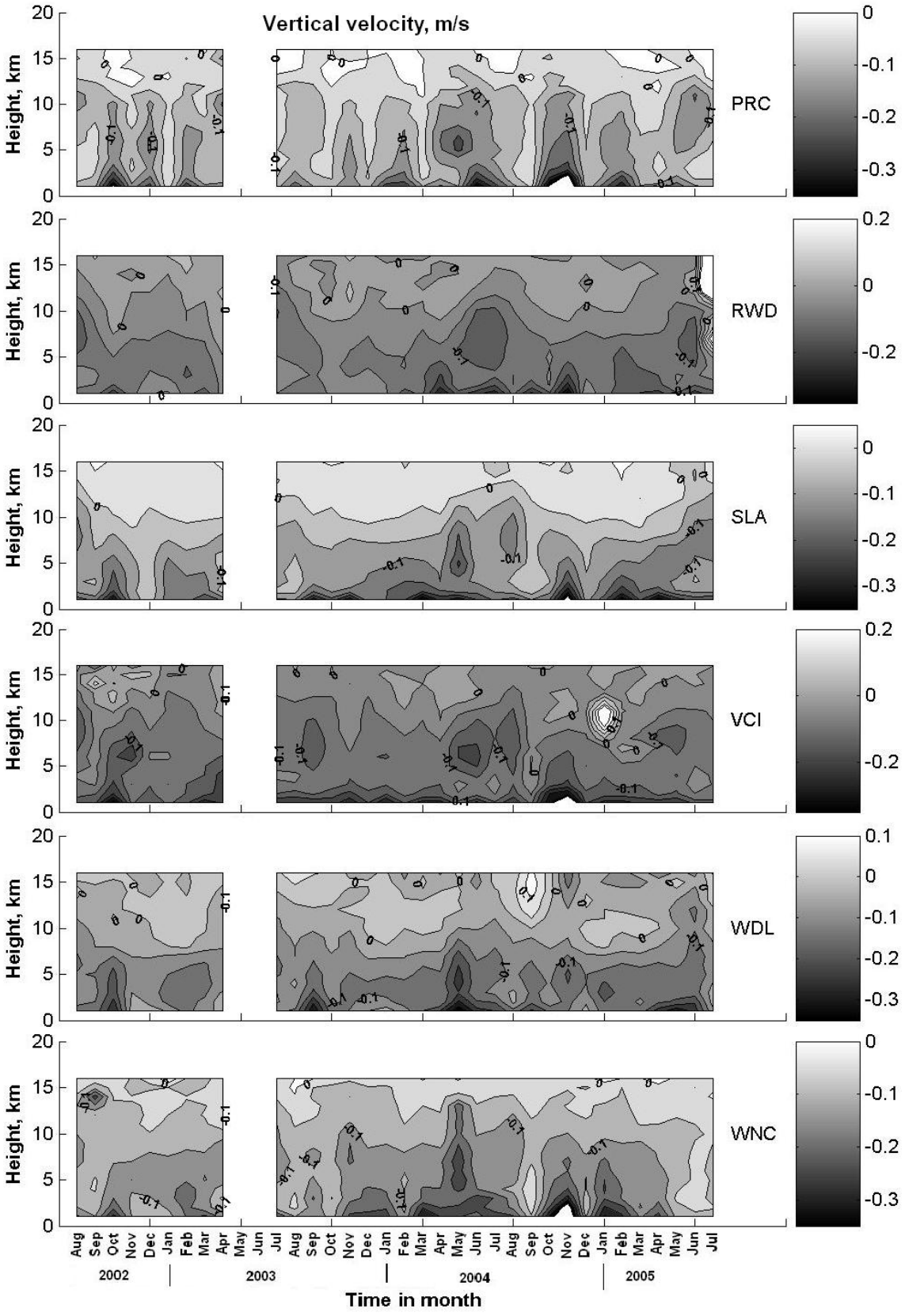
Vertical velocity, m/s
Height, km
PRC
RWD
SLA
VCI
WDL
WNC
Aug Sep Oct Nov Dec Jan Feb Mar Apr May Jun Jul Aug Sep Oct Nov Dec Jan Feb Mar Apr May Jun Jul Aug Sep Oct Nov Dec Jan Feb Mar Apr May Jun Jul
2002
2003
2004
2005
Time in month

APPENDIX D. The 3-year average profiles of vertical wind and seasonally averaged profiles for 24 profiler sites.

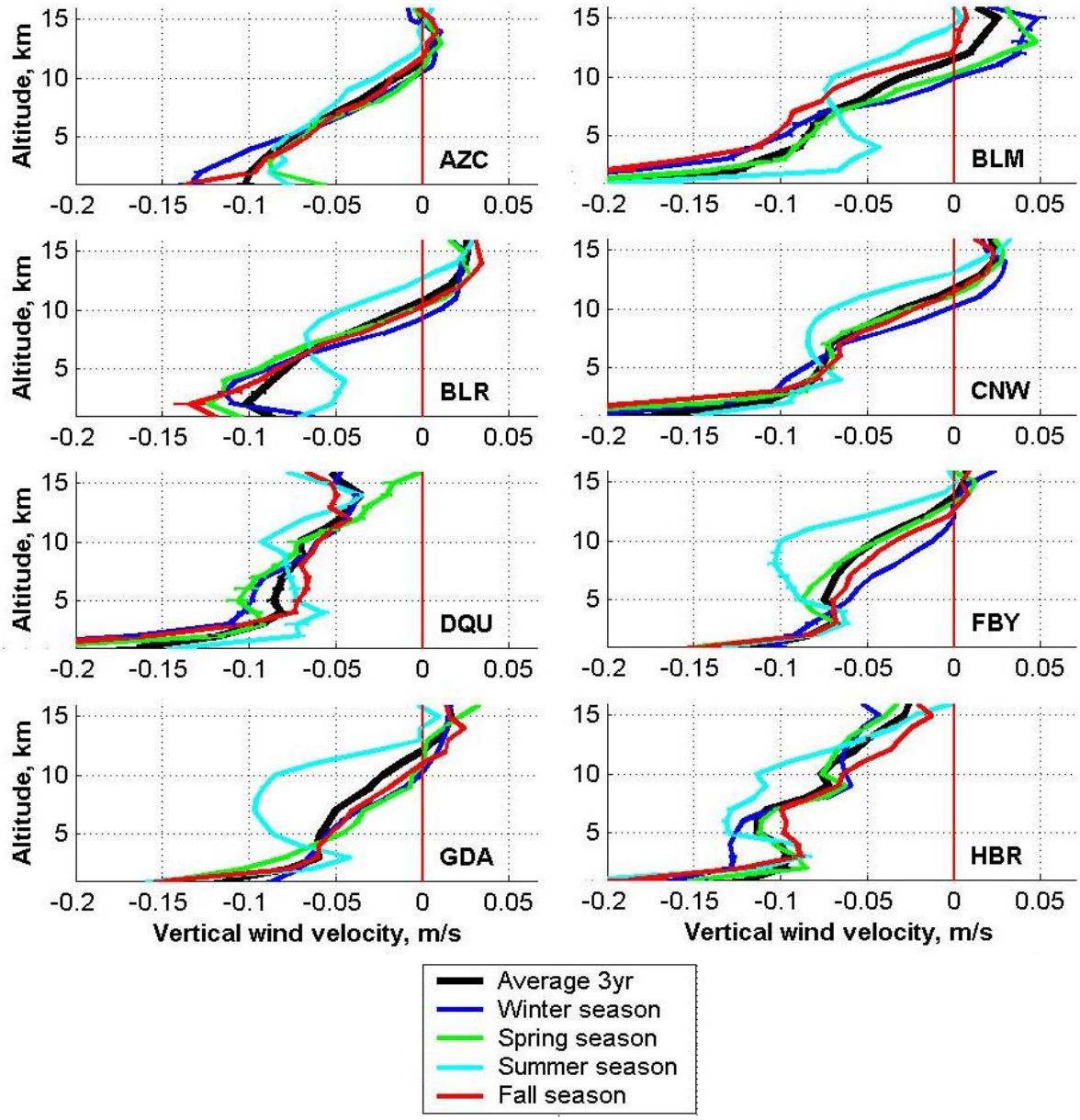

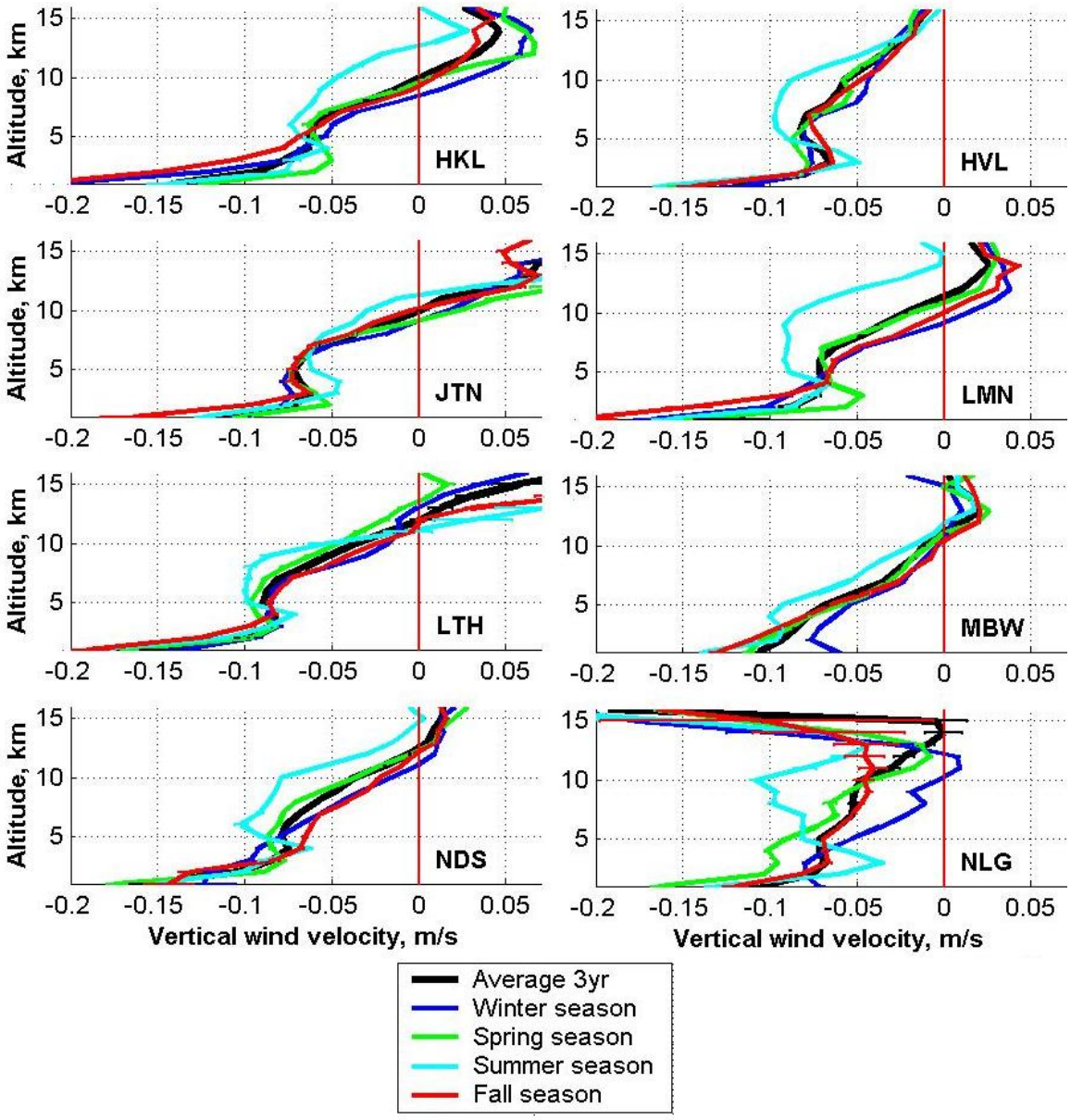
Altitude, km
15
10
5
-0.2
-0.15
-0.1
-0.05
0
0.05
HKL
HVL
JTN
LMN
LTH
MBW
NDS
NLG
Vertical wind velocity, m/s
Vertical wind velocity, m/s
Average 3yr
Winter season
Spring season
Summer season
Fall season

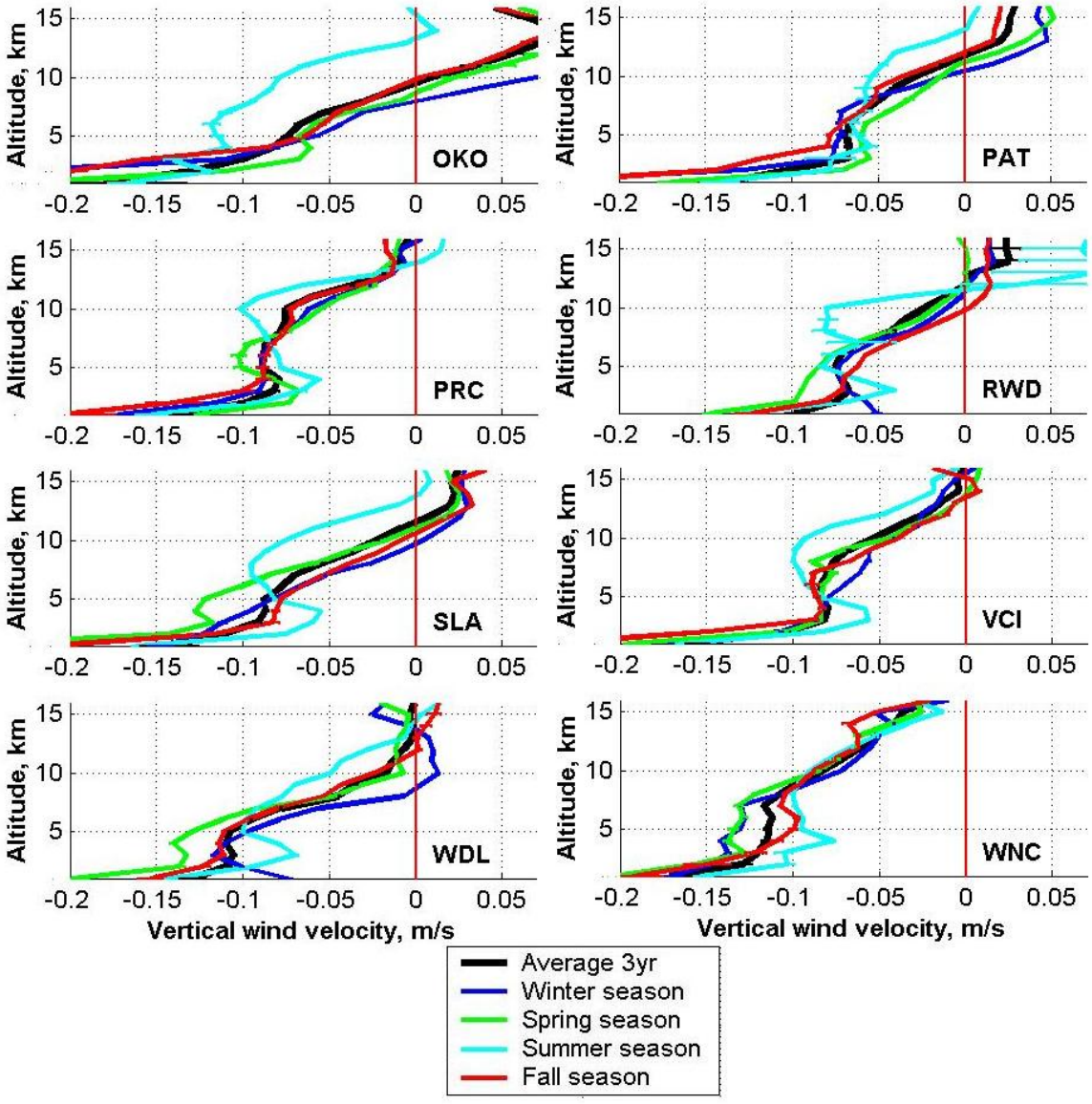
Altitude, km
15
10
5
-0.2
-0.15
-0.1
-0.05
0
0.05
OKO
PAT
PRC
RWD
SLA
VCI
WDL
WNC
Vertical wind velocity, m/s
Average 3yr
Winter season
Spring season
Summer season
Fall season

APPENDIX E. Time-altitude fields of monthly averaged total wind variance for wind profiler-measured winds.

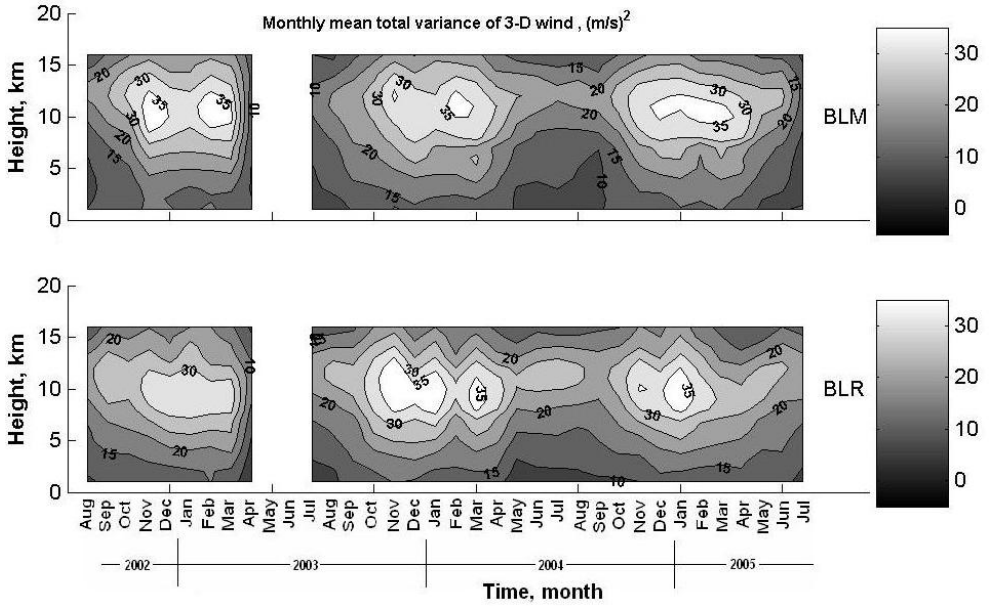

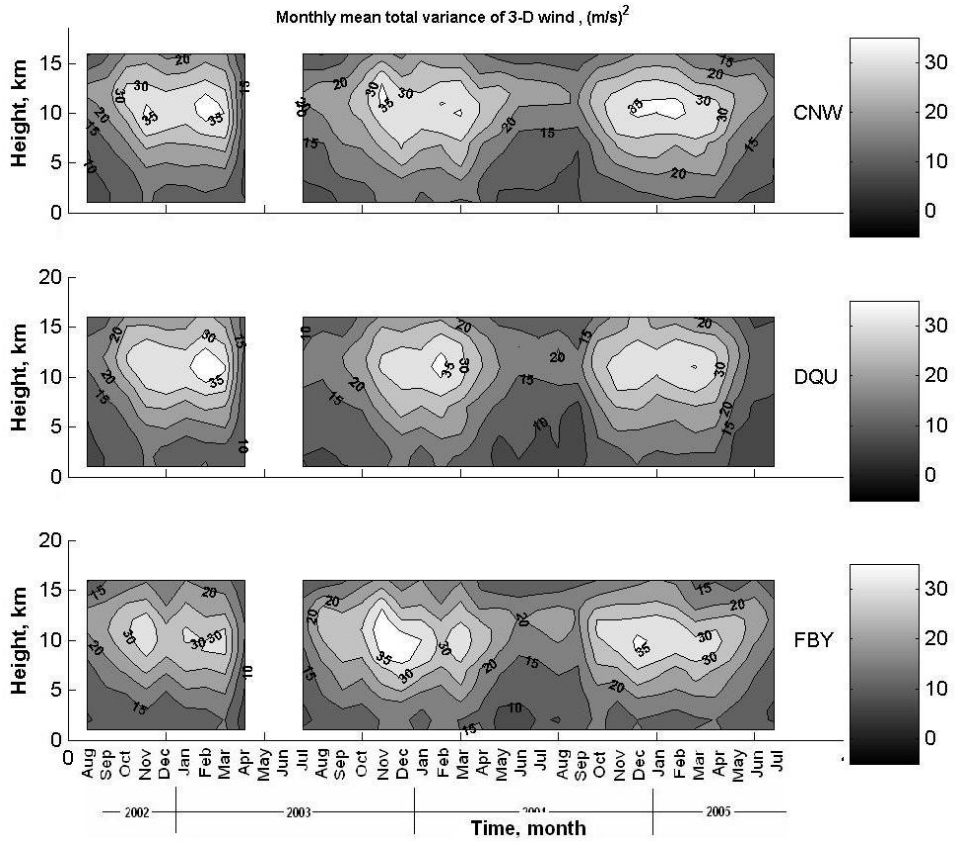

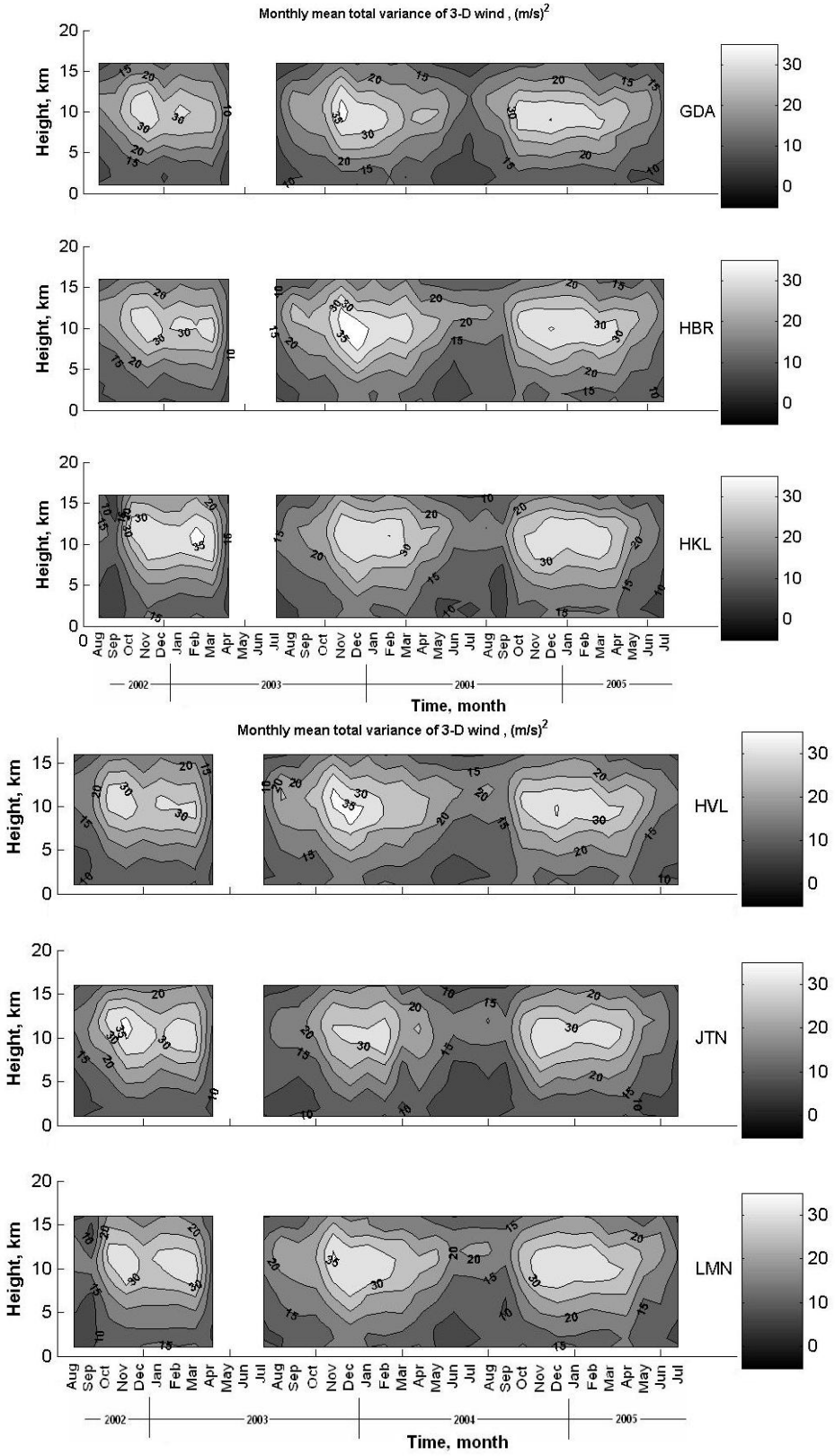
Monthly mean total variance of 3-D wind , (m/s)^2
Height, km
GDA
HBR
HKL
HVL
JTN
LMN
Time, month
2002
2003
2004
2005

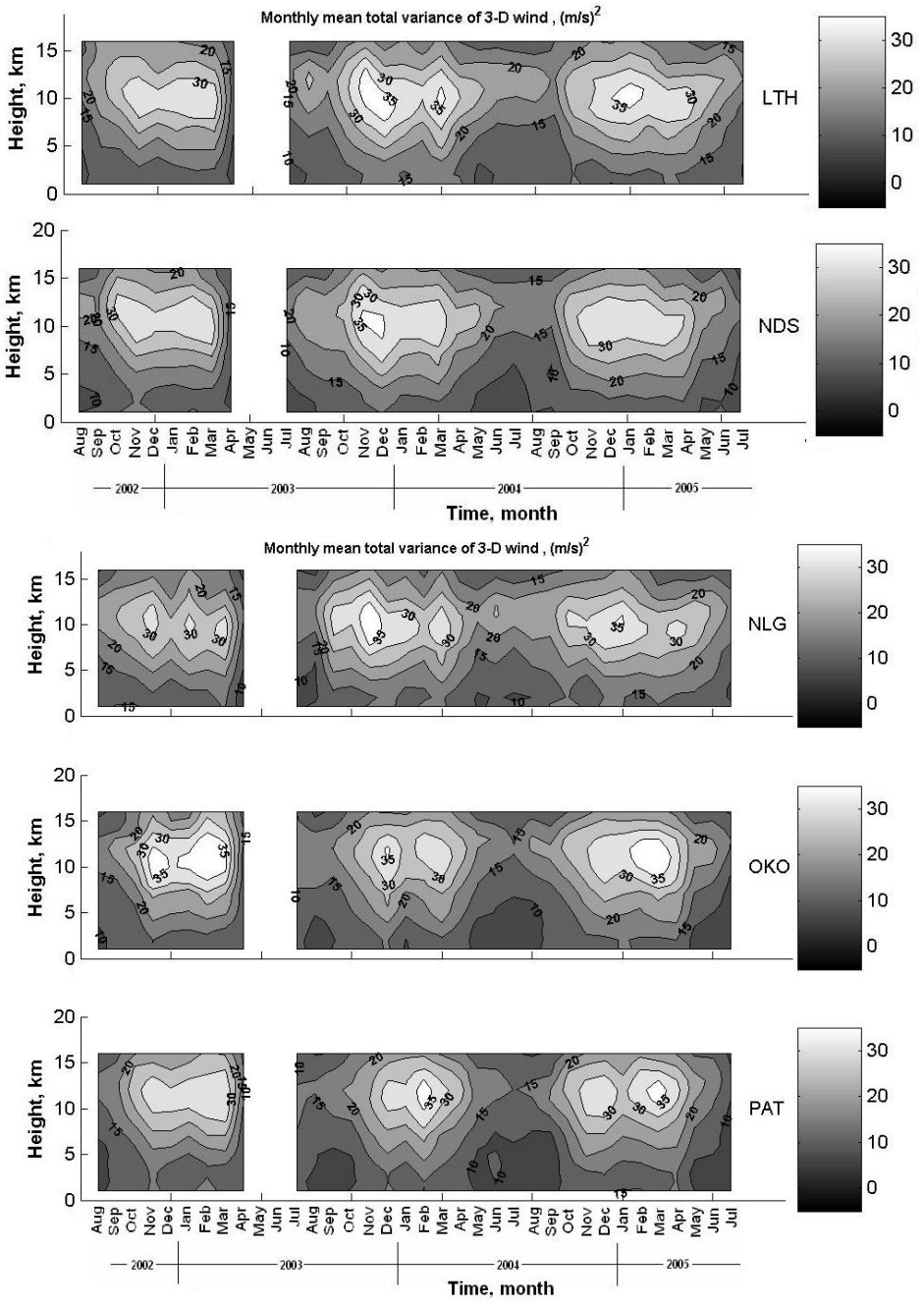
Monthly mean total variance of 3-D wind , (m/s)^2
Height, km
LTH
NDS
NLG
OKO
PAT
Aug Sep Oct Nov Dec Jan Feb Mar Apr May Jun Jul Aug Sep Oct Nov Dec Jan Feb Mar Apr May Jun Jul Aug Sep Oct Nov Dec Jan Feb Mar Apr May Jun Jul
2002
2003
2004
2005
Time, month

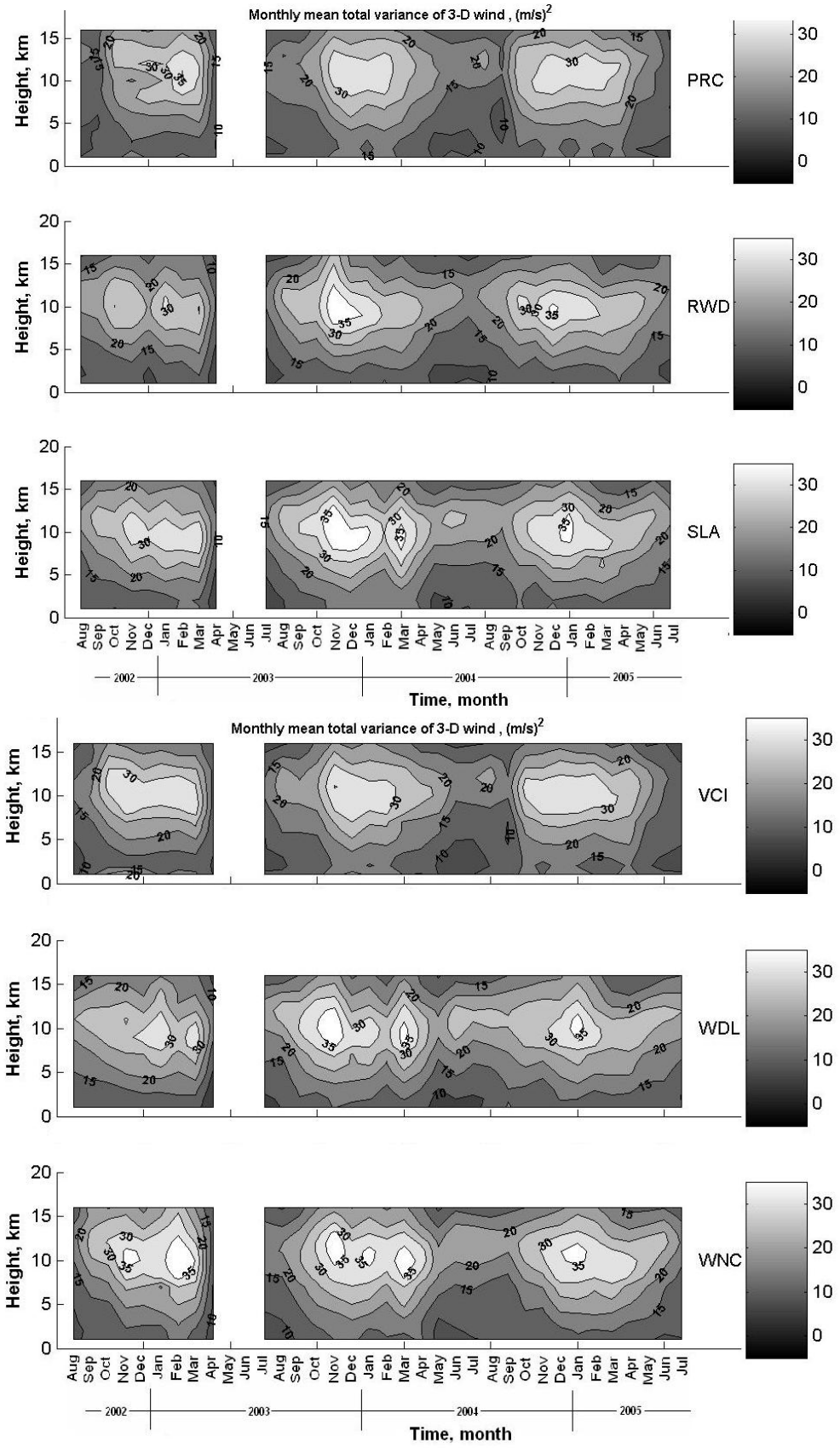
Monthly mean total variance of 3-D wind , (m/s)^2
Height, km
PRC
RWD
SLA
VCI
WDL
WNC
Aug Sep Oct Nov Dec Jan Feb Mar Apr May Jun Jul Aug Sep Oct Nov Dec Jan Feb Mar Apr May Jun Jul Aug Sep Oct Nov Dec Jan Feb Mar Apr May Jun Jul
2002
2003
2004
2005
Time, month

APPENDIX F. Time-altitude fields of total gravity wave energy E_k for 22 wind profilers.

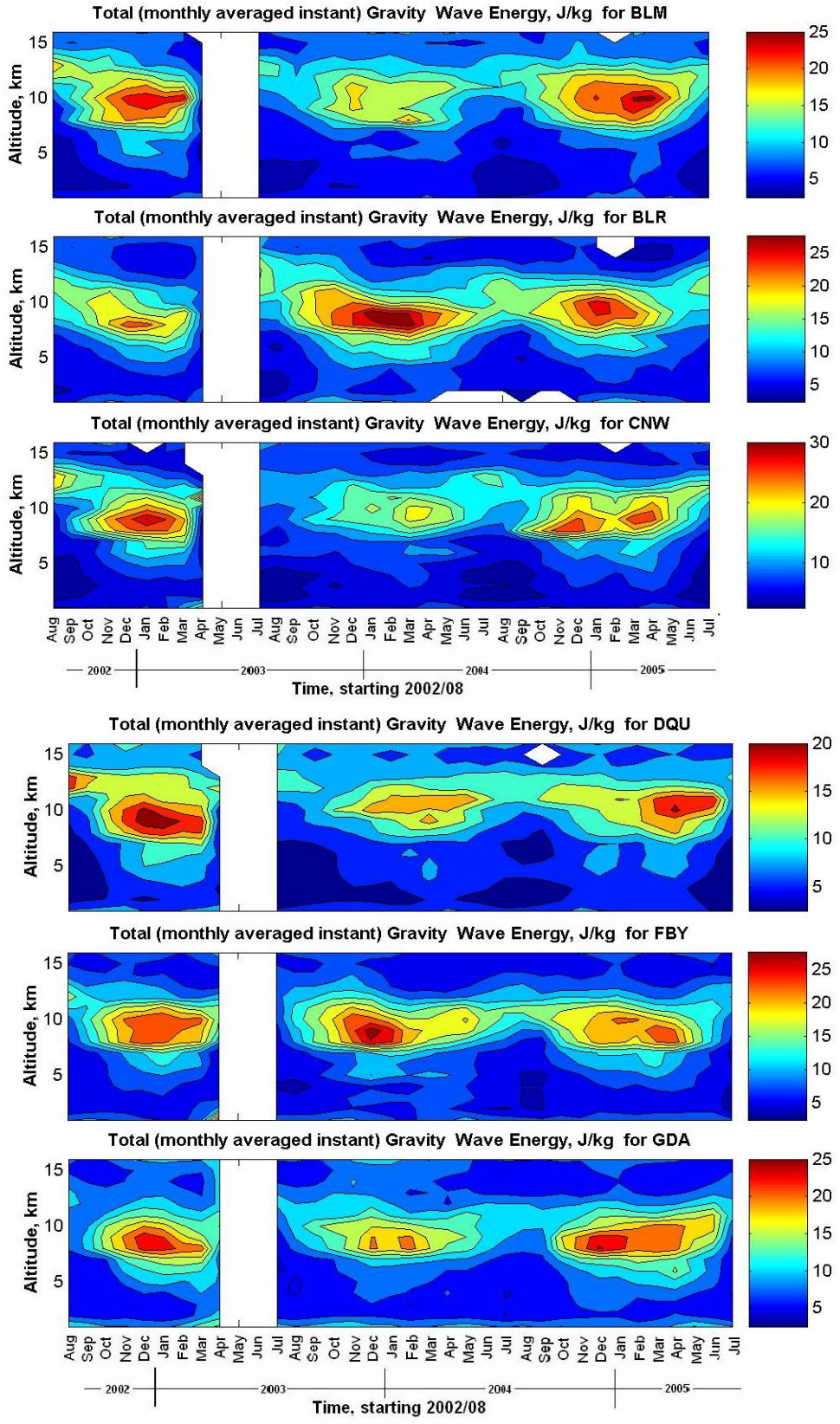

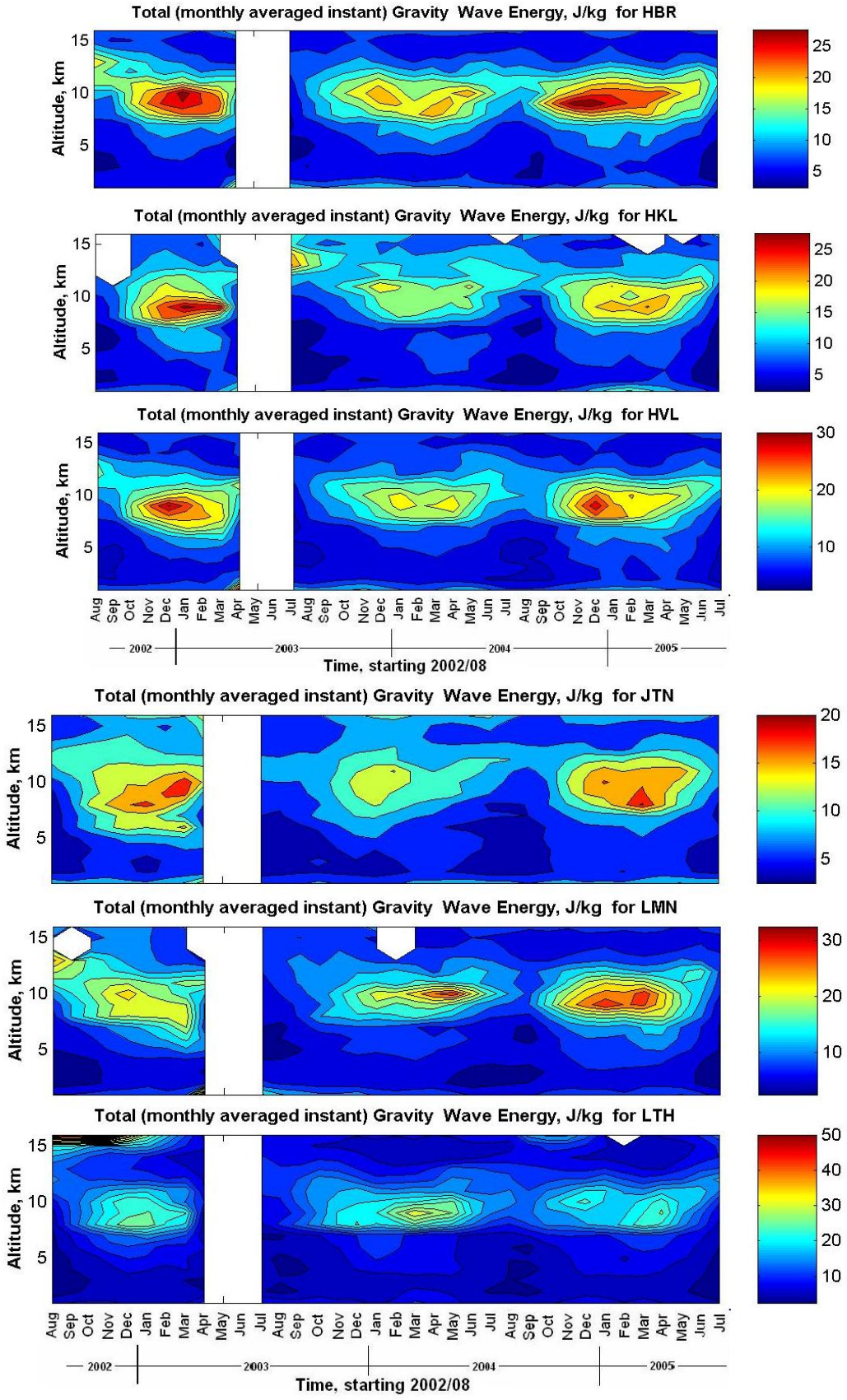
Total (monthly averaged instant) Gravity Wave Energy, J/kg for HBR
Altitude, km
15
10
5
25
20
15
10
5
Total (monthly averaged instant) Gravity Wave Energy, J/kg for HKL
Altitude, km
15
10
5
25
20
15
10
5
Total (monthly averaged instant) Gravity Wave Energy, J/kg for HVL
Altitude, km
15
10
5
30
20
10
Aug Sep Oct Nov Dec Jan Feb Mar Apr May Jun Jul Aug Sep Oct Nov Dec Jan Feb Mar Apr May Jun Jul Aug Sep Oct Nov Dec Jan Feb Mar Apr May Jun Jul
2002
2003
2004
2005
Time, starting 2002/08
Total (monthly averaged instant) Gravity Wave Energy, J/kg for JTN
Altitude, km
15
10
5
20
15
10
5
Total (monthly averaged instant) Gravity Wave Energy, J/kg for LMN
Altitude, km
15
10
5
30
20
10
Total (monthly averaged instant) Gravity Wave Energy, J/kg for LTH
Altitude, km
15
10
5
50
40
30
20
10
Aug Sep Oct Nov Dec Jan Feb Mar Apr May Jun Jul Aug Sep Oct Nov Dec Jan Feb Mar Apr May Jun Jul Aug Sep Oct Nov Dec Jan Feb Mar Apr May Jun Jul
2002
2003
2004
2005
Time, starting 2002/08

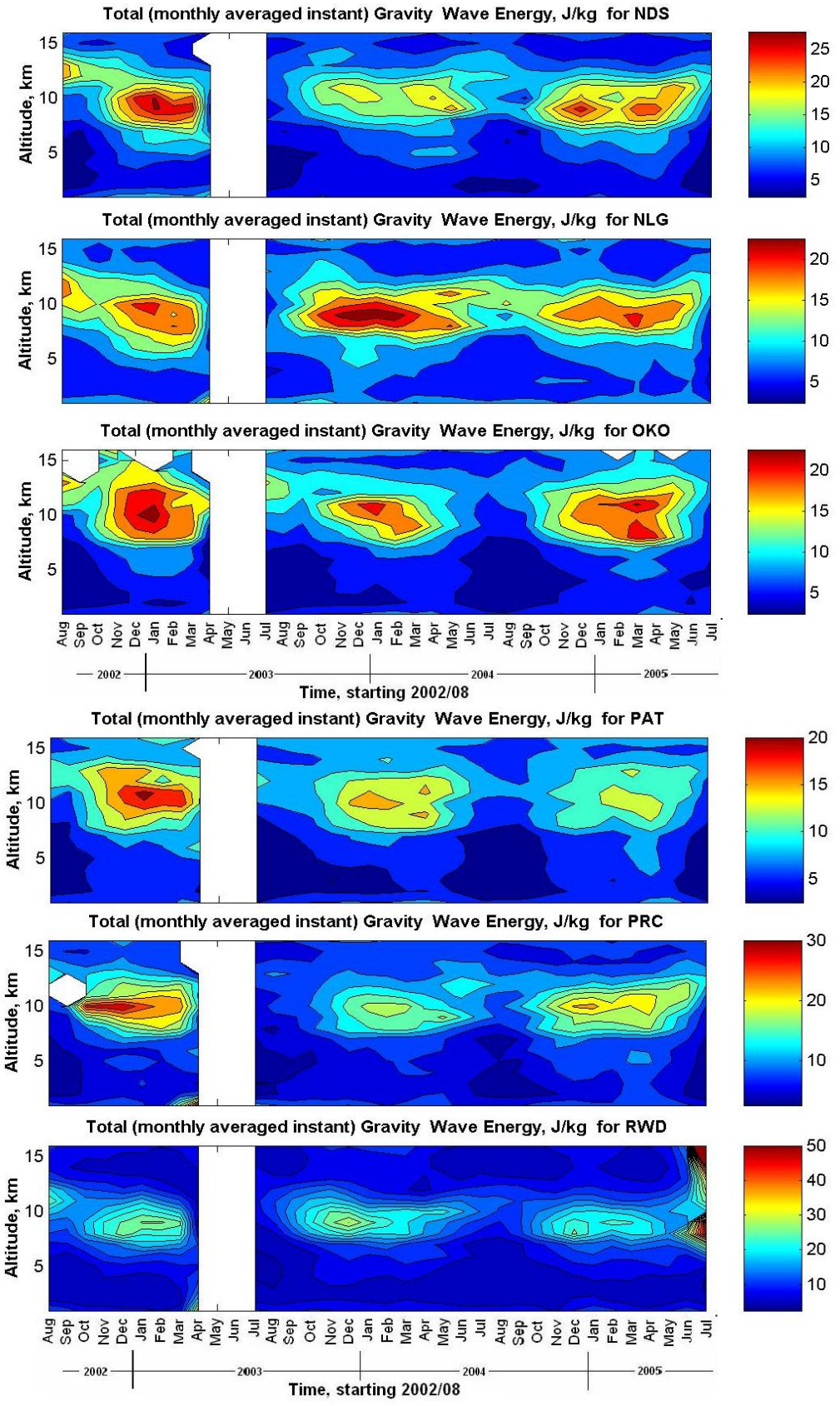
Total (monthly averaged instant) Gravity Wave Energy, J/kg for NDS
Altitude, km
15
10
5
25
20
15
10
5
Total (monthly averaged instant) Gravity Wave Energy, J/kg for NLG
Altitude, km
15
10
5
20
15
10
5
Total (monthly averaged instant) Gravity Wave Energy, J/kg for OKO
Altitude, km
15
10
5
20
15
10
5
Aug Sep Oct Nov Dec Jan Feb Mar Apr May Jun Jul Aug Sep Oct Nov Dec Jan Feb Mar Apr May Jun Jul Aug Sep Oct Nov Dec Jan Feb Mar Apr May Jun Jul
2002
2003
2004
2005
Time, starting 2002/08
Total (monthly averaged instant) Gravity Wave Energy, J/kg for PAT
Altitude, km
15
10
5
20
15
10
5
Total (monthly averaged instant) Gravity Wave Energy, J/kg for PRC
Altitude, km
15
10
5
30
20
10
Total (monthly averaged instant) Gravity Wave Energy, J/kg for RWD
Altitude, km
15
10
5
50
40
30
20
10
Aug Sep Oct Nov Dec Jan Feb Mar Apr May Jun Jul Aug Sep Oct Nov Dec Jan Feb Mar Apr May Jun Jul Aug Sep Oct Nov Dec Jan Feb Mar Apr May Jun Jul
2002
2003
2004
2005
Time, starting 2002/08

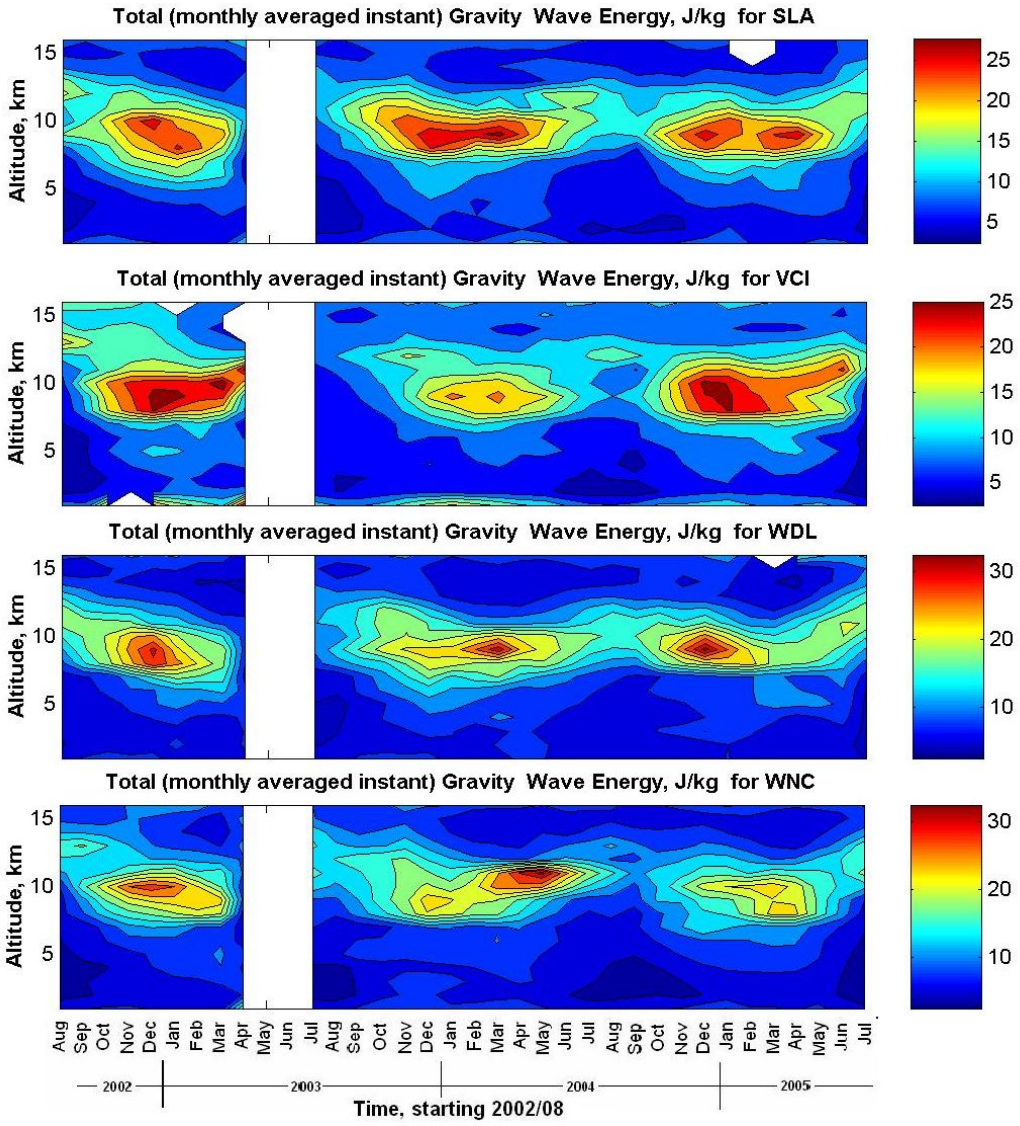
Total (monthly averaged instant) Gravity Wave Energy, J/kg for SLA
Altitude, km
15
10
5
25
20
15
10
5
Total (monthly averaged instant) Gravity Wave Energy, J/kg for VCI
Altitude, km
15
10
5
25
20
15
10
5
Total (monthly averaged instant) Gravity Wave Energy, J/kg for WDL
Altitude, km
15
10
5
30
20
10
Total (monthly averaged instant) Gravity Wave Energy, J/kg for WNC
Altitude, km
15
10
5
30
20
10
Aug Sep Oct Nov Dec Jan Feb Mar Apr May Jun Jul Aug Sep Oct Nov Dec Jan Feb Mar Apr May Jun Jul Aug Sep Oct Nov Dec Jan Feb Mar Apr May Jun Jul
2002
2003
2004
2005
Time, starting 2002/08

REFERENCES

Allen, S.J. and R. Vincent, 1995. Gravity wave activity in the lower atmosphere: Seasonal and latitudinal variations. Journal of Geophysical Research, **100 (D1)**, 1327-1350.

Alexander, M.J., T. Tsuda, R.A. Vincent, 2002. Latitudinal Variations Observed in Gravity Waves with Short Vertical Wavelengths. Journal of the Atmospheric Sciences, **59(8)**, 1394-1405.

Balsley, B.B. and K.S. Gage, 1980. The MST Radar Technique: Potential for Middle Atmospheric Studies, Pure Appl. Geophys., **118,** 452-493.

Beatty, T.J., C. A. Hostetler, and C.S. Gardner, 1992. Lidar Observations of Gravity Waves and Their Spectra near the Mesopause and Stratopause at Arecibo. Journal of the Atmospheric Sciences, Vol. **49**, 477-496.

Beres, J.H., M.J. Alexander, and J.R. Holton, 2002. Effects of tropospheric wind shear on the spectrum of convectively generated gravity waves. Journal of the Atmospheric Sciences, **59 (11)**, 1805-1824.

Black, R.X., B.A. McDaniel, and W.A. Robinson, 2005. Stratosphere-Troposphere Coupling during Spring Onset. Journal of Climate (in press).

Butchart, N., and A.A. Scaife, 2001. Removal of chlorofluorocarbons by increased mass exchange between the stratosphere and troposphere in a changing climate. Nature, **410 (6830),** 799-802.

Chadwick R.B., 1986. Wind profiler demonstration network. Handbook for MAP, Vol. 20., S.A. Bowhill and B. Edwards, Eds., URSI/SCOSTEP, 336-337.

Chang, J.L., S.K. Avery, A.C. Riddle, et al., 1997. First results of tropospheric gravity wave momentum flux measurements over Christmas Island. Radio Science, **32 (2)**, 727-748.

Chu, Y.H., T.Y. Chen, and T.H. Lin, 1997. An examination of the wind-driven effect on the drift of precipitation particles using the Chung-Li VHF radar. Radio Science, **32**(**3**), 957-966.

Cifelli, R., S.A. Rutledge, D.J. Boccippio, et al., 1996. Horizontal divergence and vertical velocity retrievals from Doppler radar and wind profiler observations. Journal of Atmospheric and Oceanic Technology, **13 (5)**, 948-966.

Clifford, S.F., J.C. Kaimal, R.J. Lataitis and R.G. Strauch, 1994. Ground-based remote profiling in Atmospheric studies: An overview. Proc. IEEE, **82 (3)**, 313-355.

Colwell, R.C., and A.W. Friend, 1936. The D region of the ionosphere. Nature, vol. **137**. 782 -791.

DeVries, A.C., W.P. Kustas, J.C. Ritchie, et al., 2003. Effective aerodynamic roughness estimated from airborne laser altimeter measurements of surface features. International Journal of Remote Sensing, **24 (7)**, 1545-1558.

Doviak, R.J., and D.S. Zrnić, 1984a. Doppler radar and weather observations. Orlando, Florida.: Academic Press, 458 p.

Doviak, R.J., and D.S. Zrnić, 1984b. Reflection and scatter formula for anisotropically turbulent air. Radio Sci.**, 19,** 325–336.

Ecklund, W.L., Gage K.S., Balsley B.B., et al., 1982. Vertical wind variability observed by the VHF radar in the lee of the Colorado Rockies. Monthly Weather Review, **110 (10)**, 1451-1457.

Egger, J., and K.P. Hoinka, 2005. Downward control from the lower stratosphere? Journal of the Atmospheric Sciences, **62 (10)**, 3808-3817.

Fritts, D.C., M.A. Geller, B.B. Balsley, et al., 1984. Research status and recommendations from the Alaska workshop on gravity waves and turbulence in the middle atmosphere. Fairbanls, Alaska, 18-22 July 1983. Bulletin of the American Meteorological Society, **65 (2)**, 149-159.

Gage, K.S., and B.B. Balsley, 1978. Doppler Radar Probing of the Clear Atmosphere. Bulletin of the American Meteorological Society**, 59 (9)**, 1074–1093.

Gage, K.S., 1983. On the measurement of vertical velocity by MST radar. Handbook for MAP.: S.A. Bowhill and B. Edvards, Eds., **9**, 215-226.

Gage, K.S., J.R. McAfee, D.A. Carter, et al., 1991. Long-term mean vertical motion over the tropical Pacific – wind-profiling radar measurements. Science **254 (5039)**, 1771-1773.

Gardner, C.S., M.S. Miller, and C.H. Liu, 1989. Rayleigh lidar observations of gravity wave activity in the upper stratosphere at Urbana, Illinois. Journal of the Atmospheric Sciences, vol. **46**, 1838-1854.

Gordon, W.E., 1958. Incoherent scattering of radio waves by free electrons with applications to space exploration by radar. Proc. IRE, vol. **46**, 1824-1829.

Gossard, E.E. and W.H. Hooke**,** 1975. Waves in the atmosphere : atmospheric infrasound and gravity waves: their generation and propagation. New York: Elsevier Scientific Pub. Co., 456 p.

Green, J.L., K.S. Gage, T.E. VanZandt, et al., 1988. Observations of vertical velocity over Illinois by the Flatland radar. Geophysical Research Letters, **15 (3)**, 269-272.

Hamilton, K. 1996. Comprehensive meteorological modeling of the middle atmosphere: A tutorial review. Journal of Atmospheric and Terrestrial physics, **58**, 1591 – 1627.

Hamilton, K, R.A. Vincent, and P.T. May, 2004. Darwin Area Wave Experiment (DAWEX) field campaign to study gravity wave generation and propagation. Journal of Geophysical Research – Atmospheres, **109 (D20)**, Art. No. D20S01.

Hansen, A.R., G.D. Nastrom, F.D. Eaton, 2001. Seasonal variation of gravity wave activity at 5-20 km observed with VHF radar at White Sands Missile Range, New Mexico. Journal of Geophysical Research – Atmospheres, **106 (D15)**, 17171-17183.

Hardy, K.R., 1967. Radar echoes from the clear air. NATO Advanced Study Institute, Univ. College of Wales, Aberystwyth, Wales.

Hertzog, A., C. Souprayen, and A. Hauchecorne, 2001. Measurements of gravity wave activity in the lower stratosphere by Doppler lidar. Journal of Geophysical Research **106 (D8)**, 7879-7890.

Hirota, I., 1984. Climatology of gravity waves in the middle atmosphere. Atm. Terr. Phys., **46**, 767-773.

Hirota, I., 1997. Some problems relating to the observed characteristics of gravity waves in the middle atmosphere. In: Gravity Wave Processes : their parameterization in global climate models / Edited by K. Hamilton. NATO ASI series. Series I, Global environment change; vol. **50**. Springer-Verlag.

Holton, J.R., 1990. On the global exchange of mass between the stratosphere and troposphere. Journal of the Atmospheric Sciences, **47 (3)**, 392-395.

Holton, J.R., 2004. An introduction to dynamic meteorology. 4th ed. Burlington, MA: Elsevier Academic Press.

Huaman, M.M., and B.B. Balsley, 1996. Long-term average vertical motions observed by VHF wind profilers: The effect of slight antenna-pointing inaccuracies. Journal of Atmospheric and Oceanic Technology, **13 (3)**, 560-569.

Janowiak, J.E., A. Gruber, C.R. Kondragunta, et al., 1998. A comparison of the NCEP-NCAR reanalysis precipitation and the GPCP rain gauge-satellite combined dataset with observational error considerations. Journal of Climate, **11 (11)**, 2960-2979.

Jiang J.H., S.D. Eckermann, and D.L. Wu et al., 2005. Seasonal variation of gravity wave sources from satellite observation. Advances in Space Research **35 (11)**, 1925-1932.

Kashcheyev, B.L., V. Oleynikov, A. Oleynikov, O. Solyanik, A. Karabanov, 1998. Some results from the atmospheric wind profiler of the Kharkov University of Radioelectonics. Meteorologische Zeitschrift, NF **7** , 1 – 4.

Kato, S., T. Ogawa, T. Tsuda, T. Sato, I. Kimura, and S. Fukao, 1884. The Middle and Upper Atmosphere Radar: First Results Using a Partial System. Radio Science, **19**, 1475-1484.

Kitamura, Y., and I. Hirota, 1989: Small-scale disturbances in the lower stratosphere revealed by daily rawin sonde observations. J. Meteor. Soc. Japan, **67**, 817-831.

Larsen, M.F., J. Rottger, and T.S. Dennis, 1988. A comparison of operational analysis and VHF profiler vertical velocities. Monthly Weather Review, **116 (1)**, 48-59.

Larsen, M.F., and R.D. Palmer, 1997. A relationship between horizontal flow gradients, in-beam incidence angles, and vertical velocities. Radio Science, **32 (3)**, 1269-1277.

Mace, G.G., and T.P. Ackerman, 1996. Assessment of error in synoptic-scale diagnostics derived from wind profiler and radiosonde network data. Monthly Weather Review, **124 (7)**, 1521-1534.

Manning, L.A., O.G. Villard, and A.M. Peterson, 1953. Meteoric echo study of upper atmospheric winds. Proc. IRE. vol. **38**, 877 - 883.

May, P.T., S. Fukao, T. Tsuda, et al., 1988. The effect of thin scattering layers on the determination of wind by Doppler radars. Radio Science, **23 (1)**, 83-94.

McAfee, J.R., Gage KS, and R.G. Strauch, 1995. Vertical velocities at Platteville, Colorado – an intercomparison of simultaneous measurements by the VHF and UHF profilers. Radio Science, **30 (4)**, 1027-1042.

McLandress, C., 1998. On the importance of gravity waves in the middle atmosphere and their parameterization in general circulation models. Journal of Atmospheric and Solar-Terrestrial Physics, **60 (14)**, 1357-1383.

Monna, W.A.A., 1994. On the use of wind profilers in meteorology. Ann. Geophys., **12 (6)**, 482-486.

Mukougawa, H., and T. Hirooka, 2004. Predictability of stratospheric sudden warming: A case study for 1998/99 winter. Monthly Weather Review, **132 (7)**, 1764-1776.

Murayama, Y., T. Tsuda, and S. FUKAO, 1994. Seasonal-variation of gravity-wave activity in the lower atmosphere observed with the MU-radar. Journal of Geophysical Research – Atmospheres, **99 (D11)**, 23057-23069.

Muschinski, A., 1996. Possible effect of Kelvin-Helmholtz instability of VHF radar observations of the mean vertical wind. Journal of Applied Meteorology, **35 (12)**, 2210-2217.

Muschinski, A., and C. Wode, 1998. First in situ evidence for coexisting submeter temperature and humidity sheets in the lower free troposphere. Journal of the Atmospheric Sciences, **55 (18)**, 2893–2906**.**

Nappo, C.J., 2002. An introduction to atmospheric gravity waves. International geophysics series ; vol. **85**. San Diego, Calif. : Academic Press.

Nash, J., 1994. Upper wind observing systems used for meteorological operations. Ann. Geophys. **12 (8)**, 691-710.

National Weather Service and the Office of Oceanic and Atmospheric Research, August 1994, Wind Profiler Assessment Report and Recommendations for Future Use 1987-1994, U.S. Department of Commerce, National Oceanic and Atmospheric Research, Silver Spring, Maryland, 141 pp.

Nastrom, G.D., and K.S. Gage, 1984. A brief climatology of vertical wind variability in the troposphere and stratosphere as seen by the Pocker Flat, Alaska, MST radar. Journal of Climate and Applied Meteorology, **23 (3)**, 453-460.

Nastrom, G.D., M.R. Peterson, J.L. Green, K.S. Gage and T.E. VanZandt, 1990a. Sources of gravity Wave activity seen in the vertical velocities observed by the Flatland VHF Radar. Journal of applied meteorology, **29 (8)**, 783-792.

Nastrom, G.D., K.S. Gage, W.L. Ecklund, 1990. Uncertainties in estimates of the mean vertical velocity from MST radar observations. Radio Science, **25 (5)**, 933-940.

Nastrom, G.D., W.L. Clark, K.S. Gage, et al., 1994a. Case-studies of the vertical velocity seen by the Flatland radar compared with indirectly computed values. Journal of Atmospheric and Oceanic Technology, **11 (1)**, 14-21.

Nastrom, G.D. and T.E. VanZandt, 1994b. Mean vertical motions seen by radar wind profilers. Journal of Applied Meteorology, vol. **33**, p. 984 – 995.

Nastrom, G.D., and J.M. Warnock, 1994. Vertical motions estimated using data from a single station and a form of the adiabatic method. Journal of the Applied Meteorology, **33 (1)**, 65-73.

Nastrom G.D. and T.E. VanZandt, 1996. Biases due to gravity waves in wind profiler measurements of winds. Journal of Applied Meteorology, **35 (2)**, 243-257.

Nastrom, G.D., R. Ruster, and G. Schmidt, 1998. The coupling of vertical velocity and signal power observed with the SOUSY VHF radar. Journal of Applied Meteorology, **37**, 114-119.

Neiman, P.J., P. T. May, and M.A. Shapiro, 1992. Radio acoustic sounding system (RASS) and Wind Profiler observations of Lower- and Midtropospheric weather systems. Monthly Weather Review, **120**, 2298-2313.

Neter, J., W. Wasserman, and M. H. Kutner, 1996. Applied linear statistical models: regression, analysis of variance, and experimental designs. Homewood, IL: Irwin, xvi, 3rd ed., 1181 p.

Oleynikov V.N., and Karabanov A.G., 1997. Algorithms of Secondary Data Processing in the Atmospheric Wind Profiler .- In: COST-76 Profiler Workshop Extended Abstracts, Vol. **2**, 326-329.

Oleynikov V.N., O.A. Solyanik, and A.G. Karabanov, 1997. Low-potential Atmospheric Vertical Sounding Radar Station. Telecommunications and Radio Engineering, **51 (8)**, 13-15.

Orr, B.W., and B.E. Martner, 1996. Detection of weakly precipitating winter clouds by a NOAA 404-MHz wind profiler. Journal of Atmospheric and Oceanic Technology, **13 (3),** 570-580.

Peterson, V.L., B.B. Balsley, 1979. Clear air Doppler radar measurements of the vertical component of wind velocity in the troposphere and stratosphere. Geophysical Research Letters, **6 (12)**, 933-936.

Philbrick, C.R. and B. Chen. Transmission of Gravity Waves and Planetary Waves in the Middle Atmosphere Based on Lidar and Rocket Measurements. Adv. Space Res. **12 (10)**, 303-306.

Rao, V.V.M.J., D.N. Rao, M.V. Ratnam, et al., 2003. Mean vertical velocities measured by Indian MST radar and comparison with indirectly computed values Journal of Applied Meteorology, **42 (4)**, 541-552.

Ralph, F.M., P.J. Neiman, D.W. van de Kamp, et al., 1995a. Using spectral moment data from NOAAs 404-MHz radar wind profiler to observe precipitation. Bulletin of American Meteorological Society, **76 (10),** 1717-1739.

Ralph, F.M., 1995b. Using radar-measured radial vertical velocities to distinguish precipitation scattering from clear-air scattering. Journal of Atmospheric and Oceanic Technology, **12 (2)**, 257-267.

Ralph, F.M., P.J. Neiman, and D. Ruffieux, 1996. Precipitation identification from radar wind profiler spectral moment data: Vertical velocity histograms, velocity variance, and signal power vertical velocity correlations. Journal of Atmospheric and Oceanic Technology, **13 (3)**, 545-559.

Rastogi, P.K., 1983. Spectral characteristics of the MST radar returns. Handbook for middle atmosphere program. Urbana, Illinois. Vol.**9**, 105 - 111.

Rastogi, P.K., 1986. An overview of data acquisition, signal coding and data analysis techniques for MST radars. Handbook for middle atmosphere program. Urbana, Illinois. Vol. **20,** 431-440.

Rastogi, P.K., 1989. Signal processing and data analysis in middle atmosphere radar. Handbook for middle atmosphere program. Urbana, Illinois. Vol. **28**, 567-592.

Rottger, J. and M.F. Larsen,1990. UHF/VHF radar techniques for atmospheric research and wind profiler applications. In: Radar in Meteorology. D. Atlas, Ed. Boston, MA: American Meteorological Society, ch.21a, 235-281.

Ruster, R, G.D. Nastrom, and G. Schmidt, 1998. High-resolution VHF radar measurements in the troposphere with a vertically pointing beam. Journal of Applied Meteorology, **37 (11)**, 1522-1529.

Salby, M. L., 1996. Fundamentals of atmospheric physics. San Diego, Calif.: Academic Press, 627 p.

Şen, Z. Terrain topography classification for wind energy generation. Renewable energy, **16**, 904-907.

Serafimovich A., P. Hoffmann, D. Peters, et al., 2005. Investigation of inertia-gravity waves in the upper troposphere/lower stratosphere over Northern Germany observed with collocated VHF/UHF radars. Atmospheric Chemistry and Physics, **5**, 295-310.

Schafer, R., S. K. Avery, and K. S. Gage, 2003. A Comparison of VHF Wind Profiler observations and the NCEP/NCAR Re-analysis over the Tropical Pacific. Journal of Applied Meteorology, **42 (7)**, 873-889.

Schmid, H.P., 1994. Source areas for scalars and scalar fluxes. Boundary-Layer Meteorology, 67 (3), 293-318.

Schuepp, P.H., M.Y. Leclerc, J.I. MacPherson, et al., 1990. Footprint prediction of scalar fluxes from analytical solutions of the diffusion equation. Boundary-Layer Meteorology, **50 (1-4)**, 353-373.

Tieleman, H.W., 2003. Roughness estimation for wind-load simulation experiments. Journal of Wind Engineering and Industrial Aerodynamics, vol. 91, 1163–1173.

Trexler, C.M., and S.E. Koch, 2000. The life cycle of a mesoscale gravity wave as observed by a network of Doppler wind profilers. Monthly Weather Review, **128 (7)**, 2423-2446.

Tsuda, T., T. Sato, K. Hirose, S. Fukao and S. Kato, 1986. MU radar observations of the aspect sensitivity of the backscattered VHF echo power in the troposphere and lower stratosphere, Radio Science, **21 (6)**, 971-980.

Tsuda, T., M. Nishida, C. Rocken, and R. H. Ware, 2000. A global morphology of gravity wave activity in the stratosphere revealed by the GPS Occultation data (GPS/MET), Journal of Geophysical Research, **105 (D6)**, 7257–7274.

U.S. Standard Atmosphere, 1976. U.S. Government Printing Office, Washington, D.C.

VanZandt T.E., 2000. A brief history of the development of wind-profiling or MST radars. Ann. Geophys. – Atm. Hydr., **18 (7)**, 740-749.

Vaughan, G., and R.M. Worthington, 2000. Effects of humidity and precipitation on VHF radar vertical beam echoes. Radio Science, **35 (6)**, 1389-1398.

Vincent, R.A., J.S. Allen, and S.D. Eckermann, 1997. Gravity wave parameters in the lower Stratosphere. In: Gravity Wave Processes : their parameterization in global climate models. Edited by K. Hamilton. NATO ASI series. Series I, Global environment change; vol. **50**. Springer-Verlag.

Wang, L., and M.A. Geller, 2003. Morphology of gravity-wave energy as observed from 4 years (1998-2001) of high vertical resolution U.S. radiosonde data. Journal of Geophysical research, **108 (D16)**, 4489.

Woodman, R. F., and A. Gullen, 1974. Radar observations of winds and turbulence in the stratosphere and mesosphere. Journal of Atmospheric Sciences, **31 (2)**, 493-505.

Worthington, R.M., 1999. Calculating the azimuth of mountain waves, using the effect of tilted fine-scale stable layers on VHF radar echoes. Ann. Geophys-Atm Hydr., **17 (2)**, 257-272.

Worthington, R.M., A. Muschinski, and B.B. Balsley, 2001. Bias in mean vertical wind measured by VHF radars: Significance of radar location relative to mountains. Journal of the Atmospheric Sciences, **58 (7)**, 707-723.

VITA

OLEKSANDR G. KARABANOV

Oleksandr (Aleks) Karabanov was born in Ukraine, at that time a republic of the Soviet Union. By the time he received a B.S. degree with highest honors from Kharkov University of Radio Electronics, Ukraine became an independent state. He continued his education at the same university, and obtained a "Candidate" (Equivalent of M.Sc.) degree in "Radiotechnics" (Electrical Engineering) and was employed for some time as a research scientist at the Research Laboratory run by Prof. Boris Kashcheyev. Aleks was working as a part of a team developing the first Ukrainian wind profiling Radar, and conducting measurements of various atmospheric parameters with other experimental radars. His interest in atmospheric research developed into a career at the School of Earth and Atmospheric Sciences of the Georgia Institute of Technology where he came in 2000 to pursue first a Master of Science and then a Doctoral degree under the guidance of Dr. R. G. Roper.